SAPIENZA
UNIVERSITÀ DI ROMA

Tackling Conceptual Problems in Gravity with Numerically Simulated *Gedanken Experiments*

Scuola dottorale in scienze astronomiche, chimiche, fisiche, matematiche e della terra "Vito Volterra"

PhD in Physics (XXXVI cycle)

Fabrizio Corelli

ID number 1706626

Advisor

Prof. Paolo Pani

Academic Year 2022/2023

Tackling Conceptual Problems in Gravity with Numerically Simulated *Gedanken Experiments*

PhD thesis. Sapienza University of Rome

This thesis has been typeset by LaTeX and the Sapthesis class.

Author's email: fabrizio.corelli@uniroma1.it

Contents

Chapter 1

Introduction

Gedanken experiments, *i.e.* thought experiments [1], are an extremely powerful tool for the development and illustration of scientific theories and philosophical arguments. In physics they have been used already by Galileo and Newton, for instance with the ship experiment [2], the Leaning Tower of Pisa experiment [3], or the bucket argument [4], while notable and extremely popular examples from the 20th century include the twin paradox [5, 6], the Schrödinger's cat [7], the Bell's spaceship paradox [8, 9], and the Dyson sphere [10].

In general, the idea is to imagine a hypothetical experiment in which some conceptual aspects or some principles of a theory clearly manifest and can be better appreciated. The understanding acquired in this way can then be used for different purposes: to clarify the first principles on which a theory is based (like in the Galileo's ship experiment), to investigate and illustrate the implications of a theory (like in the twin paradox), or eventually to highlight critical aspects that are worth considering (like in the Einstein-Podolsky-Rosen paradox [11] or in the Schrödinger's cat).

One of the main advantages of this approach is that the setups conceived are not required to be realizable, but only to satisfy all the physical properties that are relevant for the argument. This means not only that in devising the experiment one does not need to take into account measurement uncertainties and optimize the setup to reduce them, but also that one is allowed to consider completely impracticable scenarios in which the impact of the effects under examination is particularly evident.

However, successfully constructing a gedanken experiment requires a deep understanding of the theory and the phenomena one is interested in testing, as the outcome is dictated only by the reasoning of the "experimenter" and not by reality. In particular it is necessary to correctly interpret the foundational aspects of a theory and their consequences, and in some cases also to predict the evolution of physical systems. To be more concrete on this latter point, let us consider the Newton's cannonball [12], a gedanken experiment in which a stone is projected from a mountain, pointing in a direction parallel to the surface of the Earth. Due to gravitational attraction, the stone will descend following a curved trajectory, until it touches the ground. If this process is repeated progressively increasing the initial velocity, the stone will cover larger and larger distances, up to the point in which

it can return to the original point, entering in a circular periodic motion. Further increasing the velocity, then, the stone will follow more complex and eccentric trajectories, that corresponds to the orbits of Planets. As we can see in this experiment the prediction of the trajectory of the stone plays a central role, and it is crucial that it is based on a well-oriented physical sense.

In theories governed by nonlinear sets of equations the task of visualizing the behavior of a physical system can become exceptionally challenging or even impossible, as the different components of the system interact in complex ways, and it might be hard to identify the dominant terms and assess how they affect the evolution. It is the case of general relativity (GR) for instance, given the nonlinear character of Einstein's equations. Such difficulties show therefore that the fact that gedanken experiments are only based on human reasoning constitutes also an intrinsic limitation: overly complicated situations cannot be handled.

Nevertheless in some circumstances the possibility of considering setups that are completely unattainable from the observational point of view is extremely attractive, and one might not wish to abandon the gedanken experiment technique even if the theory is nonlinear. Restricting to gravity for convenience, let me present three possible use cases.

Firstly, in GR there are deeply conceptual problems that have not been fully addressed, but can be tackled quite effectively by means of gedanken experiments. As an example, at the end of the '80s it was found that some wormhole solutions may contain closed timelike curves [13], a situation that raises the question of whether time travel is possible in GR, and leads to well-defined Cauchy problems and self-consistent evolutions. These aspects where investigated in Refs. [14,15] by analyzing a fictitious setup in which a billiard ball enters in one of the wormhole mouths, exits from the other (having travelled backwards in time), and then hits itself before entering in the first mouth.

Secondly, while the compact objects that have been observed via gravitational [16–19] and electromagnetic [20–24] facilities are well described by the Kerr metric, it is still possible that their nature is different. Various models for exotic compact objects have been proposed in literature, such as wormholes [25–28], gravastars [29, 30], scalar [31–33] or vector [34] boson stars [35], and others [36]. Gedanken experiments on such objects provide a way to test them from the theoretical point of view, and can reveal important information about their structure, highlighting some specific phenomena that can act as smoking guns for their presence, or, conversely, highlight inconsistencies that can be used to rule out some models.

Lastly, despite the elegance and the experimental successes of GR, there are strong indications that it is not the ultimate theory of gravity. For instance, GR cannot be included in a quantum field theory description of the Universe, since it is not renormalizable [37], and at the same time cosmology is plagued by the cosmological constant problem [38], *i.e.* the incompatibility between the measured value of the cosmological constant and the zero-point energy. As a result, it is necessary to introduce modifications to GR, and several alternative theories of gravity have been proposed (see Refs. [39–41] for reviews). Pretty much as in the previous case, gedanken experiments can be used to test such theories, helping in identifying their distinctive features and potential criticalities from the purely conceptual point of view.

Clearly, it is not completely impossible to successfully carry out gedanken experiments in gravity, as also testified by the billiard ball experiment discussed above, but in some cases the complexity of the theory makes controlling the setup excessively hard and error prone. This is particularly true for modified gravity, since the field equations are often more complex than in GR, and additional fundamental fields may be included.

A strategy to circumvent such difficulties is to demand the task of evolving the system under investigation to a numerical integration algorithm. The approach changes significantly, as the gedanken experiment becomes *numerically simulated*, and should be more intended as a conceptual, rather than a thought, experiment. The research procedure takes the following form. Firstly, one has to devise the setup to study, modeling in detail all the components of the system and deriving the equations that govern its evolution. With these informations one can prepare the evolution code, and construct the initial configuration. Then the simulation can be run, and the integration algorithm takes full control over the evolution: the role of the "experimenter" is now reduced to observe the final result and analyze the output data.

Clearly, setting up a numerical integration code is far from being effortless, as it often involves optimizations and debugging operations to ensure that the code is reliable. However, such difficulties are counterbalanced by the fact that the automated resolution of the equations opens research paths that would have hardly been viable with standard gedanken experiments, allowing to explore regimes in which the phenomenology is unknown. In other words, not only one can target specific conceptual aspects, but also consider setups for which there are few expectations on the evolution, with the purpose of acquiring knowledge on the phenomenological behavior of a theory.

Another possible drawback of numerical simulations is that they can be extremely demanding from the computational of view, and in some cases a supercomputer is needed. It is however worth emphasizing that since gedanken experiments are not required to be realistic, one can work in simplified or highly symmetric setups, in such a way to reduce the number of variables and equations, decreasing considerably the computational cost.

In light of these considerations, I will dedicate the next three chapters to present three numerically simulated gedanken experiments that I carried out with different collaborators and resulted in the manuscripts in Refs. [42–45]. Each gedanken experiment is aimed at tackling a problem of different nature, and while they have individual physical motivations and points of interest, it is when they are considered collectively that they show the points of strength of this research technique.

I will start in Chapter 2 describing the work in Ref. [42], carried out in collaboration with prof. Paolo Pani and Dr. Taishi Ikeda, which constitutes an example of how numerical simulations can be used to test a conjecture, and at the same time of how they can lead to the discovery of new phenomena.

In particular, our focus was on the weak cosmic censorship conjecture (WCCC) [46], according to which if matter satisfies the dominant energy condition, then the maximal Cauchy evolution of initial data satisfying appropriate falloff conditions at

spatial infinity is asymptotically flat and strongly asymptotically predictable (see Refs. [47, 48] for overviews).

Predictability is of utmost importance for a physical theory. In GR this property can be spoiled due to the presence of singularities, locations where the theory breaks down which can act as sources of non-physical information [49, 50]. Since they generally arise as the result of gravitational collapse [51, 52], their role is particularly relevant for black holes (BHs). However, as long as a singularity remains confined inside an horizon, information coming from it cannot propagate in the entire spacetime, preserving predictability outside the BH. In light of these considerations, WCCC is often informally formulated as requiring that singularities forming from gravitational collapse should be hidden by an horizon [47].

For the Kerr-Newman configuration, not every choice of the charge Q and dimensionless spin a is compatible with the WCCC. Indeed, only when $Q^2+a^2 \leq M^2$, where M is the BH mass and $G = c = 4\pi\varepsilon_0 = 1$, there are horizons to censor the singularity, while in the opposite case the WCCC would be violated. In literature several gedanken experiments have been performed in order to try to overcharge or overspin a BH past the extremal condition $Q^2 + a^2 = M^2$ by means of particles [53–59], fluids [60], shells of matter [54], test fields [59, 61–63], and even in binary mergers [64, 65]. While some successful results have been obtained, there are some critical aspects and they cannot be regarded as proof of the possibility of violating the WCCC. For example, most of these studies were performed at the linear level, and it was pointed out that backreaction and finite size effects restore WCCC [66–74]. As we can see this is a paradigmatic case of how a nonlinear treatment of the gedanken experiment is necessary, which is what we did in Ref. [42]. In particular we focused on the spherically symmetric charged case, in which the Kerr-Newman configuration reduces to the Reissner-Nordström (RN) one, and the WCCC imposes $Q^2 \leq M^2$. We simulated the spherical collapse of wave packets of an electrically charged scalar field, both in flat spacetime, trying to form RN BH with $Q^2 > M^2$ from the beginning, and on a RN background, trying to overcharging a pre-existing BH past extremality. These numerically simulated gedanken experiments where already performed by Torres and Alcubierre [75], but in our work we were able to reach BH charges considerably closer to the RN bound $Q^2 = M^2$. While we were not able to violate the WCCC, studying the behaviors of such systems at the fully nonlinear level gave us the possibility of identifying two cosmic censors: electrostatic repulsion, and superradiance [72], a mechanism that allows to extract energy and charge from a BH.

In the same work we also extended our simulations to Einstein-Maxwell-scalar (EMS) gravity [76], a modification to the matter sector of Einstein-Maxwell in which a real scalar field is nonminimally coupled to the electromagnetic field. This theory admits additional hairy BH configurations featuring a nontrivial profile of the scalar field outside them, called *scalarized configurations*, that appear only for large values of the charge-to-mass-ratio and can coexist with RN BHs. For certain choices of the coupling function, highly charged RN BHs can develop a tachyonic instability and transit towards a scalarized configuration, in a *spontaneous scalarization* phenomenon similar to the one occurring in Einstein-scalar-Gauss-Bonnet gravity [77–79].

Interestingly, scalarized BHs are not subject to the RN bound, but still WCCC

imposes an upper limit to their charge which is larger than M. We simulated[1] the collapse of charged wave packets on scalarized configurations, and while we were able to produce scalarized BHs with $Q^2 > M^2$, we found no signals of WCCC violations, as in the Einstein-Maxwell case.

As a byproduct, we were able to simulate a *descalarization* process, *i.e.* the transition from a scalarized to a RN configuration. Indeed, since scalarized solutions exist only above a certain threshold of the charge-to-mass ratio, a scalarized BH undergoing a dynamical process in which its charge-to-mass ratio decreases below such threshold will be forced to loose its scalar hair, and become of RN type (see Refs. [85–87] for the analogous phenomenon in Einstein-scalar-Gauss-Bonnet gravity). Our simulations show that this process can occur thanks to the absorption of an opposite-charged wave packet, and to the superradiant scattering of a wave packet with charge of the same sign, in a novel *superradiantly induced descalarization* mechanism that we identified for the first time.

Overall, the simulations that we performed in Ref. [42] support the WCCC in a remarkably clear way, but encode complex physical phenomena that are hard to treat with semi-analytical methods, showing the effectiveness of numerically simulated gedanken experiments in tackling conceptual problems of this type.

In Chapter 3 I will show a case in which numerical simulations can be used to tackle an intrinsic conceptual problem in a theory of modified gravity, describing the work in Refs. [43,44], that I carried out in collaboration with Marina de Amicis, Dr. Taishi Ikeda, and Prof. Paolo Pani.

In this work we studied Einstein-dilaton-Gauss-Bonnet (EdGB) gravity [88], a theory that modifies GR in the high energy/curvature regime by introducing an additional real scalar field, called *dilaton*, nonminimally coupled to quadratic curvature terms via an exponential function. Such coupling terms appear in the context of low-energy expansions of string theory (see *e.g.* [89]), but here I am going to take another perspective. Indeed by dimensional arguments it is possible to see that, due to the presence of quadratic curvature terms, this theory is characterized by a new fundamental length scale $\tilde{\ell}$ that defines the regime where modifications appear: for length scales $\ell \gg \tilde{\ell}$ the theory reduces to GR, while for scales $\ell \lesssim \tilde{\ell}$ modifications become dominant. Now, if one wishes EdGB to provide quantum gravity corrections to GR, the most natural choice would be to set $\tilde{\ell}$ to the size of the Planck length. However, currently GR has been tested only on much larger length scales [39, 90], and it is still possible that modifications appear well before a quantum description of gravity is needed. With these motivations in mind, we treated EdGB as a purely classical theory, assuming $\tilde{\ell}$ to be sufficiently far from the Planckian regime.

Differences between GR and EdGB clearly manifest when studying BHs. In particular, EdGB BH solutions feature a nontrivial profile of the dilaton outside them [88], and possess a curvature singularity at finite radius inside the horizon [91]. Furthermore, they possess a minimum value for the mass of $\mathcal{O}(\tilde{\ell})$ [91–93], unlike GR BHs, for which the mass is unconstrained. The existence of the minimum-mass

[1] See also Refs. [76, 80–83] for numerical simulations in Einstein-Maxwell-scalar or Einstein-Maxwell-dilaton [84] theories

BH solution, called *critical* configuration, raises important interrogatives from the thermodynamic point of view, and calls for further investigation. Indeed, BHs are subject to an evaporation mechanism in which they lose mass by means of a thermal radiation, called Hawking radiation [94]. Now, for EdGB BHs it has been shown that the evaporation process is not halted at the minimum-mass configuration [91,92,95], and while in general an evaporating BH can reach a configuration with lower mass, critical BHs do not have such possibility, and is not clear how they will evolve and what is their fate [92, 96].

In our work we tried to answer this question by means of numerical simulations. Our idea was to include in the matter term of the action a phantom field, *i.e.* a real scalar field with "wrong" sign of the kinetic term, which contributes with a negative term in the total mass of the system. Therefore by collapsing a wave packet of this field onto a critical BH we were able to dynamically reduce the BH mass, emulating at the classical level the effect of Hawking's evaporation. Note, however, that it was not an emulation of the (quantum) radiation process, but we were only inducing its effects in order to study where the intrinsic dynamics of the theory (its classical field equations) drives the BH to when its mass is pushed below the minimum value.

Let me highlight that, in the spirit of gedanken experiments, the setup we considered is manifestly unrealistic, but allowed to directly tackle the conceptual problem at hand, explicitly pushing the system in the regime we were interested in. Furthermore, given the fact that we studied a scenario in which nonlinear effects are extremely relevant, and that the dynamics is governed by the equations of a modified theory of gravity, an analytical or semi-analytical treatment of the evolution would have been highly impractical. We can therefore see that this is a case in which the use of numerical simulations is particularly beneficial, as it allows to shift the effort to the preparation of the numerical integration code, and then evolve the system in an automated way, relying on the accuracy of the algorithm.

In Chapter 4 I will describe a work that I did in collaboration with Enrico Cannizzaro and Prof. Paolo Pani [45], in which we used numerically simulated gedanken experiments to characterize the dynamics of a system in a regime which is not easily accessible with semi-analytical methods. While the motivations for this study are discussed in the chapter, here I would like to highlight few aspects that are useful to delineate the type of gedanken experiment we performed.

Low-frequency radiation can extract energy from rotating BHs thanks to a process called *superradiant scattering* [97–99] (see [72] for a review). Intriguingly, if radiation is confined in the vicinity of the BH, energy extraction can happen repeatedly and produce instabilities that can lead to explosive phenomena, thus converting the system into what is known as "BH bomb" [100]. Massive fields are naturally prone to this instability, as for them the confining mechanism is provided by their own mass [101, 102].

In the case of photons, which are massless, the instability can be promoted by the presence of plasma surrounding the BH. Indeed plasma is characterized by a typical frequency, called *plasma frequency* [103–105], that plays the role of an effective mass for photons, providing them with a confining mechanism. Such form of superradiant instability has been studied quantitatively for example for primordial BHs in the early Universe [106], or for astrophysical BHs due to plasma

present in intracluster environments [107]. While in these two studies the photon was approximated as a massive vector field with mass given by the plasma frequency, more recent computations were carried out using Maxwell's equations [108,109], but still neglecting the backreaction of the electromagnetic field on plasma.

While such linear analyses give important information regarding the onset of the instability, during the evolution the growth of the intensity of the fields drives the system in a regime where it is necessary to take into account nonlinear effects. In this respect, in Ref. [110] it was pointed out that for strong electromagnetic fields plasma can become transparent to radiation [111], losing the ability to confine it and quenching the superradiant instability. Nevertheless, the transparency phenomenon of [111] applies to idealized scenarios of circularly polarized electromagnetic waves propagating through a homogeneous plasma, and it is not yet clear if it also manifests in the more involved scenario of superradiant instability.

In our work [45] we studied the propagation of the electromagnetic field inside plasma in the regime relevant for superradiance, in a more generic setting. We considered a gedanken experiment in which an electromagnetic wave packet of high amplitude and low frequency is scattered off a barrier of plasma. Being the evolution dominated by the electromagnetic interaction in this regime, we neglected the gravitational field, and we performed the analysis in flat spacetime. Thanks to numerical simulations we could integrate the full Maxwell's equations at the nonlinear level, and while we did not observe the transparency phenomenon, we were able to access a regime where the backreaction effects on the plasma density are strong, and can still quench the superradiant instability.

The conclusions of these works will be summarized in Chapter. 5.

As a convention, throughout the thesis Greek indices will run over spacetime dimensions ($\mu, \nu \in \{0, 1, 2, 3\}$), while Latin indices will run over spatial dimensions ($i, j \in \{1, 2, 3\}$). Given that the three gedanken experiments have been performed in three different physical contexts, a different set of units will be set on each chapter.

Publication list

The manuscripts on which this work is based (Refs. [42–45]) are the following:

- F. Corelli, T. Ikeda, and P. Pani, "Challenging cosmic censorship in Einstein-Maxwell-scalar theory with numerically simulated gedanken experiments", *Phys. Rev. D* **104** (2021), 084069, arXiv: 2108.08328 [gr-qc].

- F. Corelli, M. de Amicis, T. Ikeda, and P. Pani, "What Is the Fate of Hawking Evaporation in Gravity Theories with Higher Curvature Terms?", *Phys. Rev. Lett.* **130** (2023), 091501, arXiv: 2205.13006 [gr-qc].

- F. Corelli, M. de Amicis, T. Ikeda, and P. Pani, "Nonperturbative gedanken experiments in Einstein-dilaton-Gauss-Bonnet gravity: Nonlinear transitions and tests of the cosmic censorship beyond general relativity", *Phys. Rev. D* **107** (2023), 044061, arXiv: 2205.13007 [gr-qc].

- E. Cannizzaro, F. Corelli, and P. Pani, "Nonlinear photon-plasma interaction and the black hole superradiant instability", *Phys. Rev. D* **109** (2024), 023007, arXiv: 2306.12490 [gr-qc].

Numerical integration codes

The codes for numerical integration used in all the three works have been written in C++ and use OpenMP for parallelization. They are completely original and independent from any pre-existing code or software platform for numerical relativity.

Chapter 2

Tests of the weak cosmic censorship conjecture in Einstein-Maxwell and in Einstein-Maxwell-scalar theories of gravity

In this chapter I describe the numerical simulations I performed in Ref. [42], in collaboration with Dr. Taishi Ikeda and Prof. Paolo Pani, to test the WCCC in Einstein-Maxwell and in Einstein-Maxwell-scalar theories of gravity.

However, before entering into the details of our numerical investigations I would like to dedicate the next two sections to briefly introduce the conceptual framework in which we will operate. In particular I will start in Sec. 2.1 with an outline of singularities and WCCC, focusing on RN spacetimes, which are of interest for our work. Next, in Sec. 2.2, I will introduce EMS gravity, discussing scalarized BH solutions and the spontaneous scalarization phenomenon.

Then I will move to our work, starting with Sec. 2.3 in which I will describe the setup for our numerically simulated gedanken experiments. Here I will introduce the model we used, the evolution equations, and the integration algorithm for numerical evolution. Finally, in Sec. 2.4 I will discuss the different sets of simulations that we performed and the results we obtained.

Throughout the chapter I will use geometric units with $G = c = 4\pi\varepsilon_0 = 1$.

2.1 Singularities, Reissner-Nordström metric and the cosmic censorship

Spacetime singularities are locations where GR fails in describing a physical configuration and there is a breakdown of the theory. A typical example is the center of a Schwarzschild BH, but it is not an isolated case. Indeed, Penrose-Hawking singularity theorems [51, 52] predict that singularities will inevitably form as a result of the gravitational collapse, if matter satisfies some reasonable energy conditions. Due

to their nature, singularities can act as sources of non-physical information that can propagate inside the spacetime, jeopardizing the predictability of GR [49, 50]. For BHs this problem does not appear, since the information coming from the singularity cannot cross the horizon, and predictability is not spoiled in the external region. However GR also admits solutions, called *naked singularities* in which the singularity is not covered by an horizon, and in principle information coming from it can reach also distant observers. To give an example that will be central in the rest of the chapter, let us analyze the Reissner-Nordström (RN) metric, which describes spherically-symmetric and electrically charged spacetime configurations, and is given by the following line element [47]:

$$ds^2 = -\left(1 - \frac{2M}{r} + \frac{Q^2}{r^2}\right)dt^2 + \frac{1}{1 - \frac{2M}{r} + \frac{Q^2}{r^2}}dr^2 + r^2(d\theta^2 + \sin^2\theta d\varphi^2), \qquad (2.1)$$

where M is the mass, and Q is its electric charge.

To identify the singularity a more formal definition is needed. However, defining a singularity in a comprehensive way is not straightforward (see Refs. [47, 112] for a discussion), but since in this thesis we will be interested mainly in phenomenological aspects, for our purposes we will consider a singularity as a coordinate location where one or more curvature invariants diverge, also referring to it as a curvature singularity.

Now, from Eq. (2.1) we see that the metric is ill-defined both at $r = 0$, and where $1 - \frac{2M}{r} + \frac{Q^2}{r^2} = 0$. If we compute the Kretschmann scalar we obtain

$$K = R_{\mu\nu\rho\sigma}R^{\mu\nu\rho\sigma} = \frac{8}{r^8}\left(7Q^4 - 12MQ^2r + 6M^2r^2\right). \qquad (2.2)$$

Since K diverges on $r = 0$ we can identify the center as a curvature singularity. The other two locations are horizons, and are located at

$$r_\pm = M \pm \sqrt{M^2 - Q^2}. \qquad (2.3)$$

We can see that if $Q^2 < M^2$ the two horizons are well-defined and distinct, if $Q^2 = M^2$ they coincide. Instead if $Q^2 > M^2$, the equation $1 - \frac{2M}{r} + \frac{Q^2}{r^2} = 0$ does not admit solutions for r, and hence there are no horizons, meaning that the metric (2.1) represents a naked singularity. Penrose's weak cosmic censorship conjecture [46] protects the theory against such configurations, requiring that singularities forming from gravitational collapse are always hidden by an horizon. For RN spacetimes this results in the requirement $Q^2 \leq M^2$, and the case $Q^2 > M^2$ is explicitly forbidden. In other words the charge-to-mass ratio $\bar{Q} = Q/M$ is bound to be in the interval $-1 \leq \bar{Q} \leq 1$, a condition that can be expressed with the statement that *RN spacetimes cannot be overcharged*.

However, WCCC still lacks a definitive proof, and in this chapter we will challenge it by trying to dynamically form RN configurations with $\bar{Q} > 1$.

2.2 Einstein-Maxwell-scalar gravity and scalarized BHs

As a second step to set the stage for the gedanken experiments discussed in this chapter, let me introduce Einstein-Maxwell-scalar gravity [76]. It is a theory that

modifies Einstein-Maxwell in the matter sector by adding a real scalar field nonminimally coupled to the electromagnetic field. The action is given by:

$$S = \frac{1}{16\pi}\int_\Omega d^4x\,\sqrt{-g}\Big\{R - 2(\nabla_\mu\phi)(\nabla^\mu\phi) - F[\phi]\,F_{\mu\nu}F^{\mu\nu}\Big\}, \tag{2.4}$$

where ϕ is the scalar fields, A_μ is the vector field, $F[\phi]$ is the coupling function, $F_{\mu\nu} = \nabla_\mu A_\nu - \nabla_\nu A_\mu$ is the electromagnetic tensor, $g_{\mu\nu}$ is the spacetime metric, and R is the Ricci scalar.

The field equations of EMS are:

$$G_{\mu\nu} = 8\pi\Big(T^{\rm SF}_{\mu\nu} + T^{\rm EM}_{\mu\nu}\Big), \tag{2.5}$$

$$\nabla_\mu F^{\mu\nu} = -F^{\mu\nu}\frac{1}{F[\phi]}\frac{\delta F[\phi]}{\delta\phi}\nabla_\mu\phi, \tag{2.6}$$

$$\Box\phi = \nabla_\mu\nabla^\mu\phi = \frac{1}{4}\frac{\delta F[\phi]}{\delta\phi}F_{\mu\nu}F^{\mu\nu}, \tag{2.7}$$

where $G_{\mu\nu} = R_{\mu\nu} - \frac{1}{2}Rg_{\mu\nu}$ is the Einstein's tensor and

$$T^{\rm SF}_{\mu\nu} = \frac{1}{4\pi}(\nabla_\mu\phi)(\nabla_\nu\phi) - \frac{1}{8\pi}(\nabla_\alpha\phi)(\nabla^\alpha\phi)g_{\mu\nu}, \tag{2.8}$$

$$T^{\rm EM}_{\mu\nu} = \left\{\frac{1}{4\pi}F_{\mu\alpha}g^{\alpha\beta}F_{\nu\beta} - \frac{1}{16\pi}F_{\alpha\beta}F^{\alpha\beta}g_{\mu\nu}\right\}F[\phi]. \tag{2.9}$$

In this class of theories, due to the presence of the nonminimal coupling, BH solutions can feature a nontrivial profile of the scalar field. In the particular case $F[\phi] = 1$ the theory reduces to the well-studied Einstein-Maxwell gravity minimally coupled with a real scalar field, and BHs are generically described by the Kerr-Newman metric (or Reissner-Nordström in spherical symmetry). In the other cases the properties of BH solutions depend on the choice of the coupling, and in order to delineate them it is useful to consider the classification presented in Ref. [113], which proceeds as follows. First, theories are divided in two classes on the basis of whether they admit the Kerr-Newman solution, which is characterized by a vanishing profile of the scalar field, $\phi = 0$. In particular, class I includes theories such that $\phi = 0$ is not a solution, while class II includes theories such that $\phi = 0$ is a solution of the field equations. In order for the Kerr-Newman configuration to be a solution the condition

$$F'[0] = \frac{\delta F[\phi]}{\delta\phi}\Big|_{\phi=0} = 0, \tag{2.10}$$

has to be valid, in such a way that Eq. (2.7) is satisfied. Therefore for theories of class I $F'[0] \neq 0$, while for theories of class II $F'[0] = 0$.

As an example, Einstein-Maxwell-dilaton (EMd) [84] has $F[\phi] = e^{2\alpha\phi}$, where α is a coupling constant, and belongs to class I. We can see that $F'[0] \neq 0$ and it only admits hairy BH solutions with a nontrivial profile of ϕ outside them.

Theories of class II instead generically admit both Kerr-Newman BHs, and hairy BHs with the nontrivial profile of ϕ, which in this context are called *scalarized BH solutions*. The two sets of solutions can be continuously connected or not, giving rise to a subclassification: theories in which the scalarized solutions continuously

connect to the set of solutions with $\phi = 0$ are of class IIA, while theories in which the scalarized solutions are disconnected from the Kerr-Newman solutions are of class IIB.

Interestingly, in both theories of class IIA and IIB Kerr-Newman BHs can dynamically transit towards scalarized configurations, in a process called *scalarization*. However, the characteristics of this process can present differences across the two classes which can be illustrated in the following way [113]. Let us consider a perturbation of the scalar field around the Kerr-Newman configuration, $\phi = 0 + \delta\phi$. Since $F'[0] = 0$, Eq. (2.7) reduces to

$$\Box\delta\phi - \frac{1}{4}F_{\mu\nu}F^{\mu\nu}\frac{\delta^2 F}{\delta\phi^2}\bigg|_{\phi=0}\delta\phi = 0, \tag{2.11}$$

which can be rewritten as a Klein-Gordon equation for the perturbation, $(\Box - \mu_{eff}^2)\delta\phi = 0$, where $\mu_{eff}^2 = \frac{1}{4}F_{\mu\nu}F^{\mu\nu}\frac{\delta^2 F}{\delta\phi^2}\Big|_{\phi=0}$ plays the role of an effective mass squared. For theories of the class IIA, if $\frac{\delta^2 F}{\delta\phi^2}\Big|_{\phi=0} \neq 0$ and has a sign such that $\mu_{eff}^2 < 0$, the Kerr-Newman BH can be subject to a tachyonic instability whose end state can be a scalarized BH. This is the so called *spontaneous scalarization*, and happens for example in theories with couplings of the form $F[\phi] = 1 - \alpha\phi^2$ [114] or $F[\phi] = e^{-\alpha\phi^2}$ [76]. It is worth mentioning, however, that in curved spacetime the negativity of μ_{eff}^2 does not automatically imply the appearance of the instability. In particular, the presence of the instability has to be inspected directly from the perturbation equation. This is usually done by studying the effective potential obtained after an appropriate decomposition [79].

If $\frac{\delta^2 F}{\delta\phi^2}\Big|_{\phi=0} = 0$ instead, then there is no tachyonic instability, and the scalarization can be induced by large perturbations of the scalar field. It is the case of couplings of the form $F[\phi] = 1+\alpha\phi^4$ [115], or $F[\phi] = e^{\alpha\phi^4}$ [83], which are of class IIB.

Having given an overview of the generic properties of BH solutions in EMS gravity, let us now specialize to the case of interest for our work: a theory of class IIA featuring a spontaneous scalarization mechanism. In particular we focused on a quadratic coupling function $F[\phi] = 1 - \lambda\phi^2$, where λ is a dimensionless coupling constant; we can immediately see that $F'[0] = 0$, and $F''[0] = -2\lambda$. Furthermore we restricted to spherical symmetry, since it remarkably simplifies the computations and the discussions while preserving the elements we were interested in. In this case the magnetic field vanishes and $F_{\mu\nu}F^{\mu\nu} < 0$, therefore the tachyonic instability can appear only if $\lambda < 0$.

The domain of existence of scalarized solutions for quadratic coupling has been obtained by Fernandes *et al.* in Ref. [114]. We reproduced their results for configurations with zero nodes of the scalar field with equivalent computations, obtaining the plot in Fig. 2.1, where we show a parameter space with the coupling constant on the horizontal axis and the charge-to-mass ratio on the vertical axis. As we will see in Sec. 2.3.3, there are two meaningful definitions of electric charge, here we used $\tilde{Q}$, which is constant outside the BH. However, this choice has no impact on the discussion of this section.

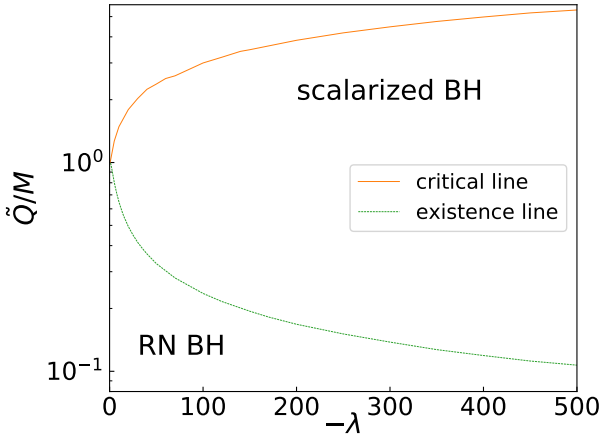

Figure 2.1. Domain of the existence of nodeless scalarized solutions in Einstein-Maxwell-scalar theory with $F[\phi] = 1 - \lambda\phi^2$. See also Ref. [114] for an equivalent domain plot.

Interestingly, the parameter space does not include quantities that describe the content of the scalar field. In fact in principle scalarized BHs are characterized by the so called *scalar charge*, defined as [84]:

$$D = -\frac{1}{4\pi}\int_{\mathcal{S}^2_{\rm inf}} d\Sigma^\mu \nabla_\mu \phi, \tag{2.12}$$

where $\mathcal{S}^2_{\rm inf}$ is a 2-Sphere at spatial infinity. However this charge is not a free parameter, but is determined from the BH mass and electric charge, and might not be required to identify a BH configuration [116].

The domain of existence of scalarized solutions is bounded by two lines. The first, called existence line, and shown in green in the plot, is the region where the scalarized solutions bifurcate from the RN ones. The other instead, called critical line, and shown in red, contains singular configurations. We see that, given a fixed value of the coupling constant λ, scalarized BHs exist in a limited interval of the charge-to-mass ratio that extends from the existence line to the critical line, but can include values above the RN bound, meaning that scalarized BH can be overcharged. It is worth mentioning that the way the singularity appears at the upper bound of the charge-to-mass ratio is different from the RN case. Indeed for scalarized BHs the horizon area vanishes at the critical line [114], while for a RN BH it reaches the value of $4\pi M^2$ and then the singularity is exposed due the fact that there are no solutions to $1 - \frac{2M}{r} + \frac{Q^2}{r^2} = 0$. However it is interesting also in this case to investigate the possibility of violating the WCCC by overcharging scalarized BHs past the critical line.

2.3 Setup for the numerically simulated gedanken experiments

We have seen that for RN spacetimes the absence of naked singularities translates into the requirement that $\bar{Q} = Q/M \leq 1$. In our work [42] we tried to challenge this

condition, and hence WCCC, with two different sets of gedanken experiments. In the first we simulated the spherical collapse of ingoing wave packets of an electrically charged scalar field on flat spacetime, with the purpose of forming a configuration which is overcharged from the beginning. In the second set instead we tried to overcharge a pre-existing RN BH using spherically-symmetric charged scalar wave packets. Then we also repeated similar sets of simulations for scalarized BHs in EMS gravity, for which the maximum value of the charge-to-mass ratio can be larger than one.

Having in mind all these different groups of numerically simulated gedanken experiments, in this section I will present a unified setup to perform them, describing the evolution equations, and the numerical integration algorithm. Since the initialization procedure can vary considerably across the sets of simulations, I will describe them in the next section together with the results, keeping only the common aspects here.

2.3.1 Action of the theory and field equations

We considered the Einstein-Maxwell-scalar model studied in Ref. [76], minimally coupled to an additional (complex) charged scalar field:

$$S = \frac{1}{16\pi}\int_\Omega d^4x\,\sqrt{-g}\left\{R - 2(\nabla_\mu\phi)(\nabla^\mu\phi) - F[\phi]\,F_{\mu\nu}F^{\mu\nu} - 4(\mathcal{D}_\mu\xi)(\mathcal{D}^\mu\xi)^*\right\}, \quad (2.13)$$

where ϕ and ξ are the real and the complex scalar fields respectively, A_μ is the vector field, $F[\phi]$ is the coupling function, $F_{\mu\nu} = \nabla_\mu A_\nu - \nabla_\nu A_\mu$ is the electromagnetic tensor, $\mathcal{D}_\mu = \nabla_\mu + iqA_\mu$ is the gauge covariant derivative for $U(1)$ symmetry, q is the electric charge of the complex scalar field, and $*$ denotes the complex conjugate operation. $g_{\mu\nu}$ is the spacetime metric, and R is the Ricci scalar.

The field equations that can be derived from (2.13) are

$$G_{\mu\nu} = 8\pi\Big(T^{\rm SF}_{\mu\nu} + T^{\rm EM}_{\mu\nu} + T^{\xi}_{\mu\nu}\Big), \quad (2.14)$$

$$\nabla_\mu F^{\mu\nu} = -F^{\mu\nu}\frac{1}{F[\phi]}\frac{\delta F[\phi]}{\delta\phi}\nabla_\mu\phi + \frac{iq}{F[\phi]}\Big[\xi(\mathcal{D}^\nu\xi)^* - \xi^*(\mathcal{D}^\nu\xi)\Big], \quad (2.15)$$

$$\Box\phi = \nabla_\mu\nabla^\mu\phi = \frac{1}{4}\frac{\delta F[\phi]}{\delta\phi}F_{\mu\nu}F^{\mu\nu}, \quad (2.16)$$

$$\Box\xi = -iq(\nabla_\mu A^\mu)\xi - 2iqA^\mu\nabla_\mu\xi + q^2A_\mu A^\mu\xi, \quad (2.17)$$

where $G_{\mu\nu} = R_{\mu\nu} - \frac{1}{2}Rg_{\mu\nu}$ is the Einstein's tensor and

$$T^{\rm SF}_{\mu\nu} = \frac{1}{4\pi}(\nabla_\mu\phi)(\nabla_\nu\phi) - \frac{1}{8\pi}(\nabla_\alpha\phi)(\nabla^\alpha\phi)g_{\mu\nu}, \quad (2.18)$$

$$T^{\rm EM}_{\mu\nu} = \left\{\frac{1}{4\pi}F_{\mu\alpha}g^{\alpha\beta}F_{\nu\beta} - \frac{1}{16\pi}F_{\alpha\beta}F^{\alpha\beta}g_{\mu\nu}\right\}F[\phi], \quad (2.19)$$

$$T^{\xi}_{\mu\nu} = \frac{1}{4\pi}\Big[(\mathcal{D}_\mu\xi)(\mathcal{D}_\nu\xi)^* + (\mathcal{D}_\mu\xi)^*(\mathcal{D}_\nu\xi) - (\mathcal{D}_\alpha\xi)(\mathcal{D}^\alpha\xi)^*g_{\mu\nu}\Big]. \quad (2.20)$$

As previously mentioned, we used $F[\phi] = 1 - \lambda\phi^2$ with $\lambda < 0$, in order to allow for scalarized solutions. Since $F[0] = 1$ and $F'[0] = 0$, we see that for vanishing

configurations of ϕ Eq. (2.16) is identically satisfied and the theory reduces to Einstein-Maxwell minimally coupled to a complex scalar field. Therefore this model can be used for simulations not only in Einstein-Maxwell-scalar, but also in Einstein-Maxwell if ϕ is set to zero. However, for the sake of generality for the moment I will not assume any specific form of $F[\phi]$, but I will only require $F[0] = 1$.

It is worth mentioning that, when considering a spherically symmetric spacetime, the choice of a positive coupling function is a sufficient condition for the null energy condition to be satisfied. I report the proof of this statement in Appendix A.

2.3.2 Evolution scheme

For the time integration of the equations of motion we used a generalization of the original Baumgarte-Shapiro-Shibata-Nakamura (BSSN) formalism [117, 118] in spherical symmetry [119, 120]. The line element is given by

$$ds^2 = (-\alpha^2 + \beta_r\beta^r)\,dt^2 + 2\beta_r\,dt\,dr + e^{4\chi(r,t)}\Big(a(r,t)\,dr^2 + b(r,t)\,r^2\,d\Omega^2\Big), \quad (2.21)$$

where α is the lapse, $\vec{\beta}$ is the shift vector (which in spherical symmetry has only radial component), and e^{χ} is the conformal factor. The 3-metric of the spacelike hypersurfaces is $\gamma_{ij} = e^{4\chi}\mathrm{diag}(a, br^2, br^2\sin^2\theta)$ and the lower radial component of $\vec{\beta}$ is given by $\beta_r = \gamma_{rr}\beta^r = e^{4\chi}a\beta^r$. Due to spherical symmetry, all functions depend on (t, r) only. The metric functions a and b were initialized in such a way that the conformal metric $\hat{\gamma}_{ij} = e^{-4\chi}\gamma_{ij}$ was flat, and then in the evolution we considered the condition

$$\partial_t\hat{\gamma} = (1-\sigma)\Big(2\hat{\gamma}\hat{\nabla}_m\beta^m\Big), \quad (2.22)$$

where $\hat{\gamma}$ is the determinant of $\hat{\gamma}_{ij}$, $\hat{\nabla}$ is the covariant derivative with respect to the conformal 3-metric, and σ is a parameter that is set to 0 for the so-called Eulerian evolution, and to 1 for the Lagrangian evolution [119]. In the simulations described in this chapter we used the latter.

We also introduced the scalar and vector electromagnetic potentials

$$\varphi = -n_\mu A^\mu, \quad (2.23)$$
$$a^i = \gamma^i{}_\mu A^\mu, \quad (2.24)$$

where $\gamma^\mu{}_\nu$ is the projector onto the foliation Σ_t, and n^μ is the orthogonal vector of Σ_t. The conjugate momenta of the real and complex scalar field are respectively defined as

$$\Pi = n^\mu\nabla_\mu\phi, \quad (2.25)$$
$$P = n^\mu\nabla_\mu\xi. \quad (2.26)$$

With these definitions we can rewrite Eqs. (2.16) and (2.17) as two sets of first-order equations:

$$\partial_t\phi = \beta^r\partial_r\phi + \alpha\Pi, \quad (2.27)$$
$$\partial_t\Pi = \beta^r\partial_r\Pi + \alpha\Pi K + \frac{(\partial_r\phi)(\partial_r\alpha)}{a\,e^{4\chi}} + \frac{1}{2}\alpha a\,e^{4\chi}(E^r)^2\frac{\delta F[\phi]}{\delta\phi}$$

$$+\frac{\alpha}{a\,e^{4\chi}}\Big[\partial_r^2\phi+(\partial_r\phi)\Big(\frac{2}{r}-\frac{\partial_r a}{2a}+\frac{\partial_r b}{b}+2\partial_r\chi\Big)\Big], \tag{2.28}$$

for the real scalar field ϕ, and

$$\partial_t\xi=\beta^r\partial_r\xi+\alpha P, \tag{2.29}$$

$$\partial_t P=\beta^r\partial_r P+\alpha PK+\frac{(\partial_r\xi)(\partial_r\alpha)}{a\,e^{4\chi}}+2iq\alpha\Big(\varphi P+\frac{a_r\partial_r\xi}{ae^{4\chi}}\Big)-q^2\alpha\Big(\frac{(a_r)^2}{ae^{4\chi}}-\varphi^2\Big)\xi$$
$$+\frac{\alpha}{a\,e^{4\chi}}\Big[\partial_r^2\xi+(\partial_r\xi)\Big(\frac{2}{r}-\frac{\partial_r a}{2a}+\frac{\partial_r b}{b}+2\partial_r\chi\Big)\Big], \tag{2.30}$$

for the complex scalar field ξ. Here K is the trace of the extrinsic curvature K_{ij}.

Due to spherical symmetry the magnetic field vanishes and the only nonvanishing component of the electric field and of the vector electromagnetic potential is the radial one. Fixing the gauge with the Lorenz condition $\nabla_\mu A^\mu=0$, it is possible to write the equations of motion for the electromagnetic field as

$$D_iE^i=-E^r(\partial_r\phi)\frac{1}{F[\phi]}\frac{\delta F[\phi]}{\delta\phi}+\frac{iq}{F[\phi]}\Big[-\xi^*P+\xi P^*+2iq\varphi|\xi|^2\Big], \tag{2.31}$$

$$\partial_tE^r=\alpha KE^r+\beta^r\partial_rE^r-E^r\partial_r\beta^r-\alpha\Pi E^r\frac{1}{F[\phi]}\frac{\delta F[\phi]}{\delta\phi}+\frac{\alpha}{F[\phi]}\frac{2q^2}{ae^{4\chi}}|\xi|^2a_r$$
$$+\frac{\alpha}{F[\phi]}\frac{iq}{ae^{4\chi}}\Big[\xi(\partial_r\xi)^*-\xi^*(\partial_r\xi)\Big], \tag{2.32}$$

$$\partial_ta_r=\beta^r\partial_ra_r+a_r\partial_r\beta^r-\partial_r(\alpha\varphi)-\alpha ae^{4\chi}E^r, \tag{2.33}$$

$$\partial_t\varphi=\beta^r\partial_r\varphi+\alpha\varphi K-\frac{(\partial_r\alpha)a_r}{ae^{4\chi}}-\frac{\alpha}{ae^{4\chi}}\Big[\partial_ra_r+a_r\Big(\frac{2}{r}-\frac{\partial_ra}{2a}+\frac{\partial_rb}{b}+2\partial_r\chi\Big)\Big], \tag{2.34}$$

where D_i is the covariant derivative with respect to the 3-metric γ_{ij}. Equations (2.31) and (2.32) have been obtained by projecting the field equation for the electromagnetic field (2.15) onto n^μ and onto Σ_t, respectively. The evolution equation for a_r has been obtained from the definition of the electric field $E^\nu=-n_\mu F^{\mu\nu}$, while Eq. (2.34) has been derived from the Lorenz gauge condition [75, 121].

For the gravitational field we used the equations of the generalized BSSN formalism in spherical symmetry [119, 120]. Introducing the traceless conformal extrinsic curvature $\hat{A}_{ij}=e^{-4\chi}(K_{ij}-\frac{1}{3}K\gamma_{ij})$, we defined $A_a=\hat{A}^r{}_r$ and $A_b=\hat{A}^\theta{}_\theta$. These two variables are not independent, since $\hat{A}_{ij}$ is traceless and $A_a+2A_b=0$, therefore we only evolved A_a. We also introduced the BSSN variable

$$\hat{\Delta}^i=\hat{\gamma}^{mn}(\hat{\Gamma}^i_{mn}-\mathring{\Gamma}^i_{mn}), \tag{2.35}$$

where $\hat{\Gamma}^i_{mn}$ and $\mathring{\Gamma}^i_{mn}$ are the Christoffel symbols of the conformal and the flat metrics, respectively.

Having fixed the notation, we can now write the evolution equations for the gravitational sector as

$$\partial_t\chi=\beta^r\partial_r\chi-\frac{1}{6}\alpha K+\frac{\sigma}{6}\hat{\nabla}_m\beta^m, \tag{2.36}$$

$$\partial_ta=\beta^r\partial_ra+2a\partial_r\beta^r-2\alpha aA_a-\frac{2}{3}\sigma a\hat{\nabla}_m\beta^m, \tag{2.37}$$

$$\partial_t b = \beta^r \partial_r b + 2b\frac{\beta^r}{r} - 2\alpha b A_b - \frac{2}{3}\sigma b \hat{\nabla}_m \beta^m, \tag{2.38}$$

$$\partial_t K = \beta^r \partial_r K - D^2\alpha + \alpha\Big(A_a^2 + 2A_b^2 + \frac{1}{3}K^2\Big) + 4\pi\alpha(S_a + 2S_b + \mathcal{E}), \tag{2.39}$$

$$\partial_t A_a = \beta^r \partial_r A_a + \alpha K A_a - \Big(D^r D_r \alpha - \frac{1}{3}D^2\alpha\Big) + \alpha(R^r{}_r - \frac{1}{3}R) - \frac{16\pi\alpha}{3}\Big(S_a - S_b\Big), \tag{2.40}$$

$$\begin{aligned}\partial_t \hat{\Delta}^r = {}& \beta^r \partial_r \hat{\Delta}^r - \hat{\Delta}^r \partial_r \beta^r + \frac{2}{b}\partial_r\Big(\frac{\beta^r}{r}\Big) + 2\alpha A_a \hat{\Delta}^r - 2\alpha\Big(A_a - A_b\Big)\frac{2}{br} \\ & - \frac{2}{a}\Big(A_a \partial_r \alpha + \alpha \partial_r A_a\Big) + \frac{1}{a}\partial_r^2 \beta^r + \frac{\sigma}{3}\Big[\frac{1}{a}\partial_r \hat{\nabla}_m \beta^m + 2\hat{\Delta}^r \hat{\nabla}_m \beta^m\Big] \\ & + \frac{2\alpha}{a}\Big[\partial_r A_a + \Big(A_a - A_b\Big)\Big(\frac{\partial_r b}{b} + \frac{2}{r}\Big) + 6A_a \partial_r \chi - \frac{2}{3}\partial_r K - 8\pi j_r\Big],\end{aligned} \tag{2.41}$$

where R_{ij} and R are respectively the Ricci tensor and the scalar curvature of the 3-metric γ_{ij}, and the constraint equations read

$$H = R + \frac{2}{3}K^2 - (A_a^2 + 2A_b^2) - 16\pi\rho = 0, \tag{2.42}$$

$$M = \partial_r A_a + \Big(A_a - A_b\Big)\Big(\frac{\partial_r b}{b} + \frac{2}{r}\Big) + 6A_a \partial_r \chi - \frac{2}{3}\partial_r K - 8\pi j_r = 0. \tag{2.43}$$

The source terms can be divided into three contributions:

- from the electromagnetic field we have

$$\mathcal{E}^{\rm EM} = n^\mu n^\nu T^{\rm EM}_{\mu\nu} = \frac{1}{8\pi} a\, e^{4\chi} (E^r)^2 F[\phi], \tag{2.44}$$

$$S^{\rm EM}_a = \Big({}^{(3)}T^{\rm EM}\Big)^r{}_r = -\frac{1}{8\pi} a\, e^{4\chi} (E^r)^2 F[\phi], \tag{2.45}$$

$$S^{\rm EM}_b = \Big({}^{(3)}T^{\rm EM}\Big)^\theta{}_\theta = \frac{1}{8\pi} a\, e^{4\chi} (E^r)^2 F[\phi], \tag{2.46}$$

- from the real scalar field we have

$$\mathcal{E}^{\rm SF} = n^\mu n^\nu T^{\rm SF}_{\mu\nu} = \frac{1}{8\pi}\Big(\Pi^2 + \frac{(\partial_r \phi)^2}{a\, e^{4\chi}}\Big), \tag{2.47}$$

$$j^{\rm SF}_r = -\gamma^\mu{}_r n^\nu T^{\rm SF}_{\mu\nu} = -\frac{1}{4\pi}\Pi \partial_r \phi, \tag{2.48}$$

$$S^{\rm SF}_a = \Big({}^{(3)}T^{\rm SF}\Big)^r{}_r = \frac{1}{8\pi}\Big(\Pi^2 + \frac{(\partial_r \phi)^2}{a\, e^{4\chi}}\Big), \tag{2.49}$$

$$S^{\rm SF}_b = \Big({}^{(3)}T^{\rm SF}\Big)^\theta{}_\theta = \frac{1}{8\pi}\Big(\Pi^2 - \frac{(\partial_r \phi)^2}{a\, e^{4\chi}}\Big), \tag{2.50}$$

- and from the complex scalar field

$$\mathcal{E}^\xi = n^\mu n^\nu T^\xi_{\mu\nu} = \frac{1}{4\pi}\Big(|\tilde{P}|^2 + \frac{|\tilde{\Psi}|^2}{a\, e^{4\chi}}\Big), \tag{2.51}$$

$$j^\xi_r = -\gamma^\mu{}_r n^\nu T^\xi_{\mu\nu} = -\frac{1}{4\pi}\Big(\tilde{\Psi}\tilde{P}^* + \tilde{P}\tilde{\Psi}^*\Big), \tag{2.52}$$

$$S_a^\xi = \Big({}^{(3)}T^\xi\Big)^r{}_r = \frac{1}{4\pi}\Big(|\tilde{P}|^2 + \frac{|\tilde{\Psi}|^2}{a\,e^{4\chi}}\Big), \tag{2.53}$$

$$S_b^\xi = \Big({}^{(3)}T^\xi\Big)^\theta{}_\theta = \frac{1}{4\pi}\Big(|\tilde{P}|^2 - \frac{|\tilde{\Psi}|^2}{a\,e^{4\chi}}\Big), \tag{2.54}$$

where $\tilde{P}$ and $\tilde{\Psi}$ are defined as

$$\tilde{P} = n^\mu \mathcal{D}_\mu \xi = n^\mu \nabla_\mu \xi + iqn^\mu A_\mu \xi = P - iq\varphi\xi, \tag{2.55}$$

$$\tilde{\Psi} = \gamma^\mu{}_r \mathcal{D}_\mu \xi = \gamma^\mu{}_r \nabla_\mu \xi + iq\gamma^\mu{}_r A_\mu \xi = \partial_r \xi + iqa_r \xi. \tag{2.56}$$

Note that, for practical reasons, in our code we evolved the variable $e^{-2\chi}$ instead of χ.

For the evolution of the lapse function we used the nonadvective 1+log slicing condition [122]

$$\partial_t \alpha = -2\alpha K, \tag{2.57}$$

while for the shift we used the Gamma-driver condition [120,123]; namely we defined a new variable B^r such that

$$\partial_t B^r = \frac{3}{4}\partial_t \hat{\Delta}^r, \tag{2.58}$$

$$\partial_t \beta^r = B^r. \tag{2.59}$$

2.3.3 Electric charge in Einstein-Maxwell-scalar theory

Due to the nonminimal coupling, in this theory it is possible to define the electric charge in two different ways. The equation for the electromagnetic field can in fact be written as $\nabla_\mu F^{\mu\nu} = -4\pi J^\nu_{\rm EM}$, where

$$J^\nu_{\rm EM} = \frac{1}{4\pi}\Big\{\frac{1}{F[\phi]}\frac{\delta F[\phi]}{\delta\phi}(\nabla_\mu\phi)F^{\mu\nu} - \frac{iq}{F[\phi]}\Big[\xi(\mathcal{D}^\nu\xi)^* - \xi^*(\mathcal{D}^\nu\xi)\Big]\Big\}, \tag{2.60}$$

but also as $\nabla_\mu\Big(F[\phi]F^{\mu\nu}\Big) = -4\pi\tilde{J}^\nu_{\rm EM}$, where

$$\tilde{J}^\nu_{\rm EM} = -\frac{iq}{4\pi}\Big[\xi(\mathcal{D}^\nu\xi)^* - \xi^*(\mathcal{D}^\nu\xi)\Big]. \tag{2.61}$$

Both these two currents are conserved, namely $\nabla_\mu J^\mu_{\rm EM} = 0 = \nabla_\mu \tilde{J}^\mu_{\rm EM}$, and allow to define the electric charge in two ways:

$$Q = \frac{1}{4\pi}\int_V dV D_i E^i = \int_V dV \rho, \tag{2.62}$$

$$\tilde{Q} = \frac{1}{4\pi}\int_V dV D_i (F[\phi]E^i) = \int_V dV \tilde{\rho}, \tag{2.63}$$

where the two charge densities are

$$\rho = -n_\mu J^\mu_{\rm EM} = \frac{1}{4\pi}\Big\{-E^r(\partial_r\phi)\frac{1}{F[\phi]}\frac{\delta F[\phi]}{\delta\phi} + \frac{iq}{F[\phi]}\Big[-\xi^* P + \xi P^* + 2iq\varphi|\xi|^2\Big]\Big\}, \tag{2.64}$$

$$\tilde{\rho} = -n_\mu \tilde{J}^\mu_{\rm EM} = \frac{iq}{4\pi}\Big[-\xi^* P + \xi P^* + 2iq\varphi|\xi|^2\Big]. \tag{2.65}$$

As it can be seen from the above equations, while the charge Q includes the contribution of the real scalar field, $\tilde{Q}$ accounts only for the charge carried by the complex field ξ. In Einstein-Maxwell theory ($F[\phi] = 1$) or when the scalar field vanishes ($F[\phi = 0] = 1$), the two charges coincide, as expected.

For a spherically symmetric spacetime, following [75], we can define the electric charge enclosed in the 2-sphere S_r of radius r in two ways:

$$\begin{aligned} Q(r) &= \int_{S_r} dV\rho = \frac{1}{4\pi}\int_{S_r} dV D_i E^i = \frac{1}{4\pi}\int_{\partial S_r} dS\, s_i E^i = \sqrt{a}be^{6\chi}r^2 E^r, \\ \tilde{Q}(r) &= \int_{S_r} dV\tilde{\rho} = \frac{1}{4\pi}\int_{S_r} dV D_i(F[\phi]E^i) = \frac{1}{4\pi}\int_{\partial S_r} dS\, s_i E^i F[\phi] \\ &= F[\phi]\sqrt{a}be^{6\chi}r^2 E^r, \end{aligned} \tag{2.66}$$

where s^i is the outward pointing unit vector normal to ∂S_r. Note that, although I only made the radial dependence explicit, the above quantities can generically depend also on the time coordinate.

We can see that the electric field can be written as

$$E^r = \frac{Q(r)}{b\sqrt{a}e^{6\chi}r^2} = \frac{\tilde{Q}(r)}{F[\phi]b\sqrt{a}e^{6\chi}r^2}. \tag{2.67}$$

and that the two definitions of charge can be related by

$$Q(r) = \frac{\tilde{Q}(r)}{F[\phi]}. \tag{2.68}$$

For a spherically symmetric BH spacetime with a vanishing complex scalar field, $\tilde{Q}$ is homogeneous outside the horizon, while Q is in general a radial function. For a scalarized configuration there is a nonvanishing charge density ρ outside the BH and the total charge of the system does not coincide with the charge enclosed in the horizon. However, the two charges coincide at infinity since we have always assumed asymptotic flatness and hence $\phi \to 0$ and $F[\phi] \to 1$ and $r \to +\infty$.

2.3.4 Numerical integration scheme

In our framework the equations of motion are regular at the origin, but contain terms that go as $\frac{1}{r}$ and $\frac{1}{r^2}$, that can cause instabilities in the numerical integration. To handle these terms we used the second-order Partially Implicitly Runge-Kutta (PIRK) method [124, 125], which does not require the implementation of an explicit regularization procedure at the origin. This allowed us to integrate the equations that contain unstable terms with a partially implicit method, while the other equations could be integrated with an explicit method. The details of this implementation can be found in Appendix B.1.

For the numerical radial derivatives we used the fourth-order accurate centered finite differences method, except for the advection terms (which are of the form $\beta^r\partial_r$) for which we used the upwind scheme. In order to avoid the appearance of high-frequencies instabilities in the evolution, we added to all the equations a

Kreiss-Oliger dissipation term, that we evolved explicitly; in this term the fourth derivative has been computed with second-order accuracy. In Appendix B.2 I show the numerical convergence of our code.

2.3.5 Initial conditions

Since our purpose was to study the collapse of a charged scalar field and the possibility of forming overcharged BH solutions, we chose an initial profile for ξ that carries a nonvanishing amount of electric charge and propagates toward the horizon:

$$\begin{aligned}\xi(r,t=0) &= B_0 e^{-\frac{1}{2}\sigma_\xi^2 (r-r_{0,\xi})^2 + i k_0 (r-r_{0,\xi})},\\ P(r,t=0) &= i B_0 e^{-\frac{1}{2}\sigma_\xi^2 (r-r_{0,\xi})^2 + i k_0 (r-r_{0,\xi})} \left(k_0 + i\sigma_\xi^2 (r-r_0)\right),\end{aligned} \tag{2.69}$$

where B_0, σ_ξ^{-1}, k_0, and $r_{0,\xi}$ are respectively the amplitude, width, frequency, and position of the initial profile of the complex scalar field.

We chose a vanishing initial shift and a flat conformal 3-metric. We set to zero the auxiliary variable B^r and the radial component of the traceless extrinsic curvature A_a, while we initialized $\hat{\Delta}^r$ using its definition in Eq. (2.35), which in spherical symmetry reduces to [120]

$$\hat{\Delta}^r = \frac{1}{a}\left[\frac{\partial_r a}{2a} - \frac{\partial_r b}{b} - \frac{2}{r}\left(1-\frac{a}{b}\right)\right]. \tag{2.70}$$

To find the initial profile of the electric field, the trace of the extrinsic curvature, and the conformal factor we solved Eq. (2.31) together with the Hamiltonian and momentum constraints. We also initialized the electromagnetic potentials to a configuration such that both φ and a_r do not evolve in a region sufficiently far from the horizon as long as the signals do not reach the outer boundary. To achieve this we set $a_r = 0$ at $t = 0$, and we determined the profile of φ by solving the equation $\partial_t a_r = 0$ which, using Eq. (2.33), reduces to $\partial_r(\alpha\varphi) = -\alpha a e^{4\chi} E^r$.

The system of equations that we solved at $t = 0$ for E^r, K, φ, and $\psi := e^\chi$ reads

$$\begin{aligned}\partial_r^2\psi = \frac{1}{48 r^2 a b^2}\Big\{ & 2a^2 b\psi\big[r^2 b\psi^4(-48\pi\mathcal{E} + 2K^2) + 6\big] + 6r(\partial_r a) b\big[r(\partial_r b)\psi \\ & + 2b(2r(\partial_r\psi) + \psi)\big] - 3a\Big[-r^2(\partial_r b)^2\psi + 4b^2\left(8r(\partial_r\psi) + \psi\right) \\ & + 4rb\Big(4r(\partial_r b)(\partial_r\psi) + \left(3\partial_r b + r\partial_r^2 b\right)\psi\Big)\Big]\Big\},\end{aligned} \tag{2.71}$$

$$\begin{aligned}\partial_r E^r = & -\left(\frac{\partial_r a}{2a} + \frac{\partial_r b}{b} + 6\frac{\partial_r\psi}{\psi} + \frac{2}{r}\right)E^r + 2q\frac{\xi_R P_I - \xi_I P_R}{F[\phi]} - 2q^2\varphi\frac{|\xi|^2}{F[\phi]} \\ & - E^r(\partial_r\phi)\frac{1}{F[\phi]}\frac{\delta F[\phi]}{\delta\phi},\end{aligned} \tag{2.72}$$

$$\partial_r K = 6\big[P_R\partial_r\xi_R + P_I\partial_r\xi_I - q\varphi(\xi_R\partial_r\xi_I - \xi_I\partial_r\xi_R)\big], \tag{2.73}$$

$$\partial_r\varphi = -\frac{\partial_r\alpha}{\alpha}\varphi - a\psi^4 E^r, \tag{2.74}$$

where the subscripts X_R and X_I denote the real and imaginary part of a complex variable X, respectively.

2.3.6 Boundary conditions

Thanks to the PIRK integration method at the origin we only imposed the parity conditions related to the spherical symmetry. Therefore we shifted the numerical grid in such a way that the origin was placed in the middle of a grid step, and the first grid point was at $r_1 = \frac{\Delta r}{2}$, where Δr is the grid step. To compute the numerical derivatives at r_1 and r_2 we added two ghost grid points at $r_{-1} = -\frac{\Delta r}{2}$ and $r_{-2} = -\frac{3\Delta r}{2}$ in which the variables were not evolved but were set at each time step to values that satisfied the parity conditions. In particular β^r, E^r, B^r, a_r, and $\hat{\Delta}^r$ have odd parity at the origin while all the other variables have even parity.

At the outer boundary we added four ghost zones which were used to compute the fourth-order accurate upwind derivatives. In these zones the variables were not evolved and they remained constant. This could be done since we considered an initial profile of φ such that the electromagnetic potentials did not evolve at the outer boundary as long as the signals coming from the horizon region were sufficiently far from the outer boundary, and we considered a domain large enough that outward-moving components of the initial field profiles did not reach the outer boundary during the time of integration.

2.4 Results

2.4.1 Collapse of the charged field in a flat background in Einstein-Maxwell theory

We started by neglecting the real field ($\phi = 0$, $F[0] = 1$) and studied the collapse of the complex scalar field in flat spacetime in Einstein-Maxwell theory, in order to explore the RN BH formation and the robustness of the cosmic censorship hypothesis in the standard case. This problem was studied in [75] using momentarily static charged wave packets as the initial data. In that case it was possible to form a RN BH with final charge-to-mass ratio as large as $Q/M \sim 0.6$, therefore still far from extremality. In our simulation, we started from an ingoing charged wave packet, so that we could form a BH with higher charge, which is a more stringent test of the cosmic censorship.

Initial setup

We defined an arbitrary mass scale M to normalize all dimensionful quantities. We chose the parameters in Eq. (2.69) in such a way that the initial profile of ξ is narrow enough to obtain final configurations in which the (possibly formed) final BH is close to extremality. In particular we set

$$\begin{aligned} &B_0 = 0.012\,, \quad k_0 M = 5\,, \\ &\sigma_\xi^2 M^2 = 2.5\,, \quad r_{0,\xi}/M = 5\,. \end{aligned} \tag{2.75}$$

For this initial configuration the simulation was computationally demanding: high resolution and a low Courant–Friedrichs–Lewy (CFL) factor were required. Therefore in order to obtain higher accuracy without increasing excessively the

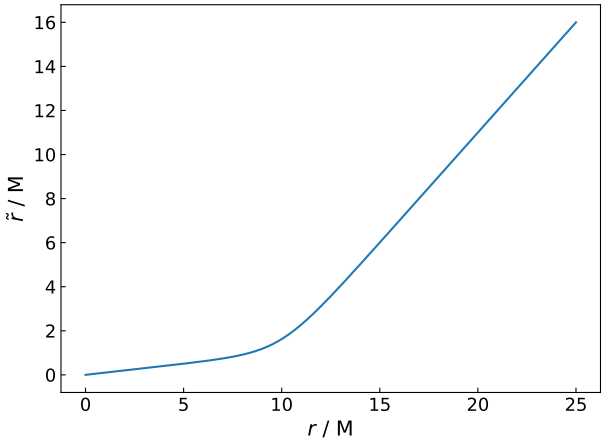

Figure 2.2. Coordinate transformation for the nonuniform grid step. Near the origin small regions in the (original) $\tilde{r}$ domain are mapped to large regions of the (new) r domain. Sufficiently far from the origin the two coordinates differ only by a constant.

computational cost, we used a nonuniform grid step by performing the following transformation on the radial coordinate:

$$\begin{cases} \tilde{r} & = C(r) = r + \frac{1-\eta}{\Delta} \ln\left(\frac{1+e^{-\Delta(r-R_1)}}{1+e^{\Delta R_1}}\right) \\ \frac{\partial \tilde{r}}{\partial r} & = C'(r) = \eta + \frac{1-\eta}{1+e^{-\Delta(r-R_1)}} \end{cases}, \tag{2.76}$$

where we renamed the new radial coordinate as r and the old one as $\tilde{r}$. In the above equation, R_1 and Δ are the typical radius and typical width of the buffer zone between the area around the origin that requires the higher numerical resolution and the asymptotic region, whereas η characterizes the relative scale of the resolution. The parameters have been set to $\eta = 0.1$, $\Delta = 1/M$ and $R_1 = 10M$. The behavior of $\tilde{r}$ vs r is shown in Fig. 2.2, where it can be seen that a small region around the center in the old coordinate $\tilde{r}$ is mapped to a larger region in the new coordinates. In this way the horizon of a final BH which is close to extremality is placed at a higher value of r allowing for higher accuracy with a larger grid step. On the other hand $C'(r) \sim 1$ for $r \gg R_1$, and the two radial coordinates differ only by a constant near the outer boundary. After this change of coordinates the metric functions a and b of the flat spacetime are:

$$a(r, t = 0) = C'(r)^2, \tag{2.77}$$

$$b(r, t = 0) = \frac{C(r)^2}{r^2}, \tag{2.78}$$

and the initial profile of $\hat{\Delta}^r$ has been set according to Eq. (2.70).

The lapse function α was initialized by imposing that $\partial_t K = 0$ at $t = 0$, therefore we integrated numerically the equation

$$\partial_r^2 \alpha = (\partial_r \alpha)\left[\frac{\partial_r a}{2a} - \frac{\partial_r b}{b} - 2\frac{\partial_r \psi}{\psi} - \frac{2}{r}\right] + \psi^4 \alpha a \frac{K^2}{3} + 4\pi\alpha\psi^4 a(\mathcal{E} + S_a + 2S_b) \tag{2.79}$$

together with Eq. (2.71)-(2.74). To solve the equations for the initial profile we used a shooting procedure starting the numerical integration from the origin and moving outwards. We imposed regularity at $r = 0$ and the asymptotic behaviors

$$\begin{aligned}
\psi &:= e^{\chi} = 1 + \frac{M_{\rm ADM}}{2\tilde{r}} + \mathcal{O}\Big(\frac{1}{\tilde{r}^2}\Big), \\
K &= \mathcal{O}\Big(\frac{1}{\tilde{r}^3}\Big), \\
\varphi &= \frac{Q_\infty}{\tilde{r}} + \mathcal{O}\Big(\frac{1}{\tilde{r}^3}\Big), \\
\alpha &= 1 - \frac{M_{\rm ADM}}{\tilde{r}} + \mathcal{O}\Big(\frac{1}{\tilde{r}^2}\Big),
\end{aligned} \tag{2.80}$$

where $M_{\rm ADM}$ is the Arnowitt-Deser-Misner (ADM) mass, and $Q_\infty = Q(r_\infty)$ is the electric charge computed at the outer boundary. We performed the numerical integration using the Runge-Kutta method at the fourth order of accuracy, and the Newton's method as a root-finding algorithm in the shooting procedure. At the end of the initialization process we computed the ADM mass and electric charge at the outer boundary.

We used a numerical grid that extends from the origin up to $\frac{r}{M} = 40$, with a grid step $\frac{\Delta r}{M} = 0.005$. We integrated the equations up to $\frac{T}{M} = 24$, and the CFL factor was set to $\text{CFL} = \frac{\Delta t}{\Delta r} = 0.01$. Note that since we employed a radial transformation, in the central region Δr was approximately 10 times larger than the corresponding step in the old radial coordinate $\Delta\tilde{r}$. The time step Δt had then to be chosen accordingly, leading to small values of the CFL factor.

Results of the simulations

We performed the numerical integration of the evolution equations for different values of $qM \in [0, 10]$, and studied the BH formation by computing the position of the apparent horizon, $r = r_{\rm AH}$. For the cases in which the collapse has happened we computed the horizon charge as

$$Q_{\rm AH} = r^2 b\sqrt{a} E^r e^{6\chi}\Big|_{r=r_{\rm AH}}, \tag{2.81}$$

and the horizon mass using the Christodoulou-Ruffini mass formula [126] in the case of vanishing spin:

$$M_H = M_{\rm irr} + \frac{Q_{\rm AH}^2}{4M_{\rm irr}}, \tag{2.82}$$

where $M_{\rm irr} = \sqrt{\frac{A_H}{16\pi}}$ is the irreducible mass and A_H is the apparent horizon area.

The use of these formulas for the horizon mass and charge is based on the assumptions that the end state of the possible gravitational collapse is described by the RN metric and the final configuration is approximately stationary near the origin at $t = T$. The first assumption is guaranteed by the uniqueness of the RN solution in Einstein-Maxwell theory, while the second assumption is satisfied for the value of T that we chose.

We then computed the initial (at $t = 0$) charge-to-mass ratio of the full spacetime, $\bar{Q}_i^{\rm ST} = \frac{Q_\infty}{M_{\rm ADM}}$, and the charge-to-mass ratio of the final BH, $\bar{Q}_f^{\rm BH} = \frac{Q_{\rm AH}}{M_{\rm AH}}$, at

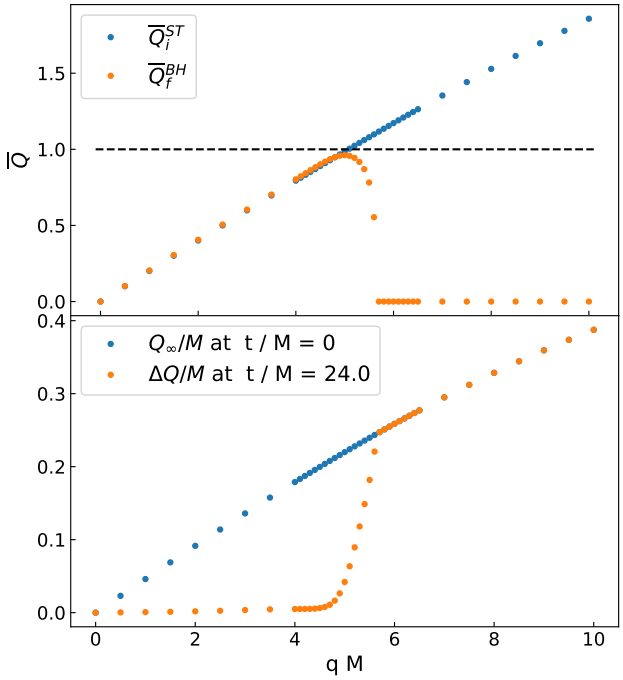

Figure 2.3. Upper panel: total charge-to-mass ratio of the spacetime at $t = 0$ (blue) and charge-to-mass ratio of the final BH at $t = T$ (orange) as functions of the fundamental charge q of the initial ingoing wave packet. **Lower panel**: total charge in the spacetime at $t = 0$ (blue) and amount of charge ΔQ outside the horizon at $t = T$ (orange) as functions of q. For low values of q almost all the initial pulse collapses and forms the final BH, for $qM \sim 5$ the charge-to-mass ratio of the final BH reaches its maximum value and then decreases, due to the electromagnetic interaction that starts becoming dominant; finally, for $qM \gtrsim 5.65$ the gravitational collapse stops occurring, and there is no formation of a horizon. This condition conventionally corresponds to $\bar{Q}_f^{\rm BH} = 0$ (i.e., $\Delta Q = Q_\infty$).

$t = T$. The results are shown in the upper panel of Fig. 2.3. For $qM \lesssim 4.5$ almost all the scalar field present at the beginning of the simulation collapses and forms the final BH. When $qM \sim 5$ the final configuration is close to extremality but the BH remains subextremal. For $qM \gtrsim 5$ the charge-to-mass ratio of the spacetime at $t = 0$ exceeds unity and the electric forces start preventing the gravitational collapse: $\bar{Q}_f^{\rm BH}$ rapidly decreases until $qM \sim 5.65$, where a BH stops forming. As a convention, in the plot we set $\bar{Q}_f^{\rm BH} = 0$ for the cases in which a horizon does not form. The maximum value of the BH charge-to-mass ratio that we obtained in our simulations is $\bar{Q}_f^{\rm BH} \sim 0.96$.

We also computed the amount of charge outside the final BH, ΔQ, obtained by subtracting the horizon charge to the final charge computed at the outer boundary, and we compared it with the total electric charge at $t = 0$; the results are shown in the lower panel of Fig. 2.3. For $qM \lesssim 4.5$ almost all the charge present in the initial pulse is enclosed in the horizon, then the amount of charge outside horizon starts increasing, and for $qM \gtrsim 5.65$ it coincides with the initial charge of the spacetime, since for these values of q the electromagnetic interaction is strong enough

to completely prevent the gravitational collapse.

2.4.2 Collapse of the charged field towards a RN BH in Einstein-Maxwell theory

Next, we considered the collapse of the complex scalar field towards a RN BH within Einstein-Maxwell theory, attempting at overcharge it. As I will show, not only this allows to reach final BHs which are closer to extremality, but the process shows also superradiant amplification at full nonlinear level.

Initial setup

In this case the initial configuration of the system is given by a complex scalar field on a RN background. The parameters of the initial profile of ξ are:

$$\begin{aligned} &B_0 = 0.002\,, \quad k_0 M = 5\,, \\ &\sigma_\xi^2 M^2 = 2.5\,, \quad r_{0,\xi}/M = 20\,, \end{aligned} \tag{2.83}$$

where in this case M is set to be equal to the initial BH mass, $M_{\rm BH} = M$, and all dimensionful quantities are measured in terms of M.

For this analysis we wished to construct a background configuration such that the mass and the charge of the central BH were fixed as q varies. In order to achieve this we implemented a shooting algorithm that integrates Eqs. (2.71)-(2.74) starting from the outer boundary and moving inward, and searches for the parameters $M_{\rm ADM}$ (the ADM mass) and Q in the asymptotic expansions

$$\begin{aligned} E^r &= \frac{Q}{r^2} + \mathcal{O}\Big(\frac{1}{r^3}\Big), \\ \psi := e^\chi &= 1 + \frac{M_{\rm ADM}}{2r} - \frac{Q^2}{8r^2} + \mathcal{O}\Big(\frac{1}{r^3}\Big), \\ K &= \mathcal{O}\Big(\frac{1}{r^3}\Big), \\ \varphi &= \frac{Q}{r} + \mathcal{O}\Big(\frac{1}{r^3}\Big)\,, \end{aligned} \tag{2.84}$$

such that the horizon charge and mass assume the required values. We used a precollapsed lapse [123] $\alpha = \frac{1}{\psi^2}$, and a conformal metric with $a = b = 1$, while the horizon mass was computed with the Christodoulou-Ruffini mass formula. After the initialization we extracted the total ADM mass and electric charge at the outer boundary.

The BH initial charge-to-mass ratio was set to $\bar{Q}_i^{\rm BH} = \frac{Q_i^{\rm BH}}{M_i^{\rm BH}} = \{0.9, 0.95, 0.99\}$. The numerical grid extends from the origin up to $\frac{r_\infty}{M} = 250$ with a grid step $\frac{\Delta r}{M} = 0.01$, and the CFL factor was CFL $= 0.4$. The final time of integration was set to $\frac{T}{M} = 100$, which is sufficient to obtain an approximately stationary final configuration near the horizon.

Results of the simulations

After the integration of the evolution equations for values of $qM \in [0, 20]$, we computed the charge-to-mass ratio of the final BH, $\bar{Q}_f^{\rm BH}$. We plotted the results in the upper panel of Fig. 2.4, where the dots represent $\bar{Q}_f^{\rm BH}$ while the crosses represent the initial charge-to-mass ratio of the entire spacetime, $\bar{Q}_i^{\rm ST}$. For low values of q the charge carried by the complex field is smaller than its mass, the initial pulse is totally absorbed by the BH and $\bar{Q}_f^{\rm BH}$ is smaller than $\bar{Q}_i^{\rm BH}$. As q increases the final charge-to-mass ratio increases, then reaches a maximum and starts decreasing, without producing overcharged final configurations. In this experiment, the maximum charge-to-mass ratio of the final BH achieved in our simulation is $\bar{Q}_f^{\rm BH} \sim 0.986$.

Interestingly, this is not only due to the increasing electromagnetic repulsion that overcomes the gravitational attraction, but there is also another mechanism at play. In fact for sufficiently high values of the parameter q the BH mass decreases during the evolution, as it can be seen from the middle panel of Fig. 2.4, where I show the behavior of the difference between the final and the initial BH mass as a function of q. Such behavior hints to the presence of superradiance [72], a mechanism that allows charge and mass extraction from a BH, analogous to the one described in Chapter 4.

For a monochromatic test field on a RN background the condition for superradiance to take place is [72]

$$\omega < q\Phi_H, \tag{2.85}$$

where ω is the wave frequency and Φ_H is the horizon electric potential. Therefore at a fixed frequency the superradiance condition (2.85) is met for values of q which are above the threshold $q_{\rm th} = \frac{\omega}{\Phi_H}$. Since we are not considering a monochromatic test field the superradiance condition is more involved, because the initial wave packet contains both frequencies that satisfy Eq. (2.85) and higher frequencies which are instead absorbed by the BH. Nonetheless, we made an estimate of the threshold value $q_{\rm th}$ using $\omega = k_0$, where k_0 is the frequency in the initial profile of ξ, and the horizon electric potential of a RN BH $\Phi_H = \frac{Q_{\rm AH}}{R_H}$, where R_H is the horizon areal radius; the results are summarized in Table 2.1. As we can see the threshold values that we obtained are compatible with the behaviors in the middle panel of Fig. 2.4, since they fall in the region where the difference between the final and initial BH mass is decreasing. Furthermore, the threshold value of q decreases with $\bar{Q}_i^{\rm BH}$, as expected. It is worth mentioning that the energy of the initial complex field is $\sim 0.1M$, so backreaction is relevant and the expectations from linear perturbation theory are only indicative. Nonetheless, by comparing the top and middle panels in Fig. 2.4, it is interesting to notice that the maximum of the final charge-to-mass ratio roughly corresponds to the BH mass extraction, suggesting that (nonlinear) superradiance plays an important role in preserving the cosmic censorship in Einstein-Maxwell theory. I will come back to this point later when discussing a similar gedanken experiment in Einstein-Maxwell-scalar theory.

Finally, in order to check the behavior of the entropy, in the lower panel of Fig. 2.4 we plotted difference between the final and initial BH area. We can see that this value is always positive, in agreement with the BH area law in GR.

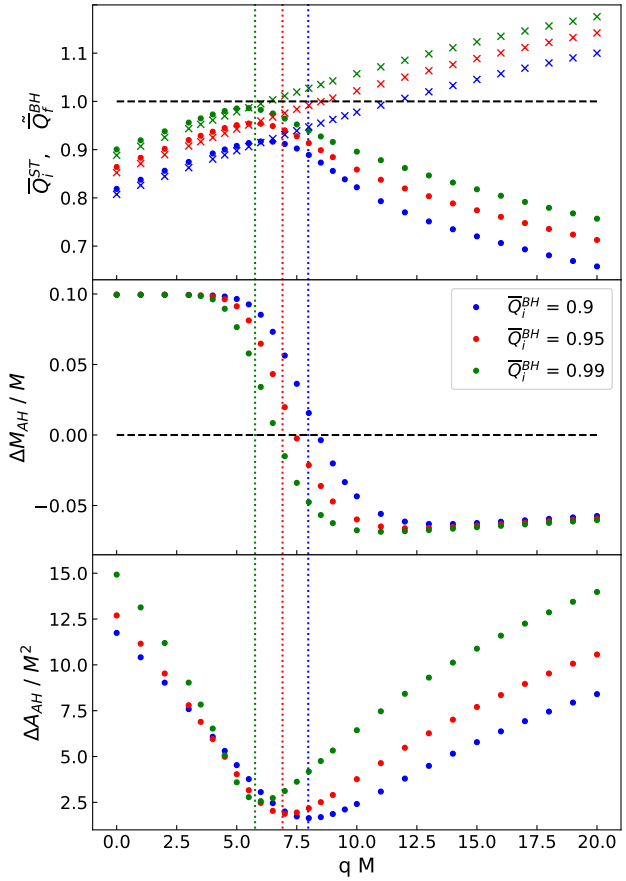

Figure 2.4. *Cosmic censorship at play in Einstein-Maxwell theory.* **Upper Panel**: Charge-to-mass ratio $\bar{Q}_f^{\rm BH}$ of the final BH (dots) and total charge-to-mass ratio $\bar{Q}_i^{\rm ST}$ of the spacetime at the beginning of the simulations (crosses) for the collapse in Einstein-Maxwell theory. For low values of q the incoming pulse is absorbed by the BH, and $\bar{Q}_f^{\rm BH}$ increases with q, while for higher values of q it decreases due to the electric repulsion and superradiance. Final configurations with an overcharged BH have never been produced. **Middle Panel**: Change of the BH mass during the simulation. For high values of q superradiance takes place and extracts mass from the initial BH. **Lower Panel**: In all simulations the BH area increases, in agreement with the BH area law. The dotted lines in the three panels correspond to the threshold values for the superradiance condition summarized in Table 2.1.

$\bar{Q}_i^{\rm BH}$	Φ_H	$q_{\rm th}M$
0.9	0.63	8.0
0.95	0.72	6.9
0.99	0.87	5.8

Table 2.1. Estimates of the threshold values of the parameter $q_{\rm th}$ from the superradiance condition 2.85. For Φ_H we used the horizon electric potential of a RN BH, $\Phi_H = \frac{Q_{\Delta \rm H}}{R_H}$, and for ω we used the frequency k_0 in the initial profile of the complex scalar field.

2.4.3 Collapse of charged field towards a RN BH in nonminimally-coupled Einstein-Maxwell-scalar theory

Let us now focus on the collapse in Einstein-Maxwell-scalar theory with nonminimal couplings.

Challenging the cosmic censorship I: dynamical formation of scalarized charged BHs

We started by studying the dynamical formation of overcharged BHs in the presence of a nonminimal coupling. We set the coupling parameter to $\lambda = -500$ in such a way that the dynamics of the spontaneous scalarization was sufficiently fast and the computational cost of the simulation was moderate.

The setup of our gedanken experiment was the following. We should initially throw a small real scalar field onto a RN BH in a region of the parameter space in which the BH is unstable and scalarizes. We then threw a second wave packet (this time made of a charged scalar field) which reached the BH on longer time scales, i.e. when the BH was reaching a stationary configuration. Given the separation of scales, our setup was similar to trying to overcharge a hairy charged BH from the onset.

Thus, we wished to construct the initial configurations in such a way that the complex scalar field reached the horizon sufficiently after the real scalar field. To this aim we used the same parameters as in the previous analysis for the initial profile of ξ and we initialized ϕ and Π to

$$\begin{aligned} \phi(r, t=0) &= A_0 \exp\left[-\frac{(r-r_0)^2}{\sigma_0^2}\right], \\ \Pi(r, t=0) &= 0, \end{aligned} \tag{2.86}$$

where $A_0 = 0.0003$, $r_0/M = 10$ and $\sigma_0/M = \sqrt{8}$. This initial profile coincides with the one used in Ref. [76]. Note that the amplitude of ϕ could be small since, owing to the tachyonic instability, the real scalar field initially grows exponentially during scalarization. We adopted the same initialization procedure as in the previous section, with the difference that in this case the equations contain also the terms depending on ϕ as well as the corresponding dynamical equation for it. Initially, the real scalar field has negligible support near the BH so we can consider the latter to be initially described by the RN metric. The grid parameters, the time step, and the end time of the simulations were set to the same values as in the previous section.

During the evolution we obtained stable hairy BHs with nonvanishing profiles of the real scalar field. To compute the mass of the scalarized BHs we could not use Eq. (2.82), since it is based on the hypothesis that the BH is described by the RN metric. An alternative strategy for extracting the mass could have been to integrate the evolution equations for longer times, in such a way that the real scalar field profile of the final BH reached a region of the spacetime large enough to compute the ADM mass explicitly. However this procedure would have been computationally expensive, since it would have required large numerical grids and larger integration

times. We instead checked that at $t = T$ the system had reached its final configuration near the horizon while the contribution from the complex scalar field could be neglected. In this case we could use the horizon data to construct a static scalarized BH solution from which we could then compute the ADM mass. This procedure heavily reduced the computational cost since it did not require to evolve the full system of equations for very long times.

To construct the stationary configuration we integrated the field equations of EMS gravity in Schwarzschild-like coordinates, which have been obtained by Herdeiro *et al.* in Ref. [76]. In particular, we used the following ansatz for the metric:

$$ds^2 = -\Big(1 - \frac{2m(R)}{R}\Big)e^{-2\delta(R)}dt^2 + \frac{dR^2}{1 - \frac{2m(R)}{R}} + R^2 d\Omega^2 \,, \tag{2.87}$$

where R is the areal radius, $m(R)$, and $\delta(R)$ are metric functions. Furthermore we assumed a time-independent profile for the scalar field $\phi = \phi(R)$, and a electromagnetic 4-potential of the form $A_\mu = (A_t(R), 0, 0, 0)$. Plugging these expressions into the field equations we obtained the system:

$$\partial_R A_t = \frac{e^{-\delta}\tilde{Q}}{F[\phi]R^2} \,, \tag{2.88}$$

$$\partial_R m = \frac{R^2}{2}\left[\left(1 - \frac{2m}{R}\right)\left(\partial_R\phi\right)^2 + e^{2\delta}F[\phi]\left(\partial_R A_t\right)^2\right] \,, \tag{2.89}$$

$$\partial_R \delta = -R\left(\partial_R\phi\right)^2 \,, \tag{2.90}$$

$$\begin{aligned}\partial_R^2\phi = &-\frac{1}{1 - \frac{2m}{R}}\left[\frac{1}{2}e^{2\delta}F'[\phi]\left(\partial_R A_t\right)^2 - \left(\frac{2}{R}\right)\left(\partial_R\phi\right)\left(\partial_R m - \frac{m}{R}\right)\right] \\ &- \frac{\left(\partial_R\phi\right)}{R}\left(2 + R^2\left(\partial_R\phi\right)^2\right) \,,\end{aligned} \tag{2.91}$$

where $\tilde{Q}$ is the charge excluding the effect of the real scalar field (see Sec. 2.3.3).

At the horizon $m(R_H) = \frac{R_H}{2}$, and, as a consequence, the denominator in (2.91) vanishes. In order to restore regularity we had to impose

$$\partial_R\phi(R_H) = \frac{1}{2R_H}F'[\phi(R_H)]\frac{\tilde{Q}^2}{\tilde{Q}^2 F[\phi(R_H)] - F[\phi(R_H)]^2 R_H^2} \,. \tag{2.92}$$

At spatial infinity instead we had the following asymptotic behaviors

$$\begin{aligned} m &= M - \frac{\tilde{Q}^2 + D^2}{2R} + \mathcal{O}\left(\frac{1}{R^2}\right) \,, \\ \delta &= \frac{D^2}{2R^2} + \mathcal{O}\left(\frac{1}{R^3}\right) \,, \\ \phi &= \frac{D}{R} + \frac{MD}{R^2} + \mathcal{O}\left(\frac{1}{R^3}\right) \,. \end{aligned} \tag{2.93}$$

We integrated Eqs. (2.88)-(2.91) taking the horizon areal radius R_H and the horizon electric charge $\tilde{Q}_{\rm AH}$ from the numerical evolution at $t = T$, and searching with a shooting procedure the values of $\phi(R_H)$ and $\delta(R_H)$ for which the asymptotic

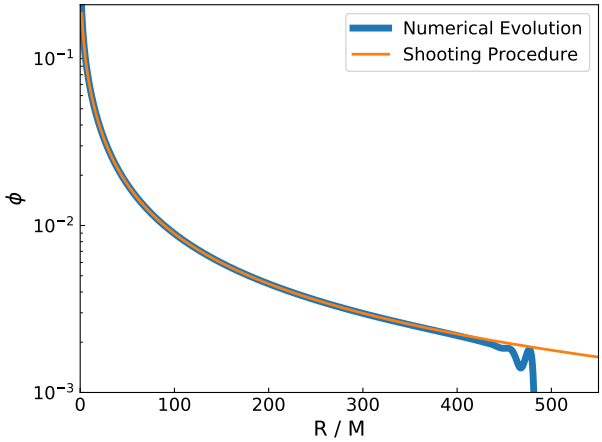

Figure 2.5. Profiles of the real scalar field obtained from the numerical integration at $T = 500M$ (blue) and from the shooting procedure extracting the parameters at $t = 100M$ (orange). The static scalarized solution is an excellent approximation of the end state of the evolution for $R < T$, as expected.

behaviors (2.93) were satisfied. We used the Newton's method as a root-finding algorithm. Since the scalarized solution is not unique, we initialized $\phi(R_H)$ using the end state of the evolution, in order to obtain the required profile of the real scalar field.

We then computed the scalar charge D as

$$D = -R^2 \frac{d\phi}{dR}\bigg|_{R=R_\infty}, \tag{2.94}$$

where R_∞ is the areal radius at the outer boundary, and the ADM mass as

$$M = m(R_\infty) + \frac{\tilde{Q}^2_{\rm AH} + D^2}{2R_\infty}. \tag{2.95}$$

In order to show the accuracy of this procedure, we performed a numerical integration of the field equations in the case of $\bar{Q}_i^{\rm BH} = 0.9$ until $t = T = 500M$, using a grid that extends up to $r_\infty = 550M$; we then compared the profile of the scalar field at the final time with the static scalarized solution computed extracting the parameters at $t = 100M$. The results are shown in Fig. 2.5, where we can see that the static solution accurately reproduces the end state of the numerical evolution, and the integration time $T = 100M$ is sufficient to obtain reliable estimates of the mass and electric charge of the final scalarized BH.

Once the mass had been extracted we could compute the charge-to-mass ratio of the final BH using the definition of the charge, Eq. (2.63).

One of our main results is shown in Fig. 2.6, where one can see that overcharged configurations are generically produced. Nonetheless, the end state of the collapse was always a (scalarized) BH and no naked singularities were produced in our gedanken experiments. This suggests that the cosmic censorship is not a prerogative of GR but is also at play in Einstein-Maxwell-scalar theory. I will further discuss this point in Sec. 2.4.3.

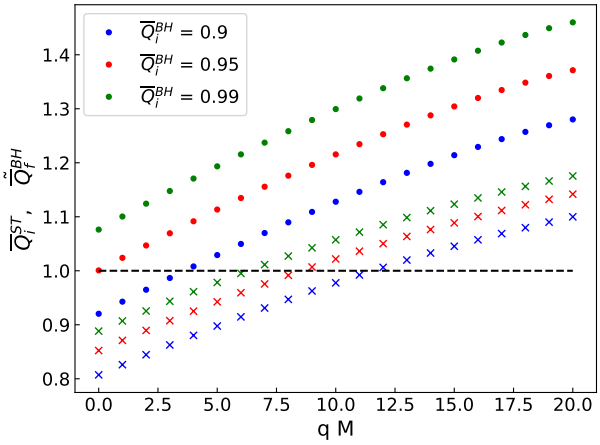

Figure 2.6. Charge-to-mass ratio $\tilde{\bar{Q}}_f^{\rm BH} = \frac{\tilde{Q}_f^{\rm BH}}{M_{\rm BH}}$ of the final BH (dots) and total charge-to-mass ratio $\bar{Q}_i^{\rm ST}$ of the spacetime at the beginning of the simulations (crosses) for the collapse in Einstein-Maxwell-scalar theory. This plot should be compared with the top panel of Fig. 2.4. In this case overcharged configurations were formed; this is due to the presence of the nonminimal coupling that quenches the electromagnetic interaction and allows to enclose a large amount of charge within the horizon.

For the static solution that we constructed the profile of the electric field is given by Eq. (2.67); in this expression the charge $\tilde{Q}$ accounts only for the contribution from the charged fields (see discussion in Sec. 2.3.3), and ϕ appears at the denominator via the coupling function, which is positive. Therefore the appearance of overcharged solutions may be explained by the action of the real scalar field that quenches the electric interaction, allowing to construct configurations in which a large amount of charged matter is confined within the horizon due to gravitational attraction. In this sense the electric charge $Q = \frac{\tilde{Q}}{F[\phi]}$ can be interpreted as a parameter that represents the "strength" of the electromagnetic interaction. In Fig. 2.7 I show the charge enclosed in the 2-spheres of areal radius R for a static scalarized configuration, using the two definitions (2.62) and (2.63); as we can see $\tilde{Q}$ is constant, while Q decreases near the horizon due to the presence of the real scalar field.

Finally, it is worth mentioning that for high values of $\bar{Q}_i^{\rm BH}$ overcharged final configurations are produced even when $q = 0$ and the field ξ does not carry any contribution to the BH charge. This happens because part the mass of the BH is ejected in a scalar spherical wave during the scalarization process.

Induced descalarization of hairy BHs by absorption of opposite-charged wave packets

Next, we studied the possibility of forming a RN BH from a previously scalarized configuration.

As we can see from Fig. 2.1 for low values of the BH charge-to-mass ratio the system does not admit scalarized configurations. Our objective was to dynamically produce a RN BH from a previously scalarized one. To do this we started from a RN BH and induced the spontaneous scalarization with a perturbation of the real

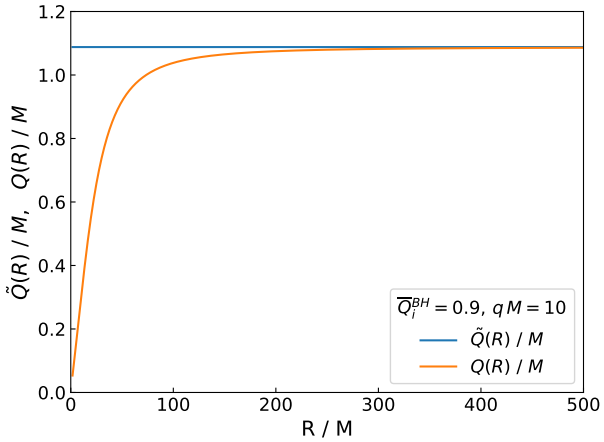

Figure 2.7. Charge enclosed in the 2-spheres of areal radius R for a static scalarized solution computed at the end of the numerical evolution. $\tilde{Q}$ accounts only for the contribution of the charged field, and is constant in R when the complex scalar ξ is absent. On the other hand Q can be seen as a parameter that measures the "strength" of the electromagnetic interaction, and it decreases near the horizon for a scalarized configuration.

scalar field; once the central BH reached a stable configuration, we sent a pulse of the complex scalar field with opposite charge in such a way that the final BH had charge close to zero and it was forced to descalarize.

We constructed the initial configuration using the same procedure described before, setting the BH mass to $M_i^{\rm BH} = M$ and the initial charge-to-mass ratio to $\bar{Q}_i^{\rm BH} = 0.5$. For the real scalar field we considered the profile in Eq. (2.86), while for the complex scalar field we exchanged the real and the imaginary parts in Eq. (2.69) (in order to have a wave packet with opposite charge) and we set the parameters to

$$\begin{aligned} &B_0 = 0.0004\,, \quad k_0 M = 5\,, \\ &\sigma_\xi^2 M^2 = 2.5\,, \quad r_{0,\xi}/M = 120\,. \end{aligned} \tag{2.96}$$

We also set $qM = 20$. In this way we obtained an inward-moving, negatively charged initial profile for ξ, such that the total charge of the spacetime was close to zero. The profile of the electric charge contained in the 2-spheres of radius r at $t = 0$ is shown in Fig. 2.8.

For the numerical evolution we chose a grid that extends up to $r_\infty = 400M$, with a grid step $\Delta r = 0.01M$. The CFL factor was CFL $= 0.5$ and the final integration time was $T = 240M$.

In Fig. 2.9 I show some snapshots[1] of the evolution of ϕ (in blue) and the real part of ξ (in red). As we can see in the first part of the evolution the BH is not affected by the complex scalar field and scalarizes reaching a stable configuration near in the central region. Later, the charged pulse reaches the horizon and is absorbed by the BH that, being in a region of the parameter space in which there is no stable scalarized solution, descalarizes leaving a final RN BH.

[1]Some animations of this gedanken experiment are available online [127].

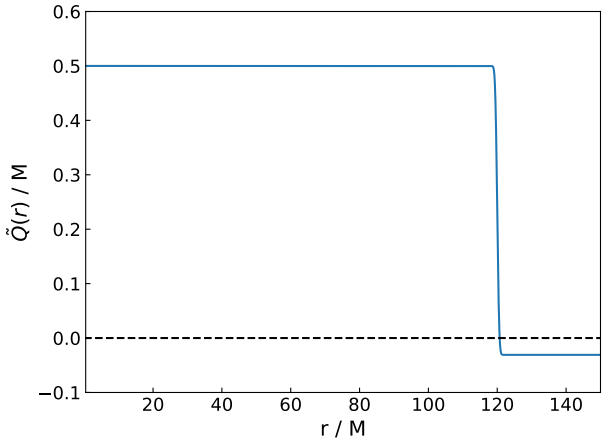

Figure 2.8. Profile of electric charge contained in the 2-spheres of radius r at $t = 0$. The charge carried by the complex scalar field was such that the total charge in the spacetime was close to zero. In this way when the pulse was absorbed by the BH, the system would be in a region of the parameter space in which no scalarized solutions exist.

To check that the BH at $t = 100M$ can be described by a scalarized solution, we compared the profile of the scalar field with the static scalarized configuration obtained using the shooting procedure described in the previous section. The result is shown in Fig. 2.10, where we can see that there is a good agreement between the two profiles. Thus we can assume that in the central region the scalarization process is completed, and that the subsequent part of the evolution shown in Fig. 2.9 (i.e., $t \gtrsim 100M$) can be considered a descalarization process.

Challenging the cosmic censorship II: superradiantly-induced descalarization

In this section I describe how we studied the possibility of overcharging a scalarized BH past its own extremality, showing that also in this case the superradiant extraction of the BH charge and mass plays a crucial role to bound the final charge-to-mass ratio below extremality.

In particular, we simulated the following process: we started with a RN BH and a small perturbation of the real scalar field so that the BH scalarized; once the scalarization process had completed in a region sufficiently large around the horizon, a pulse of the complex scalar field interacted with the BH, and set it to a new equilibrium state that we wanted to study.

In this case the horizon electric potential that appears in Eq. (2.85) should be computed by integrating Eq. (2.88), in which the coupling function appears at the denominator. Therefore in order to encounter the superradiant behavior for low values of q, we chose a small (negative) value of the coupling constant: $\lambda = -10$. This made the initial scalarization time scale longer than in the $\lambda = -500$ case previously explored, so we needed to throw the complex scalar field sufficiently later in order to make sure it interacted with the BH after the scalarization had

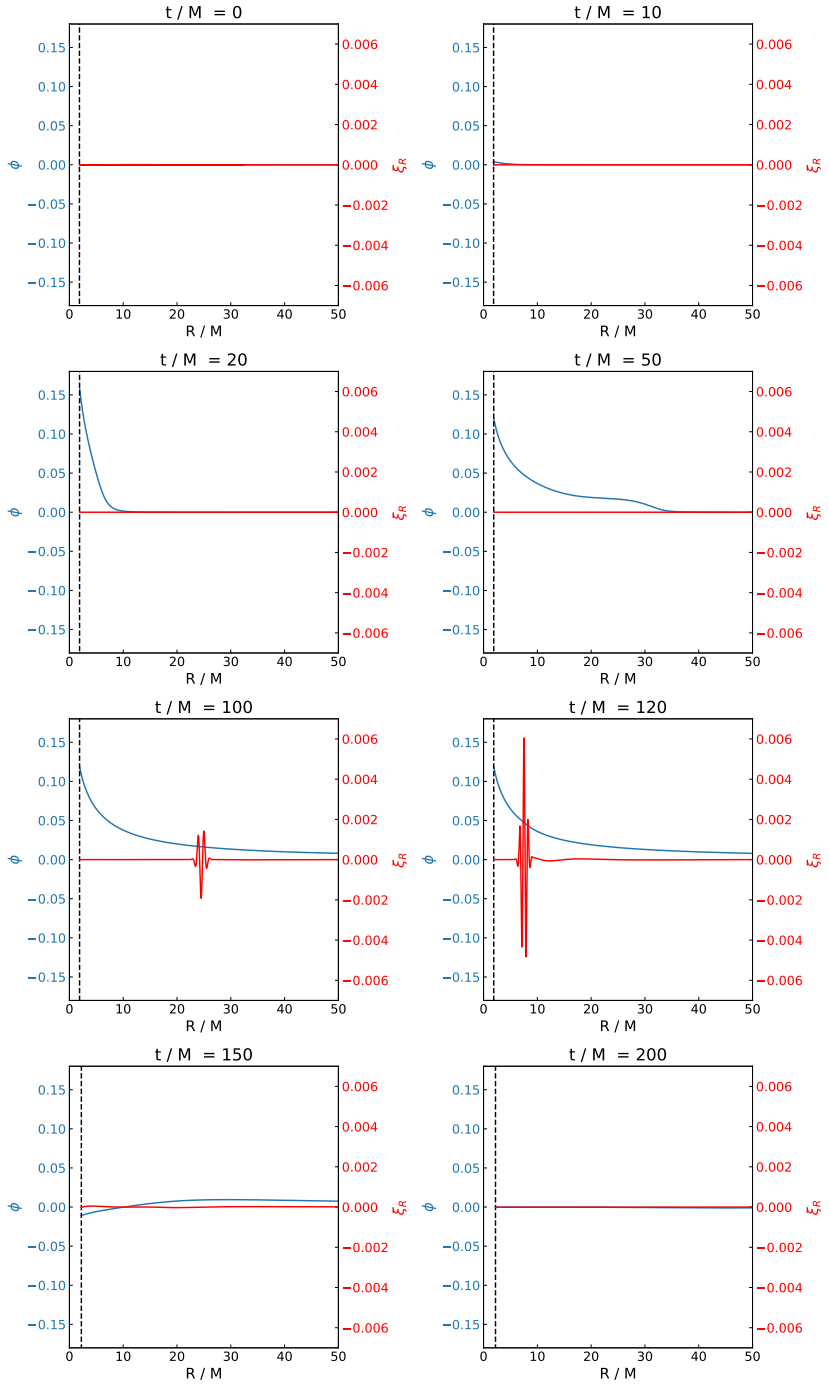

Figure 2.9. Snapshots of the evolution of the real scalar field ϕ (blue) and the real part of the complex scalar field ξ (red) for the process of scalarization and subsequent descalarization of a RN BH. The black dashed line shows the position of the apparent horizon. Initially the complex scalar field does not affect the dynamics of the system and the perturbation of the real scalar field triggers the spontaneous scalarization of the BH, that reaches a stable configuration. Then, when the complex scalar field reaches the horizon it is absorbed by the BH, which descalarizes leaving a final RN BH.

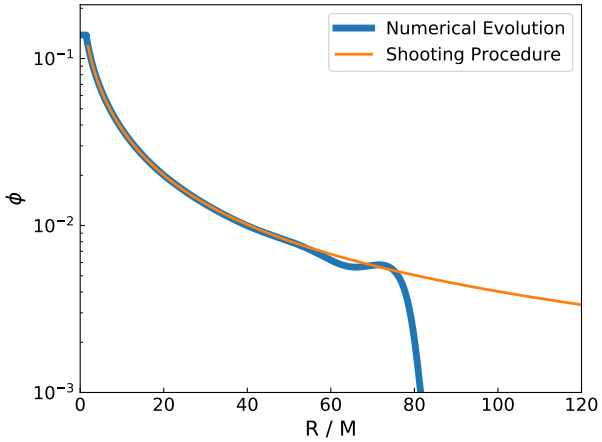

Figure 2.10. Comparison between the profile of the real scalar field at $T = 100M$ for the induced descalarization process (blue) and the static scalarized configuration obtained with the shooting procedure described in Sec. 2.4.3 (orange). As we can see there is a good agreement between the two profiles, and we can consider that in the central region the scalarization process is completed.

completed. We therefore placed the initial pulse of ξ far from the origin, setting the initial profile of ξ according to Eq. (2.69) with parameters

$$\begin{aligned} B_0 &= 0.0003\,, \quad k_0 M = 2\,, \\ \sigma_\xi^2 M^2 &= 0.5\,, \quad r_{0,\xi}/M = 150\,. \end{aligned} \tag{2.97}$$

This guaranteed that, when the pulse of the complex scalar field reached the BH, the scalarization process was completed in the horizon region. We also chose a smaller k_0 than in the previous case of standard Einstein-Maxwell theory in order for superradiance to occur at smaller values of q.

We implemented a nonuniform grid step in order to reduce the computational cost of the simulations. In particular the radial coordinate was transformed according to:

$$\begin{cases} \tilde{r} & = C(r) = \eta_2 r + \frac{1-\eta_1}{\Delta} \ln\left(\frac{1+e^{-\Delta(r-R_1)}}{1+e^{\Delta R_1}}\right) + \frac{\eta_2 - 1}{\Delta} \ln\left(\frac{1+e^{-\Delta(r-R_2)}}{1+e^{\Delta R_2}}\right) \\ \frac{\partial \tilde{r}}{\partial r} & = C'(r) = \eta_1 + \frac{1-\eta_1}{1+e^{-\Delta(r-R_1)}} + \frac{\eta_2 - 1}{1+e^{-\Delta(r-R_2)}} \end{cases} \tag{2.98}$$

where again is understood that r is the new coordinate and $\tilde{r}$ is the old one. We chose $\Delta = 1/M$, $\eta_1 = 0.1$, $\eta_2 = 10$, $R_1 = 10M$, and $R_2 = 200M$. The profile of the derivative $C'(r)$ is schematically depicted in Fig. 2.11; for low values of r this transformation is analogous to the one used for the collapse on flat background, while far from the origin large intervals in the coordinate $\tilde{r}$ are mapped into small intervals in r. In this way we could use a relatively large grid step without losing accuracy at the horizon, and we satisfied the condition that the signals did not reach the outer boundary even with a smaller numerical grid.

To construct the initial configuration we used the same shooting procedure as for the other simulations described in this section, imposing the following asymptotic

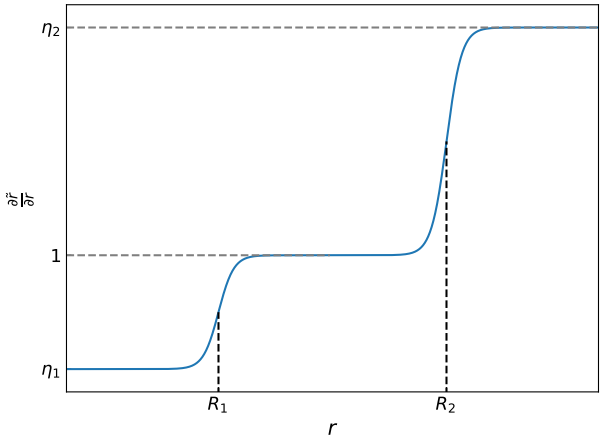

Figure 2.11. Schematic behavior of the derivative of the transformation $\tilde{r} = C(r)$ for the implementation of the nonuniform grid step. In the horizon region this transformation is analogous to the one used for the collapse on flat background, allowing larger grid steps without losing accuracy. Instead far from the origin large regions in the coordinate $\tilde{r}$ are mapped into small regions in r, allowing the use of a smaller numerical grid.

behaviors:

$$\begin{aligned} E^r &= \frac{Q_\infty}{\tilde{r}^2 \frac{\partial \tilde{r}}{\partial r}} + \mathcal{O}\Big(\frac{1}{\tilde{r}^3}\Big), \\ \psi := e^\chi &= 1 + \frac{M_{\rm ADM}}{2\tilde{r}} + \mathcal{O}\Big(\frac{1}{\tilde{r}^2}\Big), \\ K &= \mathcal{O}\Big(\frac{1}{\tilde{r}^3}\Big), \\ \varphi &= \frac{Q_\infty}{\tilde{r}} + \mathcal{O}\Big(\frac{1}{\tilde{r}^3}\Big), \end{aligned} \tag{2.99}$$

where again $M_{\rm ADM}$ is the ADM mass and $Q_\infty = Q(r_\infty)$.

The outer boundary was placed at $\frac{r_\infty}{M} = 250$, and the grid step was $\frac{\Delta r}{M} = 0.025$. The final time of integration was $\frac{T}{M} = 300$, and CFL $= 0.05$.

We computed the final BH mass using the static scalarized solution that approximates the configuration of the system in the central region, and we studied the behavior of the charge-to-mass ratio of the final BH; the results are shown in the upper panel of Fig. 2.12. As we can see the charge-to-mass ratio increases for small values of q, then reaches a peak and starts decreasing, as in the Einstein-Maxwell case. In the middle panel I show the mass difference between the final BH and the intermediate scalarized one. Interestingly, the mass of the final BH is smaller, showing that superradiance is at play also for the scalarized BH[2]. Indeed, also in this case the maximum of the charge-to-mass ratio roughly corresponds to the onset

[2]Note that a linear study of superradiant scattering off a scalarized BH in Einstein-Maxwell-scalar theory is much more involved than in the RN case in Einstein-Maxwell theory, since electromagnetic and scalar perturbations are coupled to each other. Hence, in this case we did not have a prediction for the threshold value of q.

of superradiance at nonlinear level. As for the collapse of the complex scalar field on a RN BH in Einstein-Maxwell theory, the extraction of charge is more efficient than the extraction of mass, so that $\tilde{Q}_f^{\rm BH}$ decreases. In other words, although the final charge-to-mass ratio can exceed the RN bound, it cannot grow indefinitely due to superradiance and reaches a maximum which is below the extremal value.

Interestingly enough, superradiance can be so efficient that the charge-to-mass ratio of the final BH can eventually cross the scalarization threshold (grey dashed line in the upper panel of Fig. 2.12), leading to a *superradiantly-induced descalarization*. This can be clearly seen from the behavior of the final scalar charge D (lower panel of Fig. 2.12): for large values of q the scalar charge goes to zero, indicating that the final BH has lost all its scalar hair. See [127] for some animations of these simulations.

Finally, in Fig. 2.13 I show the behavior of the difference between the final and the initial horizon areas. The area always increases, as expected from the area law, which holds also in our model since the null energy condition is satisfied.

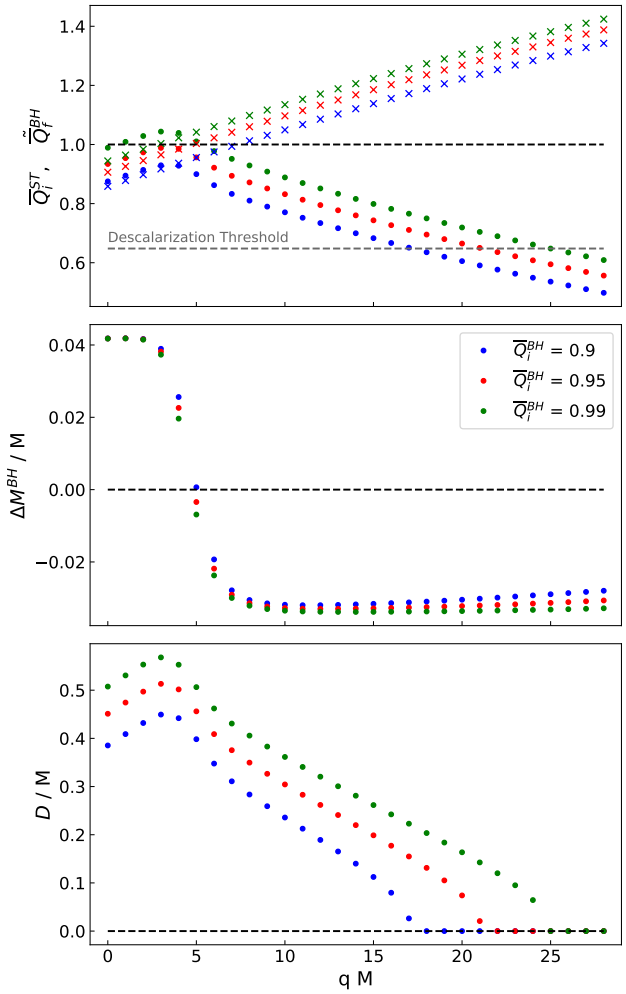

Figure 2.12. Results for the collapse of a complex scalar field in Einstein-Maxwell-scalar theory, with quadratic coupling and $\lambda = -10$. **Upper panel**: Charge-to-mass ratio $\tilde{\bar{Q}}_f^{\rm BH}$ of the final BH (dots) and total charge-to-mass ratio $\bar{Q}_i^{\rm ST}$ of the spacetime at the beginning of the simulations (crosses). **Middle panel**: mass difference between the final and the intermediate scalarized BH. **Lower panel**: scalar charge of the final BH. The charge-to-mass ratio of the final BH increases for low values of q, then it reaches a peak and starts decreasing. The negative $\Delta M^{\rm BH}$ for high values of q indicates the presence of superradiance. This mechanism can be efficient enough that the final charge-to-mass ratio falls below the threshold value for scalarization (grey dashed line in the upper panel), leading to the descalarization of the BH.

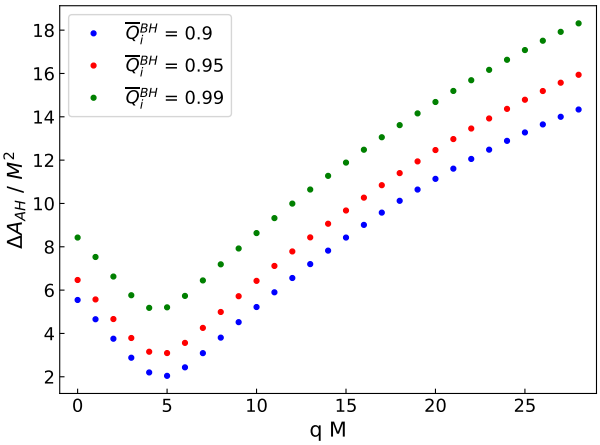

Figure 2.13. Difference between the final and initial BH area. As we can see the BH area always increases, in agreement with the area law.

Chapter 3

Fate of radiating BHs with minimum-mass in Einstein-dilaton-Gauss-Bonnet theory of gravity

In this chapter I will describe the work that I performed in collaboration with Marina de Amicis, Dr. Taishi Ikeda and Prof. Paolo Pani [43, 44], in which we performed numerically simulated gedanken experiments aimed at investigating the fate of evaporating minimum-mass BHs in EdGB gravity.

The structure of the chapter is the following. I will start in Sec. 3.1 by introducing EdGB gravity, its spherically symmetric BH configurations and the problem of Hawing evaporation. Moreover, I will discuss the phase space of static and spherically symmetric solutions, which includes wormholes and singular solitons, considering the possible phase transition that might occur in the process we investigated. Then, in Sec. 3.2 I will introduce the framework for our numerically simulated gedanken experiments, including the action, the field equations, and the metric ansatz that we used in our evolution code. Sec. 3.3 contains a description of the procedures we used to to construct the BH configurations in our setup, together with a discussion of some properties of such BH solutions that are relevant for our purposes, while our numerical evolution algorithm is introduced in Sec. 3.4. I will then describe the numerical simulations we performed and the results we obtained in Sec. 3.5.

3.1 Introduction to Einstein-dilaton-Gauss-Bonnet gravity

The action of EdGB gravity is [88] (in geometrized units $G = c = 1$)

$$S = \frac{1}{16\pi}\int_{\Omega} d^4x\,\sqrt{-g}\left\{\mathcal{R} - (\nabla_\mu\phi)(\nabla^\mu\phi) + 2F[\phi]\mathcal{G}\right\}, \tag{3.1}$$

where $\mathcal{R}$ is the scalar curvature, ϕ is the dilatonic field, $F[\phi]$ is the coupling function, and $\mathcal{G} = \frac{1}{4}\delta^{\mu\nu\alpha\beta}_{\rho\sigma\lambda\omega} R^{\rho\sigma}{}_{\mu\nu} R^{\lambda\omega}{}_{\alpha\beta}$ is the Gauss-Bonnet invariant, $\delta^{\mu\nu\alpha\beta}_{\rho\sigma\lambda\omega} = \epsilon^{\mu\nu\alpha\beta}\epsilon_{\rho\sigma\lambda\omega}$ is the generalized Kronecker delta, with $\epsilon_{\mu\nu\alpha\beta} = \epsilon^{\mu\nu\alpha\beta}$ being the Levi-Civita symbol.

As for the coupling function, we will consider an exponential form:

$$F[\phi] = \lambda e^{\gamma\phi}, \tag{3.2}$$

where λ is called Gauss-Bonnet coupling constant and γ is called dilaton coupling constant. While γ is dimensionless, $[\lambda] = [L^2]$, and sets the length scale below which modification start becoming relevant.

The field equations that can be obtained from the action read [1]

$$R_{\mu\nu} - \frac{1}{2} g_{\mu\nu} R = 8\pi T_{\mu\nu}, \tag{3.3}$$

$$\Box\phi = -\frac{\delta F[\phi]}{\delta\phi}\mathcal{G}, \tag{3.4}$$

where $\Box = \nabla_\mu \nabla^\mu$ and

$$T_{\mu\nu} = \frac{1}{8\pi}\left[(\nabla_\mu\phi)(\nabla_\nu\phi) - \frac{1}{2}(\nabla_\alpha\phi)(\nabla^\alpha\phi) g_{\mu\nu} - 2(\nabla_\gamma\nabla^\alpha F[\phi])\delta^{\gamma\delta\kappa\lambda}_{\alpha\beta\rho\sigma} R^{\rho\sigma}{}_{\kappa\lambda}\delta^{\beta}{}_{(\mu} g_{\nu)\delta}\right]. \tag{3.5}$$

Crucially, the field equations are of second order, making the theory of Horndeski type [130,131]. This guarantees that EdGB is free from the *Ostrogradsky instability* [132], a ghost-like instability potentially occurring when the fields equations are of order higher than two.

In 4 dimensions, the presence of the nonminimal coupling between the dilatonic field and the Gauss-Bonnet invariant is crucial to introduce modifications to GR. Indeed if $F[\phi] = 1$ then the Gauss-Bonnet term is topological, and the theory reduces to GR with a Klein-Gordon field in the matter sector. This can be also clearly seen from the fact that in this case the right hand side of Eq. (3.4) vanishes, and $T_{\mu\nu}$ reduces to the stress-energy tensor of a minimally coupled scalar field.

3.1.1 Black hole solutions

For theories whose action can be described by Eq. 3.1, the field equations can in principle admit GR BHs as solutions, provided that the dilaton field assumes a constant value ϕ_0 such that

$$\left.\frac{\delta F[\phi]}{\delta\phi}\right|_{\phi=\phi_0} = 0. \tag{3.6}$$

This is not possible for a coupling of the form (3.2), meaning that EdGB BHs are always characterized by a nontrivial profile of the dilaton field outside them [2].

[1] A derivation of the field equations can be found in Appendix A of [128], but see also Appendix A of [129] for a more detailed computation.

[2] For couplings of the form $F[\phi] = \frac{\lambda}{24}(1 - e^{-3\phi^2})$ [77, 133–135] or $F[\phi] = \frac{1}{16}\lambda\phi^2$ [78, 136–140] also the Kerr-Newmann BH is a solution of the field equations, and the BH configurations with a nontrivial profile of the scalar field are called *scalarized*. Theories with these coupling are usually referred to as *Einstein-scalar-Gauss-Bonnet* gravities, and exhibit a spontaneous scalarization phenomenon similar to the one discussed in Sec. 2.2 : in certain regions of the parameter space Kerr-Newman BHs are subject to a tachyonic instability whose end state is a scalarized configuration (see Ref. [79] for a review).

In order to study their main properties, let us now construct these static *dilatonic* BH configurations, restricting to the spherically-symmetric case for simplicity. While this has been first done in Ref. [88], I will follow Ref. [44] highlighting only the main steps. More explicit derivations can also be found in Refs. [141, 142].

Let us use Schwarzschild-like coordinates, so that the line element can be written as:

$$ds^2 = -e^{\Gamma(\mathfrak{r})}d\mathfrak{t}^2 + e^{\Lambda(\mathfrak{r})}d\mathfrak{r}^2 + \mathfrak{r}^2 d\Omega^2\,, \tag{3.7}$$

where $\Gamma(\mathfrak{r})$ and $\Lambda(\mathfrak{r})$ are functions of the areal radius $\mathfrak{r}$. Substituting this expression in the field equations (3.3),(3.4) we can obtain a set of 4 ordinary differential equations for Γ, Λ and ϕ, whose explicit expression can be found in Appendix C. After some manipulations one obtains an analytic expression for Λ in terms of Γ and ϕ, and two second-order equations for Γ and ϕ. Since we are in Schwarzschild coordinates, $g_{\mathfrak{t}\mathfrak{t}} = -e^{\Gamma}(r)$ is defined up to a multiplicative constant (expressing the residual freedom in rescaling the coordinate time), and Γ appears in the equations only through its radial derivatives.

At the horizon $g_{\mathfrak{t}\mathfrak{t}}$ vanishes and $g_{\mathfrak{r}\mathfrak{r}}$ diverges, so that the metric functions and the dilatonic field can be expanded as

$$\begin{cases} e^{\Gamma(\mathfrak{r})} & = \Gamma_1(\mathfrak{r}-\mathfrak{r}_H) + \mathcal{O}\left[(\mathfrak{r}-\mathfrak{r}_H)^2\right] \\ e^{-\Lambda(\mathfrak{r})} & = \lambda_1(\mathfrak{r}-\mathfrak{r}_H) + \mathcal{O}\left[(\mathfrak{r}-\mathfrak{r}_H)^2\right] \\ \phi(\mathfrak{r}) & = \phi_H + \phi'_H(\mathfrak{r}-\mathfrak{r}_{\rm H}) + \mathcal{O}\left[(\mathfrak{r}-\mathfrak{r}_{\rm H})^2\right] \end{cases}, \tag{3.8}$$

where Γ_1, λ_1, ϕ_H and ϕ'_H are real coefficients.

From the second-order equation for ϕ it is possible to see that ϕ'' contains terms that diverge at the horizon, and in order to remove them ϕ'_H must be set to

$$\phi'_H = -\frac{\mathfrak{r}_{\rm H}}{8F'[\phi_H]}\left(1 - \sqrt{1 - \frac{192}{\mathfrak{r}_{\rm H}^4}F'[\phi_H]^2}\right), \tag{3.9}$$

where $F'[\phi] = \frac{\delta F[\phi]}{\delta\phi}$.

Γ_1 is the multiplicative factor expressing the residual gauge freedom in the definition of the coordinate time, while λ_1 can be obtained by substituting the expansion at the horizon in the analytic expression for Λ. The result is

$$\lambda_1 = \frac{1}{\mathfrak{r}_{\rm H} + 4F'[\phi_H]\phi'_H}. \tag{3.10}$$

Therefore we have that for a given coupling function, and fixing the horizon areal radius $\mathfrak{r}_H$, the near-horizon solution depends only on the parameter ϕ_H.

Near spatial infinity, instead,

$$e^{\Gamma(\mathfrak{r})} \simeq e^{-\Lambda(\mathfrak{r})} \simeq 1 - \frac{2M_{\rm BH}}{\mathfrak{r}} + \mathcal{O}\left(\mathfrak{r}^{-2}\right) \tag{3.11}$$

$$\phi(\mathfrak{r}) \simeq -\frac{D}{\mathfrak{r}} + \mathcal{O}\left(\mathfrak{r}^{-2}\right), \tag{3.12}$$

where $M_{\rm BH}$ is the BH mass and D is the dilaton charge.

The static dilatonic solutions can be obtained by fixing the parameter ϕ_H in such a way that the asymptotic behavior (3.12) is satisfied. Once done this Γ_1 can

be fixed by imposing (3.11), *i.e.* that asymptotically coordinate time coincides with proper time.

Unfortunately this procedure cannot be carried out at the analytical level, but numerical methods have to be used. Here I will directly move to describe the characteristic of dilatonic BH configurations, and a discussion on the numerical procedures used for this kind of computations is postponed to Sec. 3.3.2.

For concreteness, I will focus on the case with $\gamma = 4$; different values of the dilaton coupling constant are discussed later, including $\gamma = \sqrt{2}$, which is motivated by string theory [89] and shares the same qualitative features that are relevant for our purposes. In Fig. 3.1 I show the areal radius of the event horizon as a function of the BH mass $M_{\rm BH}$ in this theory. When $\lambda/\mathfrak{r}_H^2 \ll 1$, there exists only one asymptotically-flat solution for given BH mass, which reduces to the GR Schwarzschild BH in the $\lambda \to 0$ limit. In this limit one gets $\mathfrak{r}_H \approx 2M_{\rm BH}$ as in GR. However, for any finite λ there exists a minimum-mass[3] BH solution [88, 91–93], $M_{\rm BH} \geq M_{\rm crit} \simeq 8.244\sqrt{\lambda}$. This is called *critical* solution, and divides two branches of solutions with the same mass and different radii. The upper branch (i.e., larger radii) is linearly stable, whereas the lower branch (i.e., smaller radii) is linearly unstable [95, 143]. As later discussed, the details (and existence) of the second branch depend on the specific values of γ. In our context it is important to highlight that, just as the Schwarzschild solution, these metrics have a curvature singularity inside the horizon [91], except for the solution at the end of the unstable branch in which such singularity coincides with the horizon and becomes naked (see, e.g., [142, 144] for BHs in shift-symmetric theories with $F[\phi] \propto \phi$). Since for $\gamma \gtrsim 1$ this singular solution does not coincide with the minimum-mass solution, the latter is regular on and outside the horizon, just as in the GR case. On the other hand, the singular solution is unphysical as it is part of the unstable branch.

3.1.2 Hawking evaporation

An interesting aspect that arises when quantizing a field in curved spacetime is that there is not a unique way of performing a mode decomposition which is valid for all the observers. Two observers may decompose a field using two different sets of modes, having two distinct notions of vacuum. Therefore a state identified as vacuum for an observer, might be seen as containing particles by another observer [145]. This happens also in collapsing scenarios and it is at the root of the Hawking effect [94].

Let us consider a system that is undergoing gravitational collapse to a BH and two asymptotic observers, one placed "in the past" and one "in the future". The modes from the first observer will experiment a gravitational blueshift when getting close to the collapsing body, and a redshift when departing from it in the future direction. Now, in the spacetime position where the modes exit from the body the collapse is in a more advanced state with respect to the entrance, thus the redshift will be more intense than the blueshift, with a net effect that is more relevant for the modes that pass close to horizon formation. As a consequence, the modes of the observer "in the past" will appear distorted to the observer "in the future", and

[3] As later discussed, other values of $\gamma \gtrsim 1$ change the proportionality factor of the minimum mass but in general $M_{\rm crit} \propto \sqrt{\lambda}$.

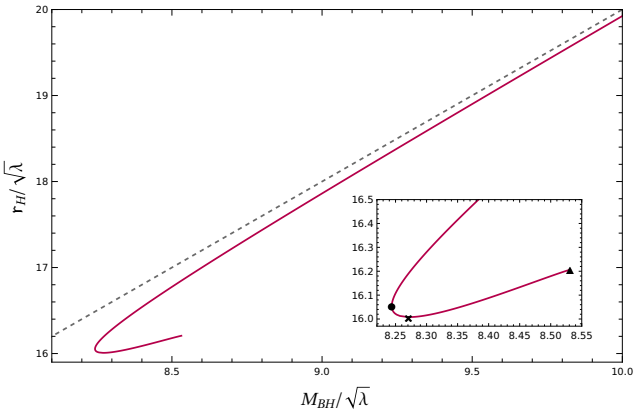

Figure 3.1. Areal radius of the event horizon as a function of the BH mass for static BH solutions in EdGB gravity with coupling $F[\phi] = \lambda e^{-4\phi}$. The gray dashed line is the Schwarzschild limit $\mathfrak{r}_H = 2M_{\rm BH}$, reached when $M \gg M_{\rm crit} \approx 8.244\sqrt{\lambda}$. The inset is a zoom-in around the minimum-mass solution, which separates a stable branch from an unstable branch. The minimum-mass, minimum-radius, and singular BH solutions are denoted by a circle, cross, and triangle, respectively.

the vacuum state of the observer "in the past" will be seen as containing particles by the observer "in the future". In particular the particles detected by this second observer come from the BH and assume a thermal spectrum with temperature [145]

$$T_H = \frac{\kappa}{2\pi}, \tag{3.13}$$

where κ is the surface gravity. T_H is called Hawking temperature, and the effect is called Hawking radiation [94]. The result is that BHs radiate away energy and lose mass at a rate given by the luminosity of radiation, which is given by [145]

$$\frac{dM}{d\mathfrak{t}} = -\frac{1}{2\pi}\sum_{lm}\int d\omega \frac{\omega G_{lm}(\omega)}{e^{\omega/T_{\rm BH}} \pm 1}\,, \tag{3.14}$$

where the sum is over the (l, m) angular mode of the radiation and, at the denominator, the plus/minus applies to the emission of fermions/bosons. $G_{lm}(\omega)$ is called graybody factor, and accounts for the fact that not all modes are able to penetrate the effective potential barrier.

For a spacetime of the form (3.7) the Hawking temperature can be expressed as

$$T_{\rm BH} = \frac{1}{4\pi}\lim_{\mathfrak{r}\to\mathfrak{r}_H}\frac{dg_{\mathfrak{tt}}/d\mathfrak{r}}{\sqrt{g_{\mathfrak{tt}}g_{\mathfrak{rr}}}}\,, \tag{3.15}$$

which, for a Schwarzschild BH, evaluates to $\frac{1}{8\pi M}$. For EdGB black holes instead we evaluated it numerically, obtaining the results shown in Fig. 3.2, where we can see that it is always higher that that of the corresponding Schwarzschild BH with the same mass. Furthermore, the temperature is nonvanishing also for the minimum-mass solution, suggesting that the BH continues emitting energy once it reaches the minimum-mass configuration.

However, in order to assess if this is the case it is necessary to compute the graybody factor relative to the emitted modes. In our work [43, 44] we computed

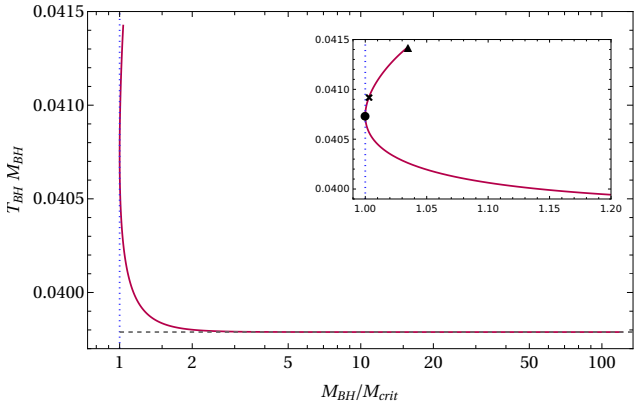

Figure 3.2. Hawking temperature of a dilatonic BH in EdGB gravity as a function of the BH mass. The horizontal dashed line denotes the temperature of a Schwarzschild BH, $T_{\rm BH}^{\rm GR} = 1/(8\pi M_{\rm BH}) \approx 0.0398/M_{\rm BH}$. The inset is a zoom-in around the minimum-mass solution. The minimum-mass, minimum-radius, and singular BH solutions are denoted by a circle, cross, and triangle, respectively.

this quantity for minimally-coupled scalar massless particles and for photons[4] (see also [146]). In particular, we considered the lowest angular modes, i.e. $l = 0$ and $l = 1$, for the scalar and vector emission, respectively, which give the leading contribution to the mass loss in this case.

The scalar Ψ and electromagnetic A_μ fields satisfy the following field equations:

$$\begin{aligned} &\nabla_\mu \partial^\mu \Psi = 0\,, \\ &\nabla_\mu (\partial^\mu A^\nu - \partial^\nu A^\mu) = 0\,, \end{aligned} \tag{3.16}$$

on the background metric described by the dilatonic BH solution. Since the background metric (3.7) is spherically symmetric, it is possible to decompose the scalar field in spherical harmonics $Y_{lm}(\theta,\varphi)$ and the electromagnetic field in vector harmonics [147]:

$$\begin{aligned} \Psi(\mathfrak{t},\mathfrak{r},\theta,\varphi) &= \sum_{lm} \frac{R_{lm}(\mathfrak{t},\mathfrak{r})}{\mathfrak{r}} Y_{lm}\,, \\ A_\mu(\mathfrak{t},\mathfrak{r},\theta,\varphi) &= \sum_{lm} \begin{pmatrix} f_{lm}(\mathfrak{t},\mathfrak{r}) \\ h_{lm}(\mathfrak{t},\mathfrak{r}) \\ a_{lm}(\mathfrak{t},\mathfrak{r}) \frac{1}{\sin\theta}\partial_\varphi + k_{lm}(\mathfrak{t},\mathfrak{r})\partial_\theta \\ a_{lm}(\mathfrak{t},\mathfrak{r}) \sin\theta \partial_\theta - k_{lm}(\mathfrak{t},\mathfrak{r})\partial_\varphi \end{pmatrix} Y_{lm}\,. \end{aligned}$$

Substituting these expansions in the field equations (3.16) and assuming a time dependence $e^{-i\omega\mathfrak{t}}$, the radial part of the equations separates and takes the form of a Schrödinger-like equation:

$$\frac{d^2}{d\mathfrak{r}_*^2}\Theta_{lm}(\mathfrak{r}) + \left[\omega^2 - V_{slm}(\mathfrak{r})\right]\Theta_{lm}(\mathfrak{r}) = 0\,, \tag{3.17}$$

[4]Of course also gravitons would be radiated, and in EdGB theory the gravitational sector is coupled to the dilaton. The computation of the graybody factor for gravitons and dilatons is technically more involved but does not change the qualitative picture.

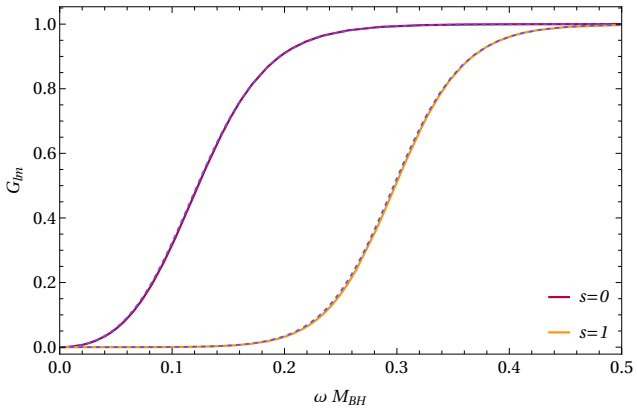

Figure 3.3. Graybody factors of the dilatonic BH with minimum mass ($\lambda \approx 0.01552$ in units such that $\mathfrak{r}_h = 2$, as we shall fix from now on), for the emission of massless scalar particles (purple) and photons (orange) in their lowest angular modes ($l = 0, 1$, respectively). We compare each curve with the corresponding graybody factors of a Schwarzschild BH with same mass (dashed blue lines).

where Θ_{lm} collectively denotes the master function for the scalar or the electromagnetic field, and

$$\begin{aligned} V_{s=0}(\mathfrak{r}) &= \frac{l(l+1)}{\mathfrak{r}^2} e^{\Gamma(\mathfrak{r})} + e^{\frac{\Gamma(r)-\Lambda(\mathfrak{r})}{2}} \frac{1}{\mathfrak{r}} \frac{d}{d\mathfrak{r}} e^{\frac{\Gamma(\mathfrak{r})-\Lambda(\mathfrak{r})}{2}} , \\ V_{s=1}(\mathfrak{r}) &= \frac{l(l+1)}{\mathfrak{r}^2} e^{\Gamma(\mathfrak{r})} , \end{aligned} \tag{3.18}$$

for the scalar ($s = 0$) and electromagnetic ($s = 1$) cases, respectively. In the above equations, $\mathfrak{r}_*$ is the generalized tortoise coordinate defined through

$$\frac{d\mathfrak{r}_*}{d\mathfrak{r}} = e^{\frac{\Lambda(\mathfrak{r})-\Gamma(\mathfrak{r})}{2}} . \tag{3.19}$$

The potentials in Eq. (3.18) vanish both at the horizon and at spatial infinity and their radial profile is in fact qualitatively very similar to the case of a Schwarzschild BH. The asymptotic solutions are ingoing/outgoing waves in tortoise coordinates, $\Theta_{lm} \sim e^{\pm i\omega \mathfrak{r}_*}$. Normalizing the flux coming from infinity, the graybody factor is simply related to the transmission coefficient of the master function,

$$\begin{cases} \Theta_{lm} = e^{-i\omega\mathfrak{r}_*} + \mathcal{R}_{lm} e^{i\omega\mathfrak{r}_*} & \mathfrak{r}_* \to \infty \\ \Theta_{lm} = G_{lm} e^{-i\omega\mathfrak{r}_*} & \mathfrak{r}_* \to -\infty \end{cases} . \tag{3.20}$$

We studied this scattering problem for the lowest angular modes of the massless scalar and the electromagnetic field, for different values of the coupling constant λ. In Fig. 3.3, I show the graybody factors of the dilatonic BH with minimum mass, compared with those of a Schwarzschild BH of equal mass. Overall these two quantities are very similar to each other for any value of the coupling (of course the agreement further improves for smaller values of the coupling than that shown in Fig. 3.3). This is consistent with the fact that the graybody factor is mainly governed by the BH photon-sphere, which is slightly outside the horizon, where the

higher-curvature corrections are already smaller relative to their value at and inside the horizon.

Therefore, the main difference between the spectrum of a dilatonic and a Schwarzschild BH comes from the (slightly) different temperature. Since the temperature of a dilatonic BH is (slightly) higher than that of a Schwarzschild BH of the same mass, the former evaporates (slightly) faster than the latter. Using Eq. (3.14), we estimated that near the minimum mass a dilatonic BH evaporates $\approx 7\%$ and $\approx 14\%$ faster than in GR for scalar and vector modes, respectively.

Intriguingly, when the dilatonic BH reaches the minimum-mass configuration, the graybody factor and temperature are finite and nonvanishing. In other words, the BH should continue evaporating, but since there are no static BH solutions with lower mass, it is natural to ask toward which state the BH evolves.

3.1.3 Phase diagram

To start addressing the question related to the evolution of BHs past the minimum mass in EdGB gravity, it is useful to study in detail the parameter space of static and spherically-symmetric solutions in this theory. In particular, one might entertain the idea of phase transitions from the critical BH toward some other solutions, should the parameter space allow for that. Interestingly, EdGB gravity admits other, horizonless, asymptotically flat solutions: traversable wormholes [148, 149] and particle-like (solitonic) solutions characterized by a singularity in the second derivative of the dilaton field [150, 151]. In our work we have built these solutions following Refs. [148–151]. Details are presented in Appendix D.

Fig. 3.4 contains the phase diagram $(D/M, \lambda/M^2)$, first computed in Ref. [150, 151]. BHs and solitons form a one-parameter family of solutions, so they are represented by curves which encloses a two-dimensional surface. The latter is the domain of existence of the wormhole solutions. An interesting feature of this phase diagram is that the BH solutions (including the minimum mass) correspond to *double points* in the phase space, wherein the BH and the wormhole solution co-exist (see inset in Fig. 3.4). Furthermore, the singular BH solution at the end of the unstable branch connects also to the solitonic solution which has a derivative singularity (i.e., a cusp), being therefore a *triple point* in the phase space of the theory. Thus, even though the solitonic solution is probably not a good candidate for the endpoint of a phase transition, the regular wormhole solution is more appealing.

3.2 Inducing mass loss with a phantom field: framework

To investigate the fate of a critical BH that undergoes Hawking evaporation, in the work of Refs. [43, 44] we decided to construct a numerically simulated gedanken experiment in which we push the BH mass below the minimum value, and then observe how the system evolves. The main conceptual difficulty here was to devise a method to dynamically reduce the BH mass in a controlled way. Our strategy was to simulate the collapse of wave packets of a phantom field, *i.e.* a real scalar field whose kinetic term has the opposite sign with respect to our conventions. Such

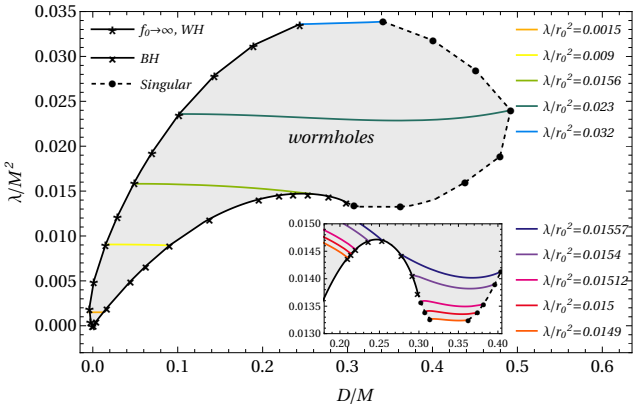

Figure 3.4. Families of asymptotically flat solutions to EdGB gravity as plotted in the phase space $(D/M, \lambda/M^2)$, where D is the dilatonic charge and M is the mass of the object measured by an observer at spatial infinity (see also [148–151]). The gray region represents the domain of existence of the wormhole solutions, each colored line represents a family of wormhole solutions characterized by a specific value of λ (in units where the wormhole throat is $r_0 = 2$): $\lambda = 0.0015$ (orange), $\lambda = 0.009$ (yellow), $\lambda = 0.0156$ (green), $\lambda = 0.023$ (dark green) and $\lambda = 0.032$ (light blue). The upper black line (asterisks) corresponds to regular wormhole solutions in the $f_0 \to \infty$ limit (see Appendix D). The lower black line (crosses) corresponds to BH solutions, whereas the dashed line (dots) corresponds to solitonic solutions with a singularity in the second derivative of the dilaton.

a field contributes with negative terms to the total mass of the system, and when absorbed by a black hole, leads to a decrease of its mass.

With this approach in mind, we constructed the setup for our numerically simulated gedanken experiment, which I will now start describing.

The action of the model we considered is obtained by supplementing Eq. (3.1) with a phantom field:

$$S = \frac{1}{16\pi}\int_\Omega d^4x\,\sqrt{-g}\left\{\mathcal{R} - (\nabla_\mu\phi)(\nabla^\mu\phi) + (\nabla_\mu\xi)(\nabla^\mu\xi) + 2F[\phi]\mathcal{G}\right\}, \tag{3.21}$$

where ξ is the phantom field, and the other symbols preserve the same meaning as in Eq. (3.1).

The fields equations derived from the new action read

$$R_{\mu\nu} - \frac{1}{2}g_{\mu\nu}R = 8\pi T_{\mu\nu}, \tag{3.22}$$

$$\Box\phi = -\frac{\delta F[\phi]}{\delta\phi}\mathcal{G}, \tag{3.23}$$

$$\Box\xi = 0, \tag{3.24}$$

where

$$T_{\mu\nu} = \frac{1}{8\pi}\Big[(\nabla_\mu\phi)(\nabla_\nu\phi) - \frac{1}{2}(\nabla_\alpha\phi)(\nabla^\alpha\phi)g_{\mu\nu} - (\nabla_\mu\xi)(\nabla_\nu\xi) + \frac{1}{2}(\nabla_\alpha\xi)(\nabla^\alpha\xi)g_{\mu\nu}$$
$$- 2(\nabla_\gamma\nabla^\alpha F[\phi])\delta^{\gamma\delta\kappa\lambda}_{\alpha\beta\rho\sigma}R^{\rho\sigma}{}_{\kappa\lambda}\delta^\beta{}_{(\mu}g_{\nu)\delta}\Big] \tag{3.25}$$

is the effective stress-energy tensor.

In the case $\xi = 0$ the field equations reduce to (3.3)-(3.4), and allow to study the stability of dilatonic BHs in EdGB by simulating the collapse of wave packets of the dilaton ϕ. While the main focus of our work was to study the fate of evaporating BHs past the minimum mass, we decided to carry out such additional set of simulations, which, from the numerical point of view, differ from the case of collapse of the phantom field only in the initial condition.

We used Painlevé-Gullstrand (PG)-like coordinates, which are horizon penetrating and read

$$ds^2 = -\alpha(t,R)^2 dt^2 + (dR + \alpha(t,R)\zeta(t,R)\, dt)^2 + R^2 d\Omega^2, \tag{3.26}$$

where R is the areal radius. Since we were interested in simulating the BH evolution close to the critical configuration, for which the curvature singularity is close to the horizon, we also needed small grid steps to resolve properly the BH region. In order to reduce the computational cost by increasing the resolution only in the central region, we defined a new radial coordinate r related to the areal radius R by the relation

$$\begin{cases} R &= \eta_2 r + \frac{1-\eta_1}{\Delta}\ln\left(\frac{1+e^{-\Delta(r-r_1)}}{1+e^{\Delta r_1}}\right) + \frac{\eta_2-1}{\Delta}\ln\left(\frac{1+e^{-\Delta(r-r_2)}}{1+e^{\Delta r_2}}\right) \\ \frac{\partial R}{\partial r} &= \eta_1 + \frac{1-\eta_1}{1+e^{-\Delta(r-r_1)}} + \frac{\eta_2-1}{1+e^{-\Delta(r-r_2)}} \end{cases}. \tag{3.27}$$

The strategy is analogous to the one used in the previous chapter, and in fact (3.27) coincides with the transformation (2.98). In this way, since in the inner region $R' \sim \eta_1 < 1$, and in the outer region $R' \sim \eta_2 > 1$ (cf. Fig. 2.11), discretizing the radial coordinate r with a uniform grid step, we obtained a higher resolution in R in the inner region and a lower resolution in the outer region.

In this new coordinates the line element reads

$$ds^2 = -\alpha(t,r)^2 dt^2 + (R'(r)dr + \alpha(t,r)\zeta(t,r)\, dt)^2 + R(r)^2 d\Omega^2. \tag{3.28}$$

An important ingredient for our simulations is the construction of the static dilatonic BH configurations, that are needed both for initializing the code and for analyzing the final state of the evolution. Therefore in the next section I will describe the procedures we used to obtain them, re-expressing the relations of Sec. 3.1.1 in PG-like coordinates and describing the numerical techniques. I will also include a discussion on the properties of BH solutions for different values of the dilaton coupling constant appearing in $F[\phi]$ (Eq. (3.2)), motivating our choice of setting $\gamma = 4$ in our analysis.

3.3 Static solutions in horizon-penetrating coordinates

Since here we need to consider static solutions in EdGB, for this section I will refer again to the action (3.1), and consider profiles of α, ζ and ϕ that depend solely on the radial coordinate r.

3.3.1 Equations and boundary conditions

Replacing the line element (3.28) into the field equations (3.3)-(3.4) and performing algebraic operations, we can obtain two first-order equations for α and ζ, and a second-order equation for ϕ, which are reported in Appendix C.

The expansion of the future-directed outgoing null geodesics normal to the 2-spheres S_R of (areal) radius R is given by

$$\theta_{(l)} = \frac{2}{R}(1-\zeta), \tag{3.29}$$

where $l^\mu = (\frac{1}{\alpha}, \frac{1-\zeta}{R'}, 0, 0)$ is the future-directed null vector normal to S_R. Thus, the horizon r_h is located where $\zeta = 1$.

The denominator of the right-hand side of the equation for the dilaton (Eq. (C.8)) goes to zero at the horizon, and imposing that the singular terms in $\phi_h'' := \phi''(r_h)$ vanish, we recover the regularity condition [88]:

$$\phi_h' = \frac{R_h' \left(-R_h^2 + \sqrt{R_h^4 - 192F'[\phi_h]^2}\right)}{8R_h F'[\phi_h]}, \tag{3.30}$$

where the subscript h indicates that the quantities are evaluated at the horizon, and $F'[\phi] = \frac{\delta F[\phi]}{\delta \phi}$. This expression is the analog of Eq. (3.9) in different coordinates.

In PG-like coordinates the spatial 3-metric is flat, and thus the ADM mass identically vanishes. Following [152], we used the asymptotic value of the Misner-Sharp mass function $m_{\rm MS}(r)$ as a definition of the total mass of the spacetime:

$$M_{\rm MS} := \lim_{r\to+\infty} m_{\rm MS}(r) = \lim_{r\to+\infty} \frac{R}{2}\zeta^2. \tag{3.31}$$

The asymptotic behaviors of ϕ, α and ζ in the asymptotically flat case can then be written as

$$\phi = -\frac{D}{R} + \mathcal{O}\Big(\frac{1}{R^2}\Big), \tag{3.32}$$

$$\zeta = \sqrt{2\frac{M_{\rm MS}}{R}} + \mathcal{O}\Big(\frac{1}{R^{5/2}}\Big), \tag{3.33}$$

$$\alpha = A + \mathcal{O}\Big(\frac{1}{R^2}\Big), \tag{3.34}$$

where the constant A in Eq. (3.34) is a free parameter, since α can be arbitrarily rescaled by a constant with a redefinition of the coordinate time.

3.3.2 Numerical procedures

We used two procedures for constructing the static dilatonic BH solutions.

The first is a standard shooting, wherein (for fixed values of the coupling constant λ and the horizon radius R_h) we integrated the equations from the horizon outward, using Newton's method to find the value of the only free parameter ϕ_h for which the asymptotic boundary conditions (3.32)-(3.34) are satisfied. We finally obtained the static dilatonic solution by performing an integration both outside and

inside the BH region. Note that since the equations for ϕ and ζ do not depend on α, we did not integrate the equation for this metric function.

The second procedure is based on the invariance of the theory under the transformation

$$\phi \to \phi + C \qquad \lambda \to \lambda e^{\gamma C}, \tag{3.35}$$

where C is a real constant. The strategy is similar to the one outlined in Ref. [153]. Namely, we started by fixing the horizon radius and setting the coupling constant to a generic value. We initialized ϕ_h, and then ζ_h and ϕ'_h with the conditions at the horizon. We then integrated equations (C.6)-(C.7), obtaining the generic asymptotic behavior for $\phi \sim \text{cost} - \frac{D}{R}$. Finally, we performed a symmetry transformation (3.35) to impose (3.32). This second procedure has the advantage of being faster, since it does not require solving the field equations multiple times to construct a single solution. Furthermore, it simplifies finding multiple solutions for the same coupling constant, when they exist. On the other hand, since it takes advantage of a symmetry of the theory, it can only be used with couplings such that the action is invariant under (3.35).

In both cases, we performed the numerical integration using the fourth-order accurate Runge-Kutta method, starting from the horizon and moving both inward and outward. Even though from an analytical point of view the conditions at the horizon guarantee the regularity of the field equations, the presence of $(1-\zeta^2)$ at the denominator of the equation for the dilaton can cause instabilities when used in a numerical integration algorithm. To overcome this issue we used the following strategy. First we integrated the field equations with the fourth-order accurate Runge-Kutta method for a single step from r_h to $r_h + \frac{\Delta r}{2}$, where Δr is the required grid step. We used the analytic expression of ϕ''_h and ζ'_h (Eqs. (C.9)-(C.10)) as the right-hand sides of the equations at the horizon, while we used Eqs. (C.7)-(C.6) in the intermediate steps. Then, we continued the numerical integration up to the outer boundary using Δr as integration step. We repeated the same procedure inside the BH region and we obtained that in the final numerical data the horizon is staggered between two grid points. We found that, when the static solution was used to initialize the evolution code described in the next section, this strategy produced a better behaved constraint violation with respect to the standard Taylor's expansion at the horizon.

Let me stress that the BH solutions have a curvature singularity inside the horizon [91], so we could only integrate the equations from the horizon inward up to the radius of such singularity. The position of the singularity inside the horizon depends on the specific value of the coupling constant, which motivates the discussion presented in the next subsection.

3.3.3 Properties of the solutions for different γ's

In Fig. 3.5 I show the domain of existence of spherically symmetric BH solutions in the $R_h - M_{\rm BH}$ plane for some representative values of γ. For $\gamma = 1$, there is only one branch of solutions and no local minimum of the BH mass. In this case the minimum-mass solution is also singular at the horizon, as in the shift-symmetric case [142, 144]. For slightly larger values of γ (e.g. $\gamma = \sqrt{2}$ in the plot), there is a critical (minimum-mass) BH which is regular in and outside the horizon. This

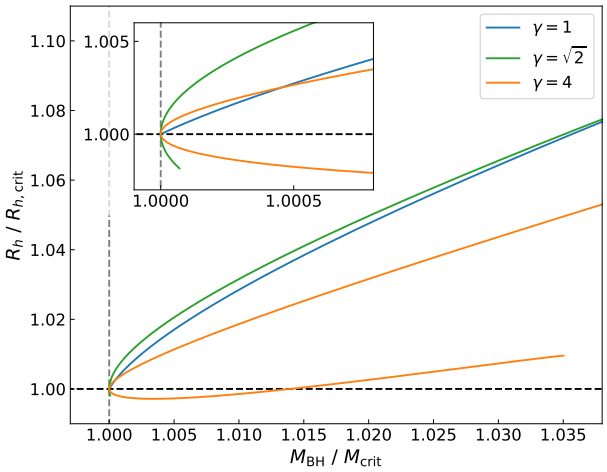

Figure 3.5. Dilatonic solutions in the $R_h - M_{\mathrm{BH}}$ plane for different values of γ. For $\gamma = 1$ the singular configuration has minimum mass, for $\gamma = \sqrt{2}$ a second branch forms and the singular configuration has minimum radius, while for $\gamma = 4$ both the minimum-mass and minimum-radius solutions are regular at the horizon.

solution separates two branches, with the lower one terminating at the minimum-radius solution, which is singular at the horizon [92, 154]. Finally, for even larger values of γ (e.g., $\gamma = 4$ in the plot), also the minimum-radius solution is regular in the BH exterior [155]. In this case the second branch terminates at a different solution which is not the minimum-mass nor the minimum-radius one. Note, however, that the lower branch is linearly unstable [143], therefore the physically interesting solutions are those on the upper branch, and we are particularly interested in the critical (minimum-mass) BH in those cases in which it is regular.

It is also interesting to investigate in more details the location R_s of the curvature singularity inside the horizon as a function of the dilaton coupling. To identify the singularity, we considered the numerical data obtained from the integration in the BH region, which started from the horizon and proceeded inward. At the singularity the denominator D_ϕ in the right-hand side of the equation for the dilaton (Eq. (C.7)) vanishes, thus the algorithm failed and the numerical data became less smooth, featuring spurious jumps. We determined R_s as the radius where this happened, imposing numerical conditions that detected changes of sign or discontinuities in D_ϕ and its derivatives near the root. In Fig. 3.6, I compare the location of the singularity with the horizon radius at the critical BH solution for different values of γ. The units are fixed in such a way that $R_h = 2$. Overall, the smaller the γ the smaller the areal distance between the singularity and the horizon, which also requires higher resolution to resolve the region around the horizon. Thus, in order to reduce the computational cost of the nonlinear time evolution presented Sec. 3.5, in addition to using the radial transformation $R(r)$ we decided to set $\gamma = 4$. We also checked different values of γ, finding a qualitatively similar behavior. Note that in Fig. 3.6 I also show the radius of the excised region, R_e, obtained by initializing the evolution algorithm presented in Sec. 3.4. Details on the excision are given later on.

Finally, in Fig. 3.7 I show the behavior of the excision radius (black curve) and

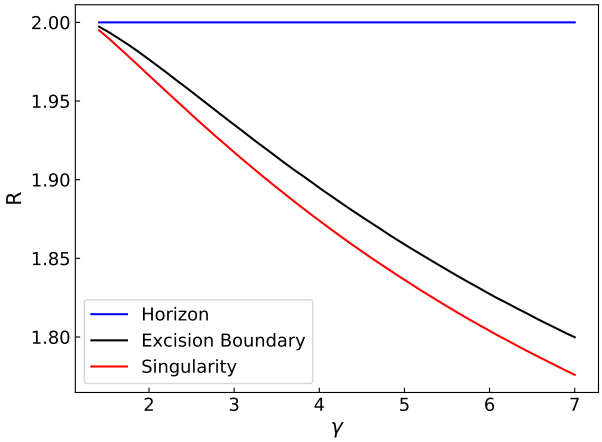

Figure 3.6. Position of the excision boundary and curvature singularity at the critical configuration for different choices of the parameter γ. Given a fixed value of the horizon radius, the radii of the excision boundary and the singularity at the critical configuration decrease as γ increases. For this reason, using larger values of γ allowed us to use larger grid steps and reduce the computational cost.

of the singularity (red curve) with respect to the coupling constant λ when $\gamma = 4$. As anticipated, for the minimum-mass solution the singularity is well within the horizon, whereas near the singular configuration both the excision boundary and the singularity approach the horizon radius. Moreover, since these solutions have been computed at fixed horizon areal radius $R_h = 2$ the coupling constant starts decreasing after the configuration that minimizes $\frac{R_h}{\sqrt{\lambda}}$.

3.4 Numerical setup: initial value problem in EdGB gravity

Having discussed the static dilatonic BH solutions in PG-like coordinates, I now present our numerical setup for the spherical collapse of fields onto a dilatonic BH in EdGB gravity. We mostly followed the formalism used in Ref. [152][5] for shift-symmetric (i.e., $F[\phi] \propto \phi$) EdGB gravity. Let me remind that we considered the collapse both of the dilatonic field ϕ directly coupled to the higher-curvature terms, and that of a phantom field ξ, which was needed to mimic BH evaporation at the classical level.

3.4.1 System of equations and hyperbolicity

To obtain the evolution equations for the system we started by defining the variables

$$Q = \partial_r \phi, \qquad \Theta = \partial_r \xi, \tag{3.36}$$

[5] See also Refs. [85–87, 128, 156–174] for numerical simulations in EdGB/EsGB gravity.

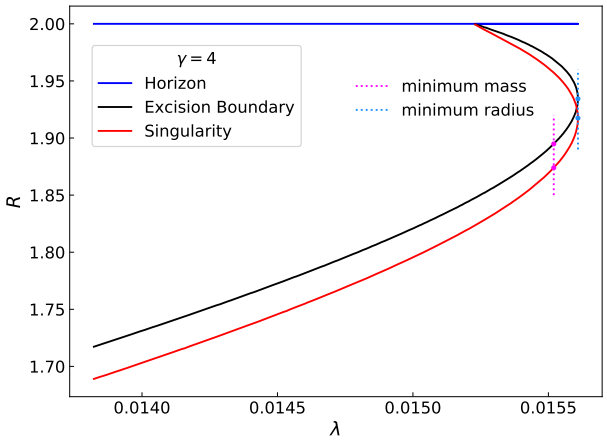

Figure 3.7. Position of the excision boundary (black) and the curvature singularity (red) for the static dilatonic solutions in the case of $\gamma = 4$. Both curves reach the horizon (blue line) at the singular configuration.

and the conjugate momenta

$$P = \frac{1}{\alpha}\partial_t\phi - \frac{\zeta Q}{R'(r)}, \qquad \Pi = \frac{1}{\alpha}\partial_t\xi - \frac{\zeta\Theta}{R'(r)}. \tag{3.37}$$

We then substituted these definitions and the ansatz for the metric in the field equations and obtained a set of 7 evolution equations for ϕ, Q, P, ξ, Θ, Π, ζ, plus 2 constraint equations for α and ζ. All equations are reported in Appendix E. The evolution equations for ϕ and ξ are redundant, since the profiles of the scalar fields can be obtained using Eqs. (3.36) as constraints.

An important aspect to consider when solving systems of partial differential equations is *well-posedness*, which is the requirement that the solution is unique and depends continuously on the initial data [175]. If this condition is not satisfied, not only it is not possible to perform the numerical integration, but the theory itself loses predictive power; indeed, given an initial condition, the solution might not exist, or might be dramatically affected by small variations in initial data, even those that are within measurement uncertainties or truncation errors in numerical computations [175, 176].

Well-posedness is guaranteed by a mathematical condition called *strong hyperbolicity* [177, 178], which I will now introduce following the approach of [179, 180]. While here I will be rather informal, a more in-depth treatment on the topic of well-posedness and hyperbolicity can be found in Refs. [175–178].

Let us consider a first-order system of N partial differential equations. We can define the principal symbol as

$$\mathcal{P}_{IJ}(\eta_\mu) = \frac{\delta E_{v^I}}{\delta\partial_\mu v^J}\eta_\mu, \tag{3.38}$$

where $I, J \in \{1, \dots, N\}$, v^I schematically denotes a variable of the system of equations, E_{v^I} is an equation, and η^μ is a 4-vector.

If there exist N linearly independent vectors $l_I^{(1)}, \dots, l_I^{(N)}$, such that for each $m \in \{1, \dots, N\}$

$$l_I^{(m)} \mathcal{P}_{IJ}(\eta_\mu^{(m)}) = 0, \tag{3.39}$$

with real $\eta_\mu^{(m)}$, then the system of equations is *strongly hyperbolic*. This results in the condition that the so called *characteristic equation*

$$\det \mathcal{P}(\eta_\mu) = 0, \tag{3.40}$$

admits a complete set of real η_μ. The mere existence of real solutions to Eq. (3.40) is instead called *weak hyperbolicity*. While a strongly hyperbolic system is also well-posed, weak hyperbolicity is not sufficient to guarantee well-posedness.

For EdGB gravity it has been shown [152] that there is a region in which the system of evolution equations and constraints in PG-like coordinates is not hyperbolic. Such region generally appeared inside the horizon, where information propagates inward, so it was possible to implement an excision procedure and integrate the equations only where the system was strongly hyperbolic.

We decided to use the same approach, and therefore we derived the condition of hyperbolicity for our set of equations following Ref. [128]. In particular, in our case the variables are $v^I = (\phi, Q, P, \xi, \Theta, \Pi, \alpha, \zeta)$, while the E_{v^I} comprise the field equations written in implicit form (6 evolution equations for ϕ, Q, P, ξ, Θ, Π, and 2 constraint for ζ, α). The determinant of $\mathcal{P}$ has the form

$$\det \mathcal{P} \propto \eta_t^2 \eta_r^2 \left[\mathfrak{a}_\xi \left(\frac{\eta_t}{\eta_r} \right)^2 + \mathfrak{b}_\xi \left(\frac{\eta_t}{\eta_r} \right) + \mathfrak{c}_\xi \right] \left[\mathfrak{a}_\phi \left(\frac{\eta_t}{\eta_r} \right)^2 + \mathfrak{b}_\phi \left(\frac{\eta_t}{\eta_r} \right) + \mathfrak{c}_\phi \right], \tag{3.41}$$

where $\mathfrak{a}_\phi$, $\mathfrak{b}_\phi$, $\mathfrak{c}_\phi$, $\mathfrak{a}_\xi$, $\mathfrak{b}_\xi$, and $\mathfrak{c}_\xi$ are lengthy expressions that depend on all the fields. This determinant vanishes if $\eta_t^2 \eta_r^2 = 0$, $\mathfrak{a}_\phi (\frac{\eta_t}{\eta_r})^2 + \mathfrak{b}_\phi (\frac{\eta_t}{\eta_r}) + \mathfrak{c}_\phi = 0$, or $\mathfrak{a}_\xi (\frac{\eta_t}{\eta_r})^2 + \mathfrak{b}_\xi (\frac{\eta_t}{\eta_r}) + \mathfrak{c}_\xi = 0$. The first equation has two solutions $\eta_r = 0$, which come from the fact that α and ζ are constrained degrees of freedom, and two solutions $\eta_t = 0$, which come from the redundancy of the equations for $\partial_t \phi$ and $\partial_t \xi$.

The second and the third equations have real solutions if the corresponding discriminants, $\Delta = \mathfrak{b}^2 - 4\mathfrak{a}\mathfrak{c}$, are nonnegative. In this case the solutions $c_\pm = -\left(\frac{\eta_t}{\eta_r}\right)_\pm$ are given by

$$c_\pm^{(\phi)} = \frac{\mathfrak{b}_\phi \pm \sqrt{\Delta_\phi}}{2\mathfrak{a}_\phi}, \qquad c_\pm^{(\xi)} = \frac{\mathfrak{b}_\xi \pm \sqrt{\Delta_\xi}}{2\mathfrak{a}_\xi}, \tag{3.42}$$

and are called *characteristic speeds*. In order for the system to be strongly hyperbolic both discriminants

$$\Delta_\phi = \mathfrak{b}_\phi^2 - 4\mathfrak{a}_\phi \mathfrak{c}_\phi \,, \qquad \Delta_\xi = \mathfrak{b}_\xi^2 - 4\mathfrak{a}_\xi \mathfrak{c}_\xi \tag{3.43}$$

have to be positive, so that there are 4 different real characteristic speeds. We referred to the region where this does not happen as the *elliptic region*, somewhat stretching the definition, and, as I will discuss later, we removed it from the domain of integration with an excision strategy.

3.4.2 Initial data

Our purpose was to simulate the evolution of small perturbations of scalar fields around initially static dilatonic BHs. To construct these initial configurations we first used the procedures described in Sec. 3.3 to find the profiles $\phi_0(r)$, $Q_0(r)$, and $\zeta_0(r)$ corresponding to a static isolated BH. Next, we initialized the dilaton as

$$\begin{aligned}
&\phi(r, t=0) = \phi_0(r) + \delta\phi(r), \\
&Q(r, t=0) = Q_0(r) + \delta Q(r), \\
&P(r, t=0) = P_0(r) + \delta P(r) = -\frac{\zeta_0(r)\, Q_0(r)}{R'(r)} + \delta P(r),
\end{aligned} \tag{3.44}$$

where

$$\begin{aligned}
\delta\phi(r) &= \frac{A_{0,\phi}}{R(r)} e^{-\frac{(R(r)-R_{0,\phi})^2}{\sigma_\phi^2}}, \\
\delta Q(r) &= \partial_r \delta\phi(r), \\
\delta P(r) &= \frac{\delta\phi(r)}{R(r)} + \partial_R \delta\phi(r) = \frac{\delta\phi(r)}{R(r)} + \frac{1}{R'}\delta Q(r)\,.
\end{aligned} \tag{3.45}$$

Similarly, since the phantom field vanishes in the background, we initialized its perturbation as

$$\begin{aligned}
\xi(r, t=0) = \delta\xi(r) &= \frac{A_{0,\xi}}{R(r)} e^{-\frac{(R(r)-R_{0,\xi})^2}{\sigma_\xi^2}}, \\
\Theta(r, t=0) = \delta\Theta(r) &= \partial_r \delta\xi(r), \\
\Pi(r, t=0) = \delta\Pi(r) &= \frac{\delta\xi(r)}{R(r)} + \partial_R \delta\xi(r) = \frac{\delta\xi(r)}{R(r)} + \frac{1}{R'}\delta\Theta(r).
\end{aligned} \tag{3.46}$$

In Eqs. (3.45)-(3.46), $A_{0,\phi}$ and $A_{0,\xi}$ represent the amplitudes of the dilaton and phantom perturbations, respectively, $R_{0,\phi}$ and $R_{0,\xi}$ represent the peak value of the Gaussian profiles, whereas σ_ϕ and σ_ξ are the typical widths. The conjugate momenta of the perturbations are similar to Ref. [128]. With this choice, the wave packets are approximately inward moving.

We then integrated the constraints with the fourth-order accurate Runge-Kutta method, starting from the first grid point outside the horizon and moving both outward and inward. We assumed that the perturbations of both fields were far enough from the horizon that we could consider the metric to be initially unperturbed in that region, and we started the numerical integration using the value of ζ obtained from the shooting procedure. Initially we set $\alpha = 1$, and at the end of the initialization process we rescaled it in such a way that $\alpha(r_\infty) = 1$, where r_∞ is the outermost grid point.

The fourth-order accurate Runge-Kutta method requires evaluating the right-hand side of the equations in intermediate grid points. In order to obtain the values of the dilatonic field in these points we constructed the static BH solution using a double resolution compared to that required by the numerical evolution. Namely, if we wanted the grid step of the numerical evolution to be Δr, we performed the

shooting procedure with $\frac{\Delta r}{2}$ as a grid step, and we used half of the grid points as intermediate values for the Runge-Kutta method. We then discarded them at the end of the initialization procedure. We evaluated $\partial_r Q$ and $\partial_r P$ on the right-hand side of the constraints by applying the fourth-order accurate centered finite differences scheme on the data from the shooting procedure, i.e., using the profiles obtained with grid step equal to $\frac{\Delta r}{2}$.

3.4.3 Numerical evolution algorithm

We performed the numerical integration with the method of lines, using the fourth-order accurate Runge-Kutta method for the time integration, and the fourth-order accurate finite differences method for computing the radial derivatives. In particular, at each step of the time integration we used Eqs. (E.1)-(E.7) to evaluate the intermediate profiles of ϕ, Q, P, ξ, Θ, Π, and ζ required by the Runge-Kutta method, and we performed a fourth-order accurate numerical integration of Eq. (E.10) to obtain the profile of α.

This latter numerical integration could not be performed using the Runge-Kutta method, as it requires the evaluation of the fields in intermediate grid steps, whereas in our setup the fields are only defined on the grid points. Nevertheless the constraint for α can schematically be written as

$$\frac{\partial_r \alpha}{\alpha} = L[R, \phi, Q, P, \Theta, \Pi, \zeta], \tag{3.47}$$

where L does not depend on α. The solution then reads

$$\alpha(r) = \exp\Big[\ln \alpha(r_\infty) + \int_{r_\infty}^{r} L\, dr\Big], \tag{3.48}$$

where $\alpha(r_\infty)$ is given by the boundary conditions on the outermost grid point. We computed the integral in the above equation using the trapezoidal rule when r and r_∞ were adjacent grid points, and with a combination of the Simpson's rules in the other cases. In this way we obtained an accuracy of order four in all the numerical grid except in the last grid step.

We used an excision procedure to remove the region where the system was not hyperbolic. The strategy was similar to the one used in Ref. [152]: at the end of each time step we computed the discriminants (3.43), we found the outermost radius in which at least one of the two was nonpositive, and then we excised the region in the interior. The field equations were not evolved in the excised region, thus the radius of the excision boundary R_e could not decrease, but would at most have remained constant if the elliptic region shrunk.

We also monitored the evolution of the apparent horizon, which is located at the coordinate radius r_h where the expansion vanishes, $\theta_{(l)}(r_h) = 0$. We estimated r_h using a linear interpolation. Since the results of the numerical integration lose physical meaning when an elliptic region appears outside the BH[6], we stopped the simulation if the apparent horizon entered in the excision boundary.

[6]Note, however, that since the apparent horizon does not coincide with the event horizon in dynamical situations, the emergence of an elliptic region outside the apparent horizon is not necessarily pathological. In other words, it is not possible to exclude in general that an elliptic region outside the apparent horizon would remain confined within the event horizon.

Finally, we implemented a fifth-order Kreiss-Oliger dissipation scheme in order to stabilize the integration algorithm against high-frequency modes arising from the inner- and near-horizon region. The action of the dissipation term was restricted to the central region by means of a weighting function $\rho(r)$. Specifically, if we schematically denote a generic variable with u, we added to the right-hand side of each evolution equation the term $Q\,u$ contained in Appendix C of Ref. [181], which we expressed as

$$Q\,u = \frac{\eta_{\rm KO}}{64\,\Delta t}(\Delta r)^6 (D_+^3)\rho(D_-^3)u, \tag{3.49}$$

where $\eta_{\rm KO}$ is a constant, Δr is the grid step, Δt is the time step, $\rho = \rho(r)$ is the weighting function, and $D_\pm$ are the operators of first-order numerical differentiation with the one-sided finite difference scheme. In particular, we used $\eta_{\rm KO} = 0.1$ and

$$\rho(r) = \frac{1}{1 + e^{5\,(R(r)-5)}}. \tag{3.50}$$

Since the computation of the numerical derivatives in Eq. (3.49) requires three grid points on each side, we did not use the dissipation term in the three grid points near each boundary of the domain of integration.

3.4.4 Boundary conditions

We did not impose conditions at the excision boundary, since it lied always inside the horizon, where information propagates inward. We only used the upwind differentiation scheme in the first two grid points outside the excision, while we used the centered scheme in the rest of the grid.

At the outer boundary we imposed $\alpha(r_\infty) = 1$, and we kept all the other variables constant in the outermost three grid points, which were used only for computing the numerical derivatives. We could do this since we used numerical grids large enough that the signals coming from the outer boundary did not reach the horizon region we were interested in. Actually, in the code the condition $\alpha = 1$ was imposed at the first point in which the time integration was performed (the fourth outermost grid point), however the errors introduced in α were of order $\frac{1}{R^2}$ and did not affect the accuracy of the code at late times, as we can see from the results of the test simulations reported in Appendix F.

We tested our implementation of the integration algorithm by checking the scaling of the violation of the constraint for ζ. Our code appeared to be accurate and reliable for the evolution of a static dilatonic BH and for the collapsing scenarios discussed in the next sections. The results of the convergence tests are presented in Appendix F.

3.5 Results

I now turn to describe our simulations of the spherical collapse of wave packets on static dilatonic BHs in EdGB gravity. In Secs. 3.5.1 and 3.5.2 I discuss the case of dilatonic perturbations onto BHs in the upper and lower branch, respectively. In Secs. 3.5.3, 3.5.4, and 3.5.5 I consider different setups of phantom perturbations that reduce the BH mass, thus mimicking BH evaporation at the classical level. Let

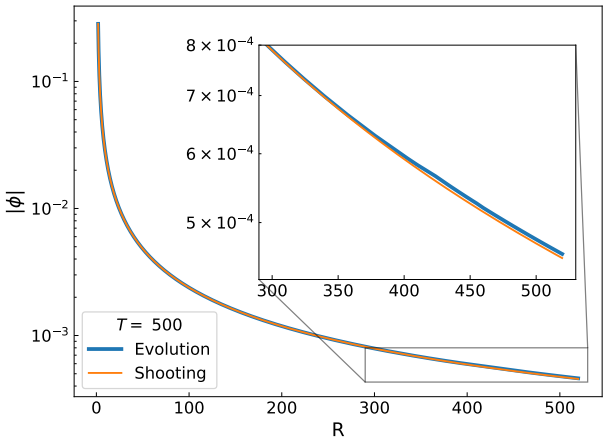

Figure 3.8. Profile of the dilaton ϕ at the end of the simulation of the collapse of a dilaton wave packet on a static BH in the upper branch. The blue curve is obtained at the end of the numerical evolution while the orange curve is obtained from the shooting procedure initialized with the horizon data at $t = T$.

me remind that we used units such that the horizon areal radius of the initial BH is $R_h(t = 0) = 2$, which corresponds to setting the initial BH mass to unity in the GR limit.

3.5.1 Collapse of a dilaton field on a BH in the upper branch

Let me first discuss the case of an initial dilatonic BH in the upper branch. We set the coupling constant to $\lambda = 0.01536$, and we constructed the initial data using the procedure described in Sec. 3.4.2. The parameters A_ϕ, R_ϕ, and σ_ϕ were set to

$$A_{0,\phi} = 0.02, \qquad R_{0,\phi} = 15, \qquad \sigma_\phi = 0.5, \tag{3.51}$$

while $A_\xi = 0$, which implies that the phantom field was always zero in this case. The outer boundary was placed at $R_\infty = 520$, the final simulation time was set to $T = 500$, and the grid step to $\Delta r = 0.01$, with a CFL factor $\text{CFL} = \frac{\Delta t}{\Delta r} = 0.025$. [7]

Since the upper branch is expected to be linearly stable [143], after the dilaton wave packet is absorbed the BH mass should increase, and the end state of the numerical simulation should be approximated by a (slightly heavier) static dilatonic configuration in the upper branch. In order to check this we initialized the shooting algorithm described in Sec. 3.3 with the horizon data at the end of our simulation ($t = T$), and constructed a static dilatonic BH solution. We then compared it with the profile of the dilaton at the end of the simulation, see Fig. 3.8. The profile obtained by the shooting procedure (orange curve) is in excellent agreement with that obtained at the end of the numerical evolution (blue curve), except in the outer region. This is consistent with the fact that the information of the absorption of the pulse has not yet reached the outer boundary.

[7] This small CFL factor was required by the fact that near and inside the horizon the areal radius step ΔR was approximately 20 times smaller than Δr.

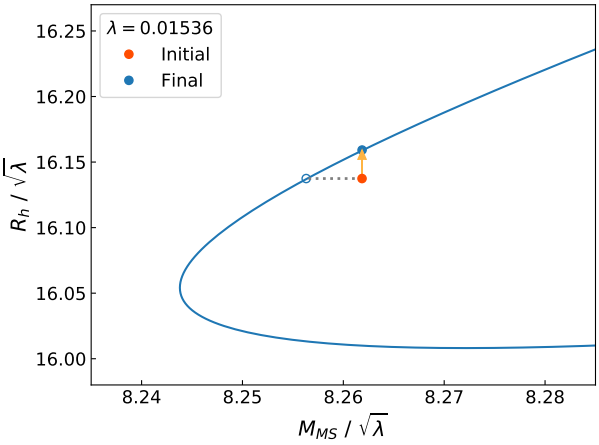

Figure 3.9. Evolution in the $R_h - M_{\rm MS}$ plane for the collapse of a dilaton wave packet on a BH in the upper branch. The blue curve is the domain of existence of static dilatonic solutions, while the blue point represents the static BH configuration that approximates the end state of the numerical evolution.

In Fig. 3.9 I show the evolution of the system during the simulation in the $R_h - M_{\rm MS}$ plane. The point corresponding to the initial configuration (red circle) is on the right of the domain of existence of static dilatonic BH solutions (blue curve), since the wave packet of the dilaton adds a positive contribution to the total Misner-Sharp mass. The initial (isolated) BH solution is marked by an empty circle, connected to the red one by a horizontal dotted line. The blue full circle represents the static configuration that approximates the end state of the numerical integration. It is clear that the final state of the evolution is in the upper branch, providing a first numerical confirmation of the stability of this family of solutions at the fully nonlinear level.

3.5.2 Collapse of a dilaton field on a BH in the lower branch

We then performed a set of four simulations of the same type with different values of the coupling constant λ in the range $[0.01554, 0.0156]$. In this regime, there are two BH solutions for each mass, and we considered those in the lower branch (i.e., with smaller radii) as initial configurations. These solutions should be linearly unstable [143].

We considered a dilaton wave packet with parameters

$$A_{0,\phi} = 0.01, \qquad R_{0,\phi} = 15, \qquad \sigma_\phi = 2.5. \tag{3.52}$$

We used a grid that extends up to $R_\infty = 2850$, with a grid step $\Delta r = 0.02$. The total integration time was set to $T = 2800$.

In Fig 3.10 I show the evolution of the systems in the $R_h - M_{\rm MS}$ plane. In this case the BHs in the lower branch migrate toward the upper branch, hinting at the instability of the former and stability of the latter at the fully nonlinear level. The dynamics of the transition is shown in Fig. 3.11, which contains a plot of the evolution of the apparent horizon areal radius. After the absorption of the wave

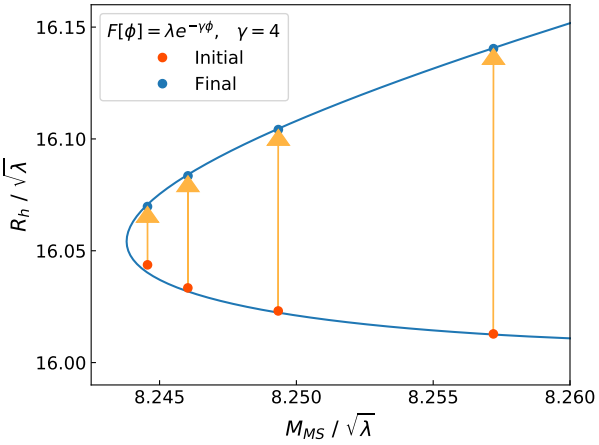

Figure 3.10. Same as in Fig. 3.9 but for the simulations starting from dilatonic BHs in the lower branch. These solutions are unstable and migrate toward stable static BH configurations in the upper branch.

packet, R_h increases with time and approaches a constant value, which corresponds to the horizon radius of the final stable BH configuration. Interestingly, when the wave packet enters in the BH, the horizon areal radius experiences a strong oscillation which is visible at early times. Such behavior is due to the fact that the wave packet, being of dilatonic type, is subject to the nonminimal coupling. To verify this we performed a simulation in which the transition is induced by means of a minimally coupled scalar field, using the code developed for the analysis in Sec. 3.5.5. We obtained that when the wave packet is absorbed by the BH, the horizon areal radius only increases slightly, and the oscillation appearing in Fig. 3.11 is not produced.

3.5.3 Collapse of a phantom field on a dilatonic BH

I now move to discuss the dynamics of dilatonic BHs under a mass loss due to absorption of the phantom field. Let me stress that the role of the phantom field was solely to mimic the mass loss due to BH evaporation at the classical level, but after the absorption of the initial perturbation the evolution was governed only by the nonlinear dynamics of the theory, and the Hawking radiation was not taken into account anymore during the simulation. This allowed us to dynamically reduce the BH mass below the critical value, and investigate the intrinsic behavior of the classical theory in this peculiar regime.

One might be concerned by the fact that a phantom field can lead to pathological dynamics, but this is not the case in spherical symmetry. Indeed, in this case the phantom field does not induce runaway instabilities due to the absence of gravitational-wave emission. We checked this point by performing test simulations of the spherical collapse of a phantom field onto a Schwarzschild BH in GR (see Appendix F). In this case the phantom perturbation is simply absorbed by the BH, which settles down to a stable Schwarzschild solution with a slightly smaller mass (and smaller horizon). Note that here the second law of BH thermodynamics

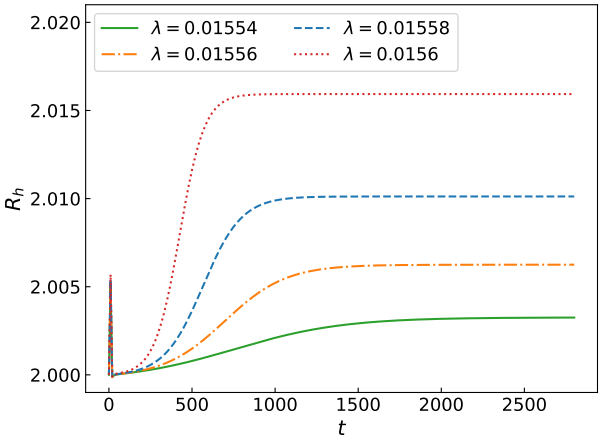

Figure 3.11. Evolution of the apparent horizon for a dilatonic perturbation on an initially static BH in the lower branch, showing the dynamics of the transition from the lower (unstable) to the upper (stable) branch.

is violated even in GR, since the phantom field does not satisfy the null energy condition.

We performed different simulations choosing the coupling constant

$$\lambda = \{0.01543, 0.01545, 0.01547, 0.01549, 0.01551\}, \tag{3.53}$$

which correspond to $R_h/\sqrt{\lambda} = \{16.10, 16.09, 16.08, 16.07, 16.06\}$. The parameters of the initial phantom perturbation (see Eq. (3.46)) were set to

$$A_{0,\xi} = 0.01, \qquad R_{0,\xi} = 15, \qquad \sigma_\xi = 2.5. \tag{3.54}$$

The initial BH was always in the upper branch, and when $\lambda = 0.01551$ the total Misner-Sharp mass at the beginning of the simulation was slightly *smaller* than the critical mass. The outer boundary was at $R_\infty = 2850$, the grid step was $\Delta r = 0.02$, and the final time of integration was $T = 2800$. The CFL factor was again set to 0.025.

The results of the simulations are shown in Fig. 3.12, in which we can see that the BH reaches a final stable configuration as long as the total mass in the spacetime at $t = 0$ is larger than the critical value. For $\lambda = 0.01551$ the situation changes dramatically. In this case the apparent horizon shrinks significantly until it crosses the excision boundary and the simulation ends.

In this specific case we repeated the numerical integration at different resolutions: $\Delta r = \{0.01, 0.005, 0.0025\}$, see Sec. 3.5.4. In Fig. 3.13 I show the dynamics of the apparent horizon and of the excision boundary using the highest resolution. During the last stages of the simulation, the horizon shrinks increasingly fast[8], and at the same time, the excised region expands at a similar pace. Eventually, they cross each other, and the simulation ends.

[8]Note that the small phantom field is accreted in ≈ 10 (in our units). Therefore, as discussed in more detail below, the dramatic shrink shown in Fig. 3.13 at much later times is entirely due to the intrinsic (nonperturbative but classical) dynamics of the theory past criticality, regardless of the details of the phantom-field accretion.

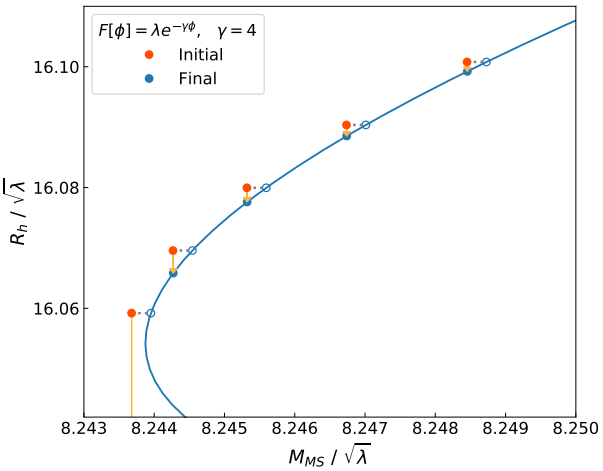

Figure 3.12. Collapse of a wave packet of the phantom field on different dilatonic BH configurations in the upper branch. The BH reaches a final stable configuration as long as the total mass in the spacetime at $t = 0$ is above the critical value $M_{\text{crit}} \sim 8.244\sqrt{\lambda}$. Instead, when $\lambda = 0.01551$ the apparent horizon shrinks significantly and the excised region expands, until it emerges out of the apparent horizon and the simulation ends, see Fig. 3.13.

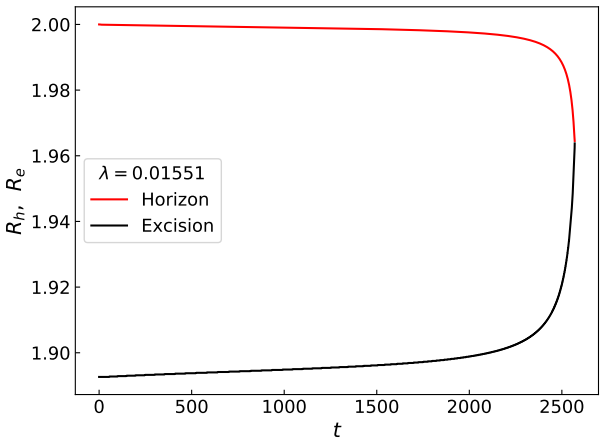

Figure 3.13. Evolution of the apparent horizon and excision boundary for the accretion of a phantom wave packet on a dilatonic BH in the subcritical case. After the initial absorption of the wave packet, on a much longer time scale the apparent horizon shrinks and the excised region expands, until they cross each other. The simulation ends as soon as this happens, due to the presence of elliptic regions outside the BH.

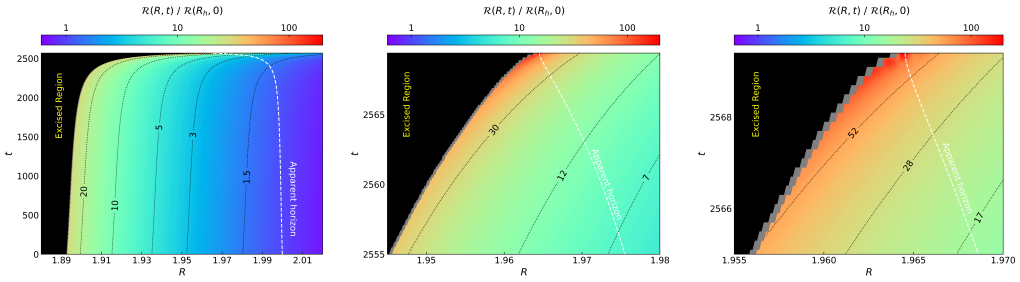

Figure 3.14. Contour plot of the Ricci scalar near the BH region for the simulation that passes the minimum BH mass. The black region is the excised region, and the gray region has been excluded from the computation to avoid inconsistencies due to the change of derivation and dissipation schemes near the excision boundary. The level curves of $\mathcal{R}$ follow the behavior of the excision boundary, and the region of high curvature expands. In the left panel I show the full evolution, while in the middle and right panels I focus on the region where the apparent horizon is about to cross the gray area.

3.5.4 Naked singularity formation in EdGB gravity?

Since in the final time steps of the mass-loss evolution past the critical mass the apparent horizon is rapidly shrinking, it is interesting to understand whether it crosses the singularity, thus violating the weak cosmic censorship [46]. Furthermore, as previously discussed, in the static case the curvature singularity is always inside the elliptic region, and thus it is natural to ask whether the expansion of the elliptic region[9] is related to the curvature singularity moving outward.

To address this point, in Fig. 3.14 I show the spacetime evolution of the Ricci scalar $\mathcal{R}$ in this simulation. The black area is the excised region, while the gray area contains the first 3 grid points in the hyperbolic region. We decided to exclude this region from the computation of $\mathcal{R}$ in order to avoid possible inconsistencies due to the change of the derivation and dissipation schemes.

The curvature at the horizon is modest at the beginning of the simulation ($\mathcal{R}(r_h, t = 0) \approx 0.0089$). However, by the time the apparent horizon crosses the excision (in fact, already when it crosses the gray area in Fig. 3.14), the Ricci scalar at the apparent horizon has grown by a factor ≈ 58 compared to its initial value. This indicates that the apparent horizon is approaching the curvature singularity. It is important to note, however, that the Ricci scalar remains finite throughout the simulation, as the curvature singularity, where $\mathcal{R}$ diverges, is outside the domain integration.

We have performed this simulation with different spatial resolutions ($\Delta r = \{0.02, 0.01, 0.005, 0.0025\}$), finding that the curvature converges well until $t = 2569.0$. This is shown in Fig. 3.15, in which I present the radial profile of the Ricci scalar at different time snapshots and for different resolutions. As a reference, at $t \approx 2569.6$ the apparent horizon has crossed the excision boundary, i.e. only 0.6 after the last

[9]The elliptic region is always inside the excised region, and since the excised region cannot shrink, we do not know the real dynamics of the elliptic region. However, the evolution of the excision boundary is governed by the discriminants (3.43); therefore, if the radius of this boundary increases, then also the elliptic region is expanding.

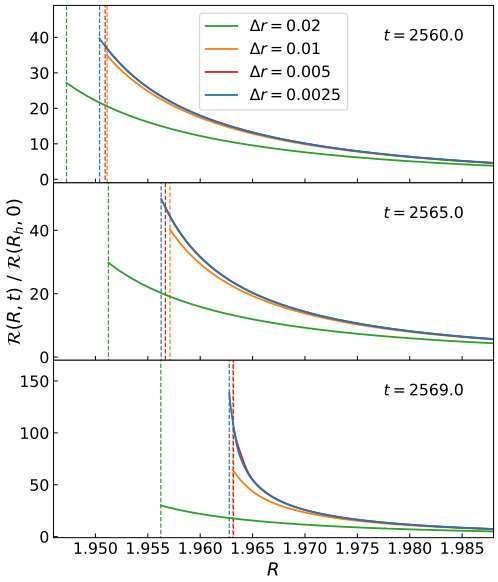

Figure 3.15. Radial profile of the Ricci curvature for the same simulation shown in Fig. 3.14 using different resolutions. Each panel shows a different time snapshot very close to the end of the simulation (as a reference, the apparent horizon has crossed the gray region in Fig. 3.14 at $t \approx 2569.6$). Dashed vertical lines denote the outer boundary of the gray region in Fig. 3.14, so the elliptic region starts close on their left. Overall, as the apparent horizon approaches the elliptic region an increasingly higher resolution is required to make the curvature converge. Furthermore, the curvature dramatically grows before the simulation stops.

snapshot of the bottom panel[10]. Our results show that the curvature when the apparent horizon crosses the gray region grows as the grid step decreases. This suggests that a large curvature region located just across the excision is emerging out of the apparent horizon.

An important point is that the apparent horizon is foliation dependent and, in highly dynamical configurations, it does not generically coincides with the *event* horizon. Furthermore, due to the violation of the null energy condition [88] in EdGB gravity the GR theorem [112] proving that the apparent horizon, if it exists, should always be enclosed by the event horizon does not necessarily apply. However, due to the breakdown of hyperbolicity, the future null infinity of the spacetime might not be complete, leading to difficulties in defining the event horizon. In this regard, we took an operational approach, defining it as the surface where future directed null geodesics converge when traced backwards in time. To explore the dynamics of the event horizon, we then proceeded as follows (see, e.g., Ref. [182] for a similar computation in a different context). For a given null tangent vector n^μ, we computed the null geodesic equation by solving $n^\mu n^\nu g_{\mu\nu} = 0$. In PG-like

[10] As a further check of our code, we have computed the Ricci scalar $\mathcal{R}$ by replacing the field equations in its definition both at the analytical and numerical level. The two computations give the same result.

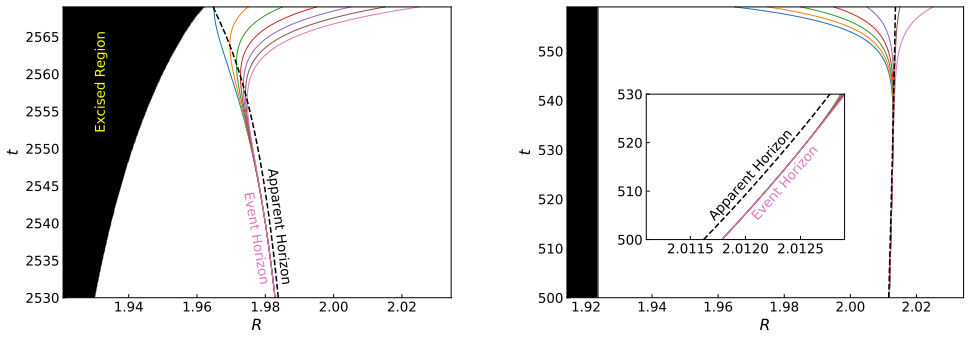

Figure 3.16. Left panel: ray tracing for the simulation showed in Fig. 3.14 to find the event horizon, which corresponds to the surface where the geodesics converge. The event horizon tracks the apparent horizon and shrinks in time toward higher-curvature regions. The fact that the event horizon is within the apparent horizon is a feature of EdGB gravity but is not generic. This is shown in the right panel for a transition from the unstable to the stable branch (rightmost simulation in Fig. 3.10). In this case the event horizon is slightly outside the apparent horizon, as in GR.

coordinates, this translates into

$$\frac{d\,r(t)}{d\,t} = -\frac{\alpha(t,r)}{R'(r)}(\zeta(t,r)-1)\,, \tag{3.55}$$

for outgoing rays described by the radial coordinate $r = r(t)$. We solved this equation backward in time with initial condition $r(t_F) = r_F$ where t_F is near the final time of our simulation (which does not necessarily correspond to a stationary configuration) and r_F is a free parameter. The result is presented in the left panel of Fig. 3.16. This shows two interesting features: i) in the last stages of the simulation the event horizon is *inside* the apparent horizon; this effect is forbidden in GR and it is due to the GB coupling;[11] ii) the event horizon shrinks in time following the same behavior as the apparent horizon, probing regions of increasing curvature.

Intrigued by the fact that the event horizon is located inside the apparent horizon, we performed ray tracing also in other configurations. First of all, already for the same aforementioned simulation we noted that the event horizon and the apparent horizon coincide at times earlier than those shown in the left panel of Fig. 3.16. This is because the dynamics is initially slow. Furthermore, when the dynamics is less extreme, the behavior of the event horizon is more similar to what is expected in GR. This is shown in the right panel of Fig. 3.16, in which I present the ray tracing for a transition from an unstable BH in the lower branch to a stable BH in the upper branch (rightmost simulation in Fig. 3.10). The event horizon approximately tracks the apparent horizon also in this case, but it is (slightly) *outside* of it, as in GR.

Since the curvature singularity is always located inside the excised region, our simulations cannot access the region where $\mathcal{R}$ actually diverges[12]. Nonetheless,

[11] Note that the phantom field is tiny at late times, since it is initially already small and soon gets absorbed by the BH. Thus, the phantom perturbation cannot be responsible for the different dynamics of the horizons at late times.

[12] Note that for the minimum-mass solution the curvature singularity is initially already very

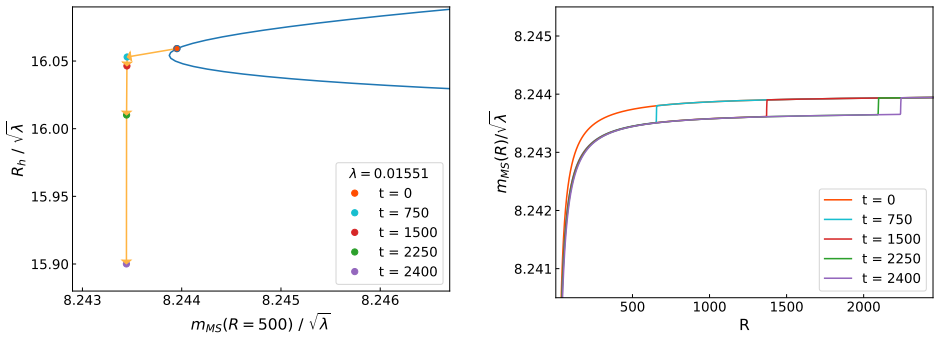

Figure 3.17. Left panel: analog of Fig. 3.12 for a simulation of a pair of negative- and positive-energy wave packets onto a dilatonic BH near the critical mass. As in the leftmost evolution shown in Fig. 3.12, the BH mass decreases past criticality upon accreting the phantom perturbation, triggering a runaway instability on much longer time scales. Right panel: some time snapshots of the Misner-Sharp mass function, $m_{\rm MS}(R)$, for the same simulation. While the Misner-Sharp mass decreases near the BH due to the accretion of the phantom field, as the ordinary field χ moves outward it gives an outgoing positive contribution to the mass function.

it is important to note that the level curves in Fig. 3.14 follow the trajectory of the excision boundary, suggesting that also the radius of the curvature singularity increases during the evolution. Although our formalism is limited, these results might suggest that a naked singularity can form as the outcome of BH evaporation in EdGB gravity. I will come back to this point in the concluding discussion in Chapter. 5.

3.5.5 Emulating Hawking pair production: negative- and positive-energy wave packets emitted near a dilatonic BH

In the simulations discussed so far, we have emulated BH mass loss through the accretion of a phantom perturbation. This was a trick to mimic one of the salient features of Hawking evaporation at the classical level. However, Hawking emission can also be roughly interpreted as pair creation of entangled particles near the horizon [183], with one ("positive-energy") particle escaping to infinity and the other ("negative-energy") particle falling inside the BH and decreasing its mass. In order to emulate Hawking pair production more closely, we considered an extended setup in which we evolved *two* wave packets initially located near the horizon of a dilatonic BH. In particular, besides "vacuum" EdGB gravity, the matter content of the model is described by the action

$$S_{\rm matter} = \frac{1}{16\pi}\int_\Omega d^4x\,\sqrt{-g}\,\left((\nabla\xi)^2 - (\nabla\chi)^2\right)\,, \tag{3.56}$$

where ξ is again the phantom field (that emulates the negative-energy Hawking quantum), while χ is a new minimally-coupled scalar field that emulates the positive-energy Hawking quantum.

close to the outer boundary of the elliptic region, see Fig. 3.6, so the high-curvature region is just across the boundary of the elliptic region.

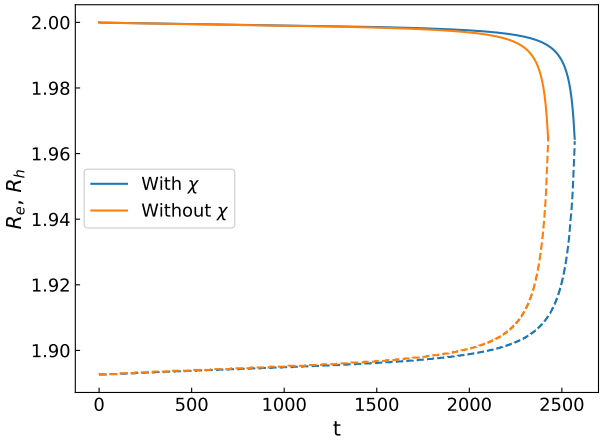

Figure 3.18. Analog of Fig. 3.13 but for the case of a pair of phantom field ξ and ordinary scalar field χ. Solid and dashed curves correspond to the apparent horizons and excision boundaries, respectively. Regardless of the presence of χ and of the details of the initial phantom field, the dynamics is very similar and, on long time scales, leads to a shrink of the apparent horizon and to the formation of a naked elliptic region.

For concreteness, I will present the simulation of a dilatonic BH near the critical configuration to which we added two Gaussian perturbations. For ξ we used the profile in Eq. (3.46), while we initialized χ with the profile

$$\begin{aligned}
\chi(r,t=0) &= \delta\chi(r) = \frac{A_{0,\chi}}{R(r)} e^{-\frac{(R(r)-R_{0,\chi})^2}{\sigma_\chi^2}}, \\
Y(r,t=0) &= \delta Y(r) = \partial_r \delta\chi(r), \\
H(r,t=0) &= \delta H(r) = -\frac{\delta\chi(r)}{R(r)} - \partial_R \delta\chi(r) = -\frac{\delta\chi(r)}{R(r)} - \frac{1}{R'}\delta Y(r),
\end{aligned} \tag{3.57}$$

where $Y := \partial_r \chi$ and $H := \frac{1}{\alpha}\partial_t \chi - \frac{\zeta Y}{R'(r)}$ is the conjugate momentum of the scalar field χ. With these choices the initial perturbation of the phantom field ξ is (approximately) ingoing whereas the initial perturbation of the ordinary field χ is (approximately) outgoing.

The parameters of the profiles (3.46) and (3.57) are set to

$$A_\xi = 8\times 10^{-4}\,, \quad R_{0,\xi} = 2.1\,, \quad \sigma_\xi = 0.02\,, \tag{3.58}$$

$$A_\chi = 7\times 10^{-3}\,, \quad R_{0,\chi} = 2.1\,, \quad \sigma_\chi = 0.02\,. \tag{3.59}$$

In this way the pulses are generated inside the BH photon-sphere (located at $R \approx 3.05$ for an almost critical configuration) and close to the horizon (initially located at $R_H = 2$), but the scalar perturbations approximately vanish on it. The amplitudes are chosen in such a way that the total Misner-Sharp mass is approximately the same as the one of the initial BH, but when the phantom field is absorbed the BH mass decreases below the critical value by an amount similar to those of the simulations presented in the previous sections. We also tried different choices for the wave-packet initial location (e.g., inside and outside the photon-sphere) and width,

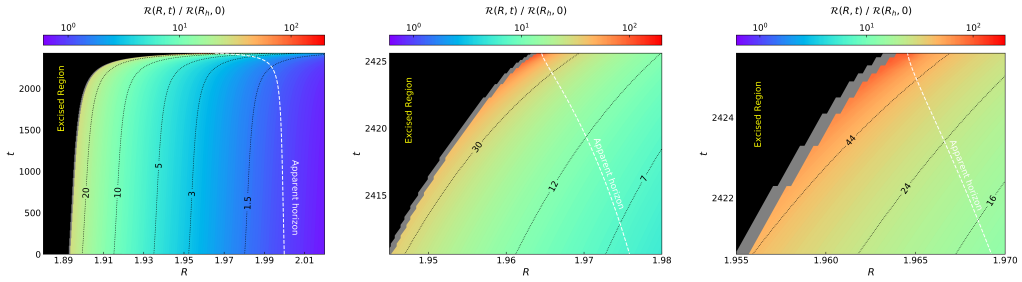

Figure 3.19. Analog of Fig. 3.14 but for an ingoing phantom perturbation and an outgoing standard field perturbation both starting near the horizon (which would more closely mimic the production of a Hawking quantum pair), see main text for details.

the latter parametrizing the frequency content and hence – within the Hawking pair emission analogy – the temperature scale of the evaporating BH. We used a grid step $\Delta r = 0.005$ since, as we can see from Fig. 3.15, this is sufficient to obtain results accurate enough for our purposes. In all cases we obtained the same qualitative features as presented below.

Overall, we observed a very similar dynamics as that presented in Sec. 3.5.3 for a single phantom perturbation. As an example, in the left panel of Fig. 3.17 I show the equivalent of Fig. 3.12 but for this setup with a pair of negative- and positive-energy wave packets. In this case the Misner-Sharp mass shown on the horizontal axis is evaluated at $R = 500$ so for $t \gtrsim 500$ it represents the BH mass without the (positive) contribution of the outgoing field χ. The behavior is qualitatively the same as previously reported: due to the absorption of the small phantom perturbation, the BH mass immediately goes slightly past criticality, where no static BH solutions exist. On much longer time scales, the horizon starts shrinking. The behavior of the Misner-Sharp mass function, $m_{\rm MS}(R)$, at different time snapshots is shown in the right panel of Fig. 3.17, from which it is evident that the BH mass decreases upon accreting the phantom field ξ, whereas the (positive-energy) contribution of the ordinary field χ moves outward as this wave packet reaches infinity.

To further support the generality of this dynamics, in Fig. 3.18 I compare the dynamics of the apparent horizon and excision boundary for two simulations with and without the initial perturbation of the ordinary field χ, showing that the qualitative behavior already presented in Fig. 3.13 – in particular the formation of a naked elliptic region – is the same. This was expected since, as discussed above, there exists a hierarchy of scales between the accretion of the phantom field (reducing the BH mass past criticality) and the formation of a naked elliptic region. The latter occurs when the small phantom field perturbation has been already accreted and cannot play any role in the late-time dynamics. Indeed, the shrinking of the horizon and the appearance of a naked elliptic region are entirely due to the intrinsic, nonperturbative, dynamics of the theory triggered by going past the critical BH solution.

Finally, in Fig. 3.19 I show the analog of Fig. 3.14 in this setup with a pair of negative- and positive-energy wave packets. The striking similarity between Figs. 3.14 and 3.19 confirms that the late-time dynamics does not depend on the details of the BH mass loss past criticality.

Chapter 4

Nonlinear plasma-photon interaction and the black hole superradiant instability

In this chapter I will present the work that I did in collaboration with Enrico Cannizzaro and Prof. Paolo Pani [45], in which we simulated the nonlinear interaction between an electromagnetic (EM) wave packet and a plasma barrier, being interested in application to the superradiant instability.

I will start in Sec. 4.1 introducing the superradiant instability [1] and in Sec. 4.2 I will specialize to the plasma-driven scenario, discussing the issue of nonlinear effects. Then I will start describing the core of our work. In particular, in Sec. 4.3 I will derive the set of evolution equations and constraints for a system composed by the EM field and plasma, which is treated as a fluid, while in Sec. 4.4 I will describe our numerical setup. The results of the simulations will be presented in Sec. 4.5, and their implications for the plasma-driven superradiant instability will be discussed in Sec. 4.6.

4.1 Introduction to the black hole superradiant instability

The extraction of energy from physical systems by means of amplification of radiation, called *superradiance*, is a transversal phenomenon that appears different areas of physics, both in the classical and the quantum world. Indeed, while the term *superradiance* was coined in a work from 1954 by Robert Dicke in the context of quantum optics [184], the occurrence of this phenomenon in classical systems like BHs has attracted considerable interest from the gravity community.

The starting point of this latter line of research can be placed in the early '70s, when Zel'dovich [97, 98], found that cylindrical electromagnetic waves can be amplified by an absorbing rotating cylinder provided that the condition

$$\omega < m\,\Omega \tag{4.1}$$

[1] Clearly the topic is very broad, and while here I will briefly touch many aspects, an in-depth review can be found in Ref. [72].

is met. Here Ω is the angular velocity of the cylinder, ω is the frequency of the wave and m its azimuthal number.

In order to get a sense of this condition it is worth considering the following argument by Zel'dovich. Intuitively, in order to have amplification one should require the velocity of the cylinder to be larger than the phase velocity of the wave. This can be achieved thanks to the cylindrical symmetry of the system: the presence of a multipole moment decreases the angular phase velocity to $\frac{\omega}{m}$, so that it can be in principle lower than Ω, and the condition for this to happen coincides exactly with Eq. (4.1).

In the same seminal papers, Zel'dovich observed that the same phenomenology occurs also for Kerr BHs, with the event horizon playing the role of the absorbing surface of the cylinder, and with Ω in the superradiant condition (4.1) being the angular velocity of the horizon. This scenario was then investigated by Teukolsky and Press, who computed the amplification factors for gravitational and EM waves scattering off a Kerr BH, obtaining that in general this quantity decreases with m, with the maximum value being 138% and 4.4% for the gravitational and EM fields respectively [99].

The possibility of extracting energy from a BH is extremely interesting, as it can be basis of previously unknown macroscopic processes involving BHs and fundamental fields. In this context, a remarkable example if the so called *BH bomb*, a phenomenon occurring in a gedanken experiment devised by Press and Teukolsky in their seminal paper [100]. If a rotating BH is surrounded by a mirror, a wave packet undergoing superradiant scattering close to the BH will not be able to escape to infinity, but will be reflected back and amplified via superradiance multiple times. This results in an exponential growth of the field energy that can lead to the explosion of the mirror.

While at first one might be tempted to think that this process cannot have phenomenological applications, as it is not possible to place a mirror around a BH, it was soon realized that there exist in nature systems exhibiting a mirror-like behavior. It is the case of a massive scalar field [101]: intuitively, the effective potential of the massive field possesses a well that acts as a cavity where modes satisfying the Eq. (4.1) can be exponentially amplified. More formally, it was shown that in the limit $\frac{G\mu M}{\hbar c} \ll 1$, where μ is the scalar field mass and M is the BH mass, the Klein-Gordon equation on a Kerr background can be written in a Schrödinger-like form that is similar the one of the hydrogen atom, and possesses bound-state solutions that are unstable when the superradiance condition is met [102]. Extending these results to a wider range of masses it has been found that when $\frac{G\mu M}{\hbar c} \gg 1$ the instability is suppressed [185], and the largest growth rate of the scalar field occurs for $\frac{G\mu M}{\hbar c} \lesssim 0.5$, meaning that the instability is more efficient when the reduced Compton wavelength of the scalar field $\lambda_{\rm C} = \frac{\hbar}{\mu c}$ is comparable to the BH size $R_{\rm BH} \sim \frac{GM}{c^2}$ [186].

Over the years also higher spin massive fields have been analyzed with various techniques, and it was shown that superradiant instability occurs also for vector [187–192] and tensor [193, 194] fields.

This behavior appears therefore to be generically related to the presence of massive bosons around rotating BH spacetimes, and leads to a rich variety of possible

observational consequences. In particular, energy and angular momentum extraction from the BH via superradiance can take place until the angular velocity of the horizon decreases below ω/m and the condition (4.1) ceases to be valid, leaving a BH surrounded by a boson cloud [195–204] that can then emit gravitational waves [205–218].

Moreover, given the ability of superradiance to reduce the BH spin, one should not expect to observe BHs with parameters corresponding to a sufficiently fast instability time scale. As a result, experimental observations of BHs should populate the Regge plane (*i.e.* the plane J/M^2 vs M, where J and M are the BH angular momentum and mass respectively) in a non-uniform way, producing "holes" in regions determined by the characteristics of the bosonic field under consideration [187, 188, 190, 194, 195, 205, 209, 211, 215, 217].

These are only two possible detectable effects, and do not exhaust the huge impact of the presence of the boson cloud on BH phenomenology, which includes, *e.g.* , modifications in the BH shadow [219–226] and in the dynamics of binary systems [227–239].

The relevance of these effects is maximized in configurations for which the superradiant instability is most efficient, *i.e.* when $\frac{G\mu M}{\hbar c} \approx 0.5$, that results in values of μ that go as $\mu \approx 0.5\frac{\hbar c}{GM} \sim 10^{-10}\left(\frac{M_\odot}{M}\right)\frac{eV}{c^2}$. Bosonic field with such small masses arise in different contexts, as a solution of the strong CP problem in QCD [240–242], as dark matter candidates [243–245], and also in string theory [195,246–248]. Therefore the eventual detection (or absence of detection) of observational signatures of the presence of a boson cloud can be used to constrain the existence of such ultralight bosons [187,188,190,194,209,211,212,217,249–263]. This means that superradiance can not only give us interesting information about the structure of BHs and their interaction with external fields, but also provide a new way to test physics beyond the Standard Model.

4.2 Triggering the superradiant instability with plasma

Another interesting way of triggering the superradiant instability is by means of plasma. Indeed photons behave as effectively massive particles when propagating into plasma, and can therefore be subject to the confining mechanism discussed in the previous section. Starting with a with a brief overview of the necessary plasma physics concepts, here I will introduce the plasma-driven superradiant instability and then discuss the issue of nonlinear effects.

4.2.1 Plasma frequency and dispersion relation for the photon

Plasma is a state of matter in which atoms are ionized, and presents characteristics similar to the ones of a globally neutral gas. Its components, electrons and ions, are subject to the electromagnetic interaction and, having charges with opposite sign, tend to dynamically create disomogeneities in the charge density at the local level.

At the first level of approximation, in order to study the behavior of plasma, one may consider a homogeneous system in which ions and electrons have constant number densities, $n_e = n_{(\text{ions})}$. By studying linear perturbations to this system one

finds that charge density perturbations are characterized by a typical oscillation frequency, called *plasma frequency*, which is given by [103, 104]

$$\omega_p = \sqrt{\frac{n_e e^2}{\varepsilon_0 m_e}}, \tag{4.2}$$

where e is the elementary charge, ε_0 is the vacuum permittivity, and m_e is the electron mass.

Moreover, when studying the propagation of electromagnetic waves through plasma in the same linear regime, one finds the following interesting dispersion relation [104]

$$\omega^2 = c^2 k^2 + \omega_p^2, \tag{4.3}$$

where c is the speed of light, while ω and k are respectively the frequency and the wave vector of the electromagnetic wave. As we can see, the plasma frequency plays the role of an effective mass for the photon, and when considering the superradiance scenario, this can give rise to the instability described in Sec. 4.1.

To better appreciate how this can take place, we can consider the case of an electromagnetic wave impinging on a barrier of plasma. If the frequency of the wave ω is larger than the plasma frequency ω_p, then the wave vector can take real values and the wave can propagate trough the barrier. On the other hand, if $\omega < \omega_p$, then k takes imaginary values, that correspond to an exponential damping of the fields inside the barrier [104] and a reflection of the wave. Imagining this as a rudimentary description of the interaction between the plasma surrounding a BH and an electromagnetic wave that has undergone a superradiant scattering process, we see that in the regime $\omega < \omega_p$ the system exhibits the mirror-like behavior that can trigger a superradiant instability.

4.2.2 Superradiant instability

The existence of an effective mass for the photon, however, does not guarantee that the superradiant instability is efficient enough to be observed, but we have the additional requirement that $\mu \approx 10^{-10}\left(\frac{M_\odot}{M}\right)\frac{eV}{c^2}$, which results in $\omega_p = 10^5\left(\frac{M_\odot}{M}\right)\frac{\text{rad}}{s}$. Conlon and Herdeiro [107] noticed that for stellar mass BHs ($M \approx 1 \div 100\, M_\odot$) this optimal value can be reached in intracluster environments where $n_e \approx 10^{-3} \div 10^{-2} cm^{-3}$, as $\omega_p \approx 10^3\sqrt{\frac{n_e}{10^{-3}cm^{-3}}}\,\frac{\text{rad}}{s}$, and they also considered the interesting possibility that BHs undergoing plasma-driven superradiant instability in these environments are the source of the observed Fast Radio Bursts. Moreover, plasma is present also in the early Universe, and Pani and Loeb [106] have studied how the eventual superradiant instability of primordial black hole can alter the spectrum of the cosmic microwave background.

These studies were performed approximating the EM field as a Proca field with constant mass ω_p, and while the results already show the potential relevance of this phenomenon, the approach used suffers mainly from two limitations. Firstly, as noted in [108], Proca waves have three propagating degrees of freedom, two transverse and one longitudinal, while an EM wave propagating in a cold plasma has only two propagating degrees of freedom, since the longitudinal one is electrostatic.

Secondly, while the assumption of a constant ω_p holds for a homogeneous plasma, it might be not valid for the more complex density profiles that appear when accretion is included.

In order to address this latter issue, Dima *et al.* [264] performed numerical simulations of the superradiant amplification with a varying plasma frequency, using a toy model in which the EM field was replaced by a massive Klein-Gordon field. Cannizzaro *et al.* [108,109], instead, carried out a linear analysis in which they used the Maxwell's equations and a fluid description for the plasma, finding quasibound states that become unstable when the superradiance condition (4.1) is met, even in the case of a spatially-dependent ω_p.

4.2.3 Nonlinear regime

While linear studies show that plasma is capable of triggering a superradiant instability, the presence of an exponential growth of the electromagnetic field demands to investigate the impact of nonlinear effects in this process.

This was first done in Ref. [110] where it was pointed out that at the nonlinear level circularly polarized transverse EM waves can propagate in a homogeneous plasma even if [111]

$$\omega_p\left(1+\left(\frac{eE}{m_e c\omega}\right)^2\right)^{-1/4} < \omega < \omega_p, \tag{4.4}$$

where E is the amplitude of the electric field. This effect, called *plasma transparency*, can be viewed as due to the fact that electrons are accelerated to relativistic speed by the electric field, and their relativistic mass increases, resulting in an effective reduction of the plasma frequency to

$$\omega_p \to \sqrt{\frac{n_e e^2}{m_e \varepsilon_0 \sqrt{1+\left(\frac{eE}{m_e c\omega}\right)^2}}}. \tag{4.5}$$

Eq. (4.4) can also be translated into a lower threshold for E above which radiation is able to propagate through plasma:

$$E > E_{\rm crit}^{\rm trans} = \frac{m_e c}{e}\sqrt{\frac{\omega_p^4}{\omega^2}-\omega^2}, \tag{4.6}$$

where, here and in the rest of the thesis, $\omega_p = \sqrt{\frac{n_e e^2}{m_e \varepsilon_0}}$ as a convention.

This poses a bound on the amount of energy that can be extracted via plasma-driven superradiant instability, since confinement of radiation is possible only for small values of E, and as soon as it reaches the critical value $E_{\rm crit}^{\rm trans}$ the plasma will become transparent, dispersing the accumulated EM energy to infinity.

This is not the only mechanism that can quench the amplification process [265], but is the most relevant, and can severely limit the possibility of detecting observational signatures of the superradiant instability, as it come into play when only a small amount of energy has been extracted from the BH [110].

Even though such an argument shows exceptionally well the potential impact of nonlinear effects, the existence of the solutions found in Ref. [111] is made possible

by a vanishing Lorentz term (the cross product of the velocity of electrons times the magnetic field, $\vec{v}\times\vec{B}$), which has the effect of crucially reducing the nonlinear terms, allowing low-frequency, circularly polarized, transverse waves with large amplitude to propagate inside a homogeneous plasma without inducing an evolution of the density profile, or a longitudinal motion of electrons. These characteristics are hardly representative of the superradiance scenario, where deviations from the planar geometry, different polarizations, and an inhomogeneous profile of the plasma density are to be expected. In the more generic case where these possibilities are included the phenomenology is significantly richer as transverse and longitudinal modes are coupled, and plasma can evolve. For instance, by considering a circularly polarized wave scattering off a sharp boundary plasma it was found [266] that electrons tend to pile up in narrow regions, increasing the plasma density and the threshold for relativistic transparency. Moreover, 1D numerical simulations show [267, 268] that in this case while propagation of low-frequency radiation is possible, plasma does not genuinely behave as transparent, but in an articulated fashion involving complex profiles of the plasma density. It is therefore clear from these results that removing restrictions from the system of evolution equations can significantly affect the dynamics, and in order to assess whether nonlinear effects can hamper the superradiant instability, a more complete description has to be used.

With these considerations in mind, in our work [45] we developed a code to perform the 3+1 nonlinear numerical evolution of systems composed by the EM field and plasma. Clearly, this is a classical topic in plasma physics (see Ref. [269] for a review), but in our work, being interested in the applications to BH superradiance, we focused on a regime that is seldom studied in standard plasma-physics applications, namely a low-frequency, high-amplitude EM wave propagating in an inhomogeneous overdense plasma.

4.3 Field equations

For simplicity, and because the stress-energy tensor of the plasma and EM field is negligible even during the superradiant growth, we considered a fixed background and neglected the gravitational field. We considered a system composed by the EM field and a plasma fluid, described by the field equations (in rationalized Heaviside units with $c = 1$):

$$\nabla_\mu F^{\mu\nu} = J^\nu, \tag{4.7}$$

$$u^\nu \nabla_\nu u^\mu = \frac{e}{m_e} F^{\mu\nu} u_\nu, \tag{4.8}$$

$$\nabla_\mu (n_e u^\mu) = 0, \tag{4.9}$$

where $F_{\mu\nu}$ is the EM tensor, J^μ is the EM 4-current, u^μ is the 4-velocity field for the plasma fluid, and n_e is the rest number density of electrons inside the plasma. Note that we considered a fluid model with vanishing pressure, as in the regime of interest for plasma-driven superradiant instability pressure is expected to be small and to give negligible contributions [108, 109]. However, a relevant limitation is that, due to this choice, the system can undergo the formation of caustics, with

divergences in the plasma density. I will come back on this point when discussing the results of our numerical simulations.

Having in mind future extensions, we performed a $3+1$ decomposition of the field equations that is valid for any curved background spacetime. However, in this work we performed our simulations in flat spacetime, $ds^2 = \eta_{\mu\nu}\, dx^\mu\, dx^\nu$.

4.3.1 $3+1$ decomposition of the field equations

Generic spacetime

Let us introduce a foliation of the spacetime into spacelike hypersurfaces Σ_t, orthogonal to the 4-velocity of the Eulerian observer n^μ. We then express the line element as

$$ds^2 = -(\alpha^2 - \beta_i\beta^i)\, dt^2 + 2\,\beta_i\, dx^i\, dt + \gamma_{ij}\, dx^i\, dx^j, \tag{4.10}$$

where α is the lapse, β^i is the shift vector, and γ_{ij} is the spatial 3-metric. We can define the electric and the magnetic fields as [121]

$$E^\mu = -n_\nu F^{\nu\mu}, \qquad B^\mu = -n_\nu F^{*\nu\mu}, \tag{4.11}$$

where $F^{*\mu\nu} = -\frac{1}{2}\epsilon^{\mu\nu\lambda\sigma}F_{\lambda\sigma}$ is the dual of $F^{\mu\nu}$. The EM tensor can be decomposed as

$$F^{\mu\nu} = n^\mu E^\nu - n^\nu E^\mu + {}^{(3)}\epsilon^{\mu\nu\sigma}B_\sigma, \tag{4.12}$$

where ${}^{(3)}\epsilon^{\mu\nu\sigma} = n_\lambda\epsilon^{\lambda\mu\nu\sigma}$ is the Levi-Civita tensor of the spacelike hypersurface Σ_t. Note that E^μ and B^μ are orthogonal to n^μ and are spacelike vectors on the 3-surfaces Σ_t.

We can define the charge density as $\rho = n_\mu J^\mu$, and the 3-current as ${}^{(3)}J^\mu = h^\mu{}_\nu J^\nu$, where $h^\mu{}_\nu$ is the projection operator onto Σ_t. Finally, we can write the Maxwell's equations as [121]

$$D_iE^i = \rho, \tag{4.13}$$

$$D_iB^i = 0, \tag{4.14}$$

$$\partial_t E^i = \mathcal{L}_\beta E^i + \alpha K E^i + [\vec{D}\times(\alpha\vec{B})]^i + \alpha\,{}^{(3)}J^i, \tag{4.15}$$

$$\partial_t B^i = \mathcal{L}_\beta B^i + \alpha K B^i - [\vec{D}\times(\alpha\vec{E})]^i, \tag{4.16}$$

where D_i is the covariant derivative with respect to the 3-metric γ_{ij}, and K_{ij} is the extrinsic curvature. Here the first equation is the Gauss' law, the second equation is equivalent to the absence of magnetic monopoles, and the last two are the evolution equations for the electric and magnetic fields, respectively. The EM 4-current is given by ions and electrons $J^\mu = J^\mu_{(\mathrm{ions})} + J^\mu_{(e)}$. We assume ions to be at rest, due to the fact that $m_e \ll m_{(\mathrm{ions})}$, so that $J^\mu_{(\mathrm{ions})} = -\rho_{(\mathrm{ions})}n^\mu$. For electrons instead we have $J^\mu_{(e)} = -en_eu^\mu$. Let us decompose u^μ into a component along n^μ, $\Gamma = -n^\mu u_\mu$, and a component on the spatial hypersurfaces, ${}^{(3)}u^\mu = h^\mu{}_\nu u^\nu$. The 4-velocity of the fluid can be written as

$$u^\mu = \Gamma n^\mu + {}^{(3)}u^\mu = \Gamma(n^\mu + \mathcal{U}^\mu)\,, \tag{4.17}$$

where $\mathcal{U}^\mu$ is defined by ${}^{(3)}u^\mu = \Gamma\mathcal{U}^\mu$. The above expression allows us to write $\rho = n_\mu J^\mu = \rho_{(\text{ions})} + \rho_{(e)} = \rho_{(\text{ions})} + en_{EL}$, where $n_{EL} = \Gamma n_e$ is the electron density as seen by the Eulerian observer. The density of ions is constant in time, and will be fixed when constructing the initial data[2]. As $J^\mu_{(\text{ions})}$ is orthogonal to Σ_t, the 3-current ${}^{(3)}J^\mu$ receives only contributions from electrons, and we have ${}^{(3)}J^\mu = -en_e\Gamma\mathcal{U}^\mu = -en_{EL}\mathcal{U}^\mu$. Thus, the source terms that appear in Eqs. (4.13)-(4.15) are

$$\rho = \rho_{(\text{ions})} + en_{EL}, \qquad {}^{(3)}J^\mu = -en_{EL}\mathcal{U}^\mu. \tag{4.18}$$

Let us now move to Eq. (4.8). Projecting it on n^μ and Σ_t we obtain respectively (see Appendix G for the explicit computation):

$$\partial_t\Gamma = \beta^i\partial_i\Gamma - \alpha\mathcal{U}^i\partial_i\Gamma + \alpha\Gamma K_{ij}\mathcal{U}^i\mathcal{U}^j - \Gamma\mathcal{U}^i\partial_i\alpha + \frac{e}{m_e}\alpha E^i\mathcal{U}_i\,, \tag{4.19}$$

$$\begin{aligned}\partial_t\mathcal{U}^i = {}&\beta^j\partial_j\mathcal{U}^i - \mathcal{U}^j\partial_j\beta^i - \alpha a^i - \alpha\mathcal{U}^iK_{jl}\mathcal{U}^j\mathcal{U}^l + 2\alpha K^i{}_j\mathcal{U}^j + \mathcal{U}^i\mathcal{U}^j\partial_j\alpha - \alpha\mathcal{U}^jD_j\mathcal{U}^i \\ &+ \frac{\alpha}{\Gamma}\frac{e}{m_e}\Big(-\mathcal{U}^iE^j\mathcal{U}_j + E^i + {}^{(3)}\epsilon^{ijl}B_l\mathcal{U}_j\Big)\end{aligned} \tag{4.20}$$

Finally, we can write the continuity equation (4.9) as

$$\partial_t n_{EL} = \beta^i\partial_i n_{EL} + \alpha K n_{EL} - \alpha\mathcal{U}^i\partial_i n_{EL} - \alpha n_{EL}\nabla_\mu\mathcal{U}^\mu. \tag{4.21}$$

While the above decomposition is valid for a generic background metric, from now on we will focus on a flat spacetime.

Flat spacetime

Let us use Cartesian coordinates, so that $g_{\mu\nu} = \eta_{\mu\nu} = \text{diag}\{-1,1,1,1\}$. As a consequence, we have that for any 3-vector ${}^{(3)}V^i = {}^{(3)}V_i$, and

$$\alpha = 1, \qquad \beta^i = 0, \qquad K_{ij} = 0. \tag{4.22}$$

In these coordinates the equations for the EM field can be written as

$$\partial_iE^i = \rho_{(\text{ions})} + en_{EL}, \tag{4.23}$$

$$\partial_iB^i = 0, \tag{4.24}$$

$$\partial_tE^i = [\vec{\partial}\times\vec{B}]^i - en_{EL}\mathcal{U}^i, \tag{4.25}$$

$$\partial_tB^i = -[\vec{\partial}\times\vec{E}]^i, \tag{4.26}$$

the evolution equations for Γ and $\mathcal{U}^i$ as

$$\partial_t\Gamma = -\mathcal{U}^i\partial_i\Gamma + \frac{e}{m_e}E^i\mathcal{U}_i, \tag{4.27}$$

$$\partial_t\mathcal{U}^i = -\mathcal{U}^j\partial_j\mathcal{U}^i + \frac{1}{\Gamma}\frac{e}{m_e}\Big[-\mathcal{U}^iE^j\mathcal{U}_j + E^i + (\vec{\mathcal{U}}\times\vec{B})^i\Big], \tag{4.28}$$

and the continuity equation as

$$\partial_t n_{EL} = -\mathcal{U}^i\partial_i n_{EL} - n_{EL}\partial_i\mathcal{U}^i. \tag{4.29}$$

Moreover, from the normalization condition $u^\mu u_\mu = -1$ we can obtain a constraint for Γ and $\mathcal{U}^i$:

$$\Gamma^2(1 - \mathcal{U}^i\mathcal{U}_i) = 1. \tag{4.30}$$

[2]Note that with the conventions we used, electrons carry *positive* charge, while ions carry *negative* charge.

4.4 Numerical setup

I now move to discuss our numerical setup, describing the integration scheme and the initialization procedure.

4.4.1 Integration scheme

We evolved $\vec{E}$, $\vec{B}$, Γ, $\vec{\mathcal{U}}$, and n_{EL} with Eqs. (4.25)-(4.29), using the constraints (4.23) and (4.30) to evaluate the convergence of the code. The profile of $\rho_{(\text{ions})}$ was kept constant, consistently with the approximation that ions are at rest. For the numerical integration we used the fourth-order accurate Runge-Kutta algorithm, computing the spatial derivatives with the fourth-order accurate centered finite differences scheme. For simplicity we simulated the propagation of *plane* EM wave packets along the z direction, and therefore we obtained field configurations that are homogeneous along the x and y directions. This feature allowed us to impose periodic boundary conditions in the x and y directions, as they preserve the homogeneity of the solution without introducing numerical instabilities. We imposed periodic boundary conditions also on the z axis, while choosing grids with extension along z large enough that the wave packet does not interfere with itself during the all duration of the simulations.

4.4.2 Initialization procedure

When constructing the initial data for the simulations we first set the profile of the plasma. We started by setting $\Gamma(t=0,\vec{x})=1$ and $\vec{\mathcal{U}}(t=0,\vec{x})=0$, so that the plasma is initially at rest. Then, we initialized the profile of n_{EL} with barrier-like shape of the following form:

$$n_{EL}(t=0,\vec{x}) = 2n_{\text{bkg}} - n_{\text{max}} + (n_{\text{max}} - n_{\text{bkg}})\Big[\sigma(z;W_1,z_1)+\sigma(z;-W_2,z_2)\Big], \quad (4.31)$$

Where $\sigma(z;W,z_0)=(1+e^{-W(z-z_0)})^{-1}$ is a sigmoid function. The qualitative behavior of Eq. (4.31) is shown in Fig. 4.1, where we can see that n_{bkg} is the background value of the plasma density and n_{max} is the plasma density at the top of the barrier. The parameters $z_{1,2}$ determine the location and width of the barrier, while the parameters $W_{1,2}$ control its steepness. Note that this profile was chosen to reproduce a very crude toy model of a matter-density profile around a BH [270], where the accretion flow peaks near the innermost stable circular orbit and is depleted between the latter and the BH horizon. Finally, the constant profile of $\rho_{(\text{ions})}$ was determined by imposing that the plasma is initially neutral, so that $\rho_{(\text{ions})}(t=0,\vec{x}) = -en_{EL}(t=0,\vec{x})$. Once the profile of the plasma had been assigned we could proceed to initialize the EM field. We considered a circularly polarized wave packet moving forward in the z-direction:

$$\vec{E} = A_E \begin{pmatrix} \cos[k_z(z-z_0)] \\ \sin[k_z(z-z_0)] \\ 0 \end{pmatrix} e^{-\frac{(z-z_0)^2}{2\sigma^2}}, \quad (4.32)$$

$$\vec{B} = A_E \frac{k_z}{\omega} \begin{pmatrix} -\sin[k_z(z-z_0)] \\ \cos[k_z(z-z_0)] \\ 0 \end{pmatrix} e^{-\frac{(z-z_0)^2}{2\sigma^2}}, \quad (4.33)$$

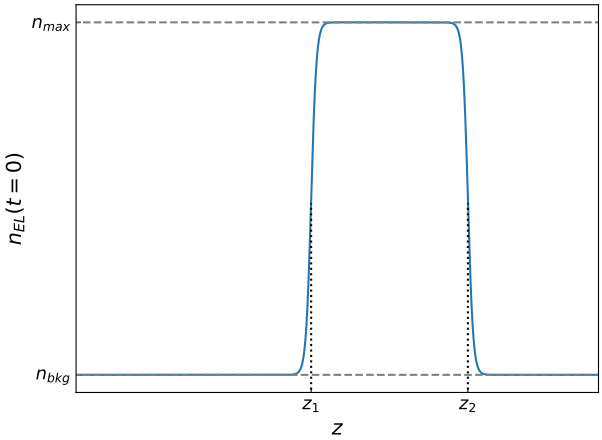

Figure 4.1. Qualitative behavior of the barrier-shaped initial profile for the plasma, Eq. (4.31). $n_{\max}$ and $n_{\rm bkg}$ are the values of the plasma density inside the barrier and on the background, while the parameters $z_{1,2}$ and $W_{1,2}$ determine the position and the steepness of the boundaries of the barrier, respectively.

where A_E is the amplitude of the wave packet, σ is its width, z_0 its central position, ω is the frequency, and $k_z = \sqrt{\omega^2 - \omega_p^2}$, where $\omega_p = \sqrt{\frac{e^2\, n_{\rm bkg}}{m_e}}$ is the plasma frequency computed using $n_{\rm bkg}$, as the wave packet is initially located outside the barrier (i.e., $\sigma \ll z_1 - z_0$).

Let me stress that while the configuration we considered is by no means realistic, it allowed us to study the nonlinear interaction between EM field and plasma in a setup that already gives an intuition on the possible implications for the superradiance scenario.

4.5 Results

Here I present the results of our numerical simulations of nonlinear plasma-photon interactions in different configurations. We considered a low-frequency, circularly polarized wave packet propagating along the z direction and scattering off the plasma barrier with the initial density profile given by Eq. (4.31).

4.5.1 Linear regime

As a consistency check of our code, we tested that for sufficiently low amplitude waves our simulations were in agreement with the predictions of linear theory. We set units such that $e = m_e = 1$ and considered an initial wave packet of the electric field centered at $z_0 = 0$, with a characteristic width $\sigma = 5$. We also set $\omega = 0.5$ and $A_E = 10^{-6}$, so that the evolution could be described by the linear theory. The plasma barrier was situated between $z_1 = 40$ and $z_2 = 100$, and we set $W_1 = W_2 = 1$. The background density of the plasma was $n_{\rm bkg} = 0.01$ so that $\omega_p^{(\rm bkg)} = 0.1$ and all the frequency content of the EM wave was above the plasma frequency of the background. We ran 6 simulations with $n_{\max} =$

$\{n_{\rm bkg}, 0.25, 0.5, 0.75, 1, 1.25\}$, that correspond to plasma frequencies at the top of the barrier $\omega_p^{(\max)} = \{0.1, 0.5, 0.707, 0.866, 1, 1.12\}$, respectively, and fall in different parts of the frequency spectrum of the EM wave packet. In the linear regime, we expected that the frequency components above $\omega_p^{(\max)}$ propagated through the plasma barrier, while the others were reflected, and this setup allowed us to clearly observe this mechanism at play. In all these simulations we used a grid that extends in $[-1, 1] \times [-1, 1] \times [-450, 450]$, with a grid step $\Delta x = \Delta y = \Delta z = 0.2$ and a time step $\Delta t = 0.1$, so that the CFL factor was CFL $= 0.5$. The final time of integration was set to $T = 400$.

Figure 4.2 shows some snapshots of the numerical results at different times for different values of $\omega_p^{(\max)}$. It is evident that the analytical predictions of linear theory are confirmed: as the plasma frequency of the barrier increases, less and less components are able to propagate through it and reach the other side. In particular, when $\omega_p^{(\max)} \gtrsim 0.9$ the wave is almost entirely reflected, and the transmitted component becomes negligible. Furthermore, in the linear regime the backreaction on the density is effectively negligible, as the barrier remains constant over the entire simulation (in fact, we observed a maximum variation of n_{EL} of the order of 10^{-11}, which is clearly not appreciable on the scale of Fig. 4.2).

To better quantify the frequency components that are propagated and the agreement between the simulations and the analytic expectation in the linear regime, we computed the (discrete) Fourier transform of the time evolution of E^x in two points along the z axis: $z = -50$ and $z = 150$, which are located before and after the plasma barrier, respectively. Figure 4.3 shows the absolute value of the Fourier transform for the different values of the plasma frequency in the barrier, which are represented as vertical dotted lines. As we can see from the Fourier transform at $z = 150$, the transmitted waves have only components with frequency $\omega > \omega_p^{(\max)}$, in agreement with the fact that only modes above this threshold can propagate. Hence, the barrier perfectly acts as a high-pass filter, with a critical threshold given by the plasma frequency.

4.5.2 Nonlinear regime

We then proceeded to increase the amplitude of the field until linear theory breaks down and the interaction becomes fully nonlinear. As anticipated, the evolution is more involved than in the idealized model described in [111]. Indeed, even from a first qualitative analysis, it is evident from the z-component of the momentum equation (4.28) that in the nonlinear regime electrons will experience an acceleration along the z axis due to the nonlinear Lorentz term $(\vec{\mathcal{U}} \times \vec{B})^z$. The formation of a current along the z directions implies a modification of the density profile because of the continuity equation, and also the formation of a longitudinal electric field that tries to balance and preserve charge neutrality. In the following, I will support this qualitative analysis with the results of our numerical simulations and show that nonlinear effects can have a dramatic impact on the system dynamics.

In this set of simulations, we set units[3] such that $e = 1$ and $m_e = 1000$, and we

[3] Note that, in rationalized Heaviside units, changing m_e (and hence the classical electron radius) simply accounts for rescaling lengths, times, and masses in the simulations. Lengths and times are

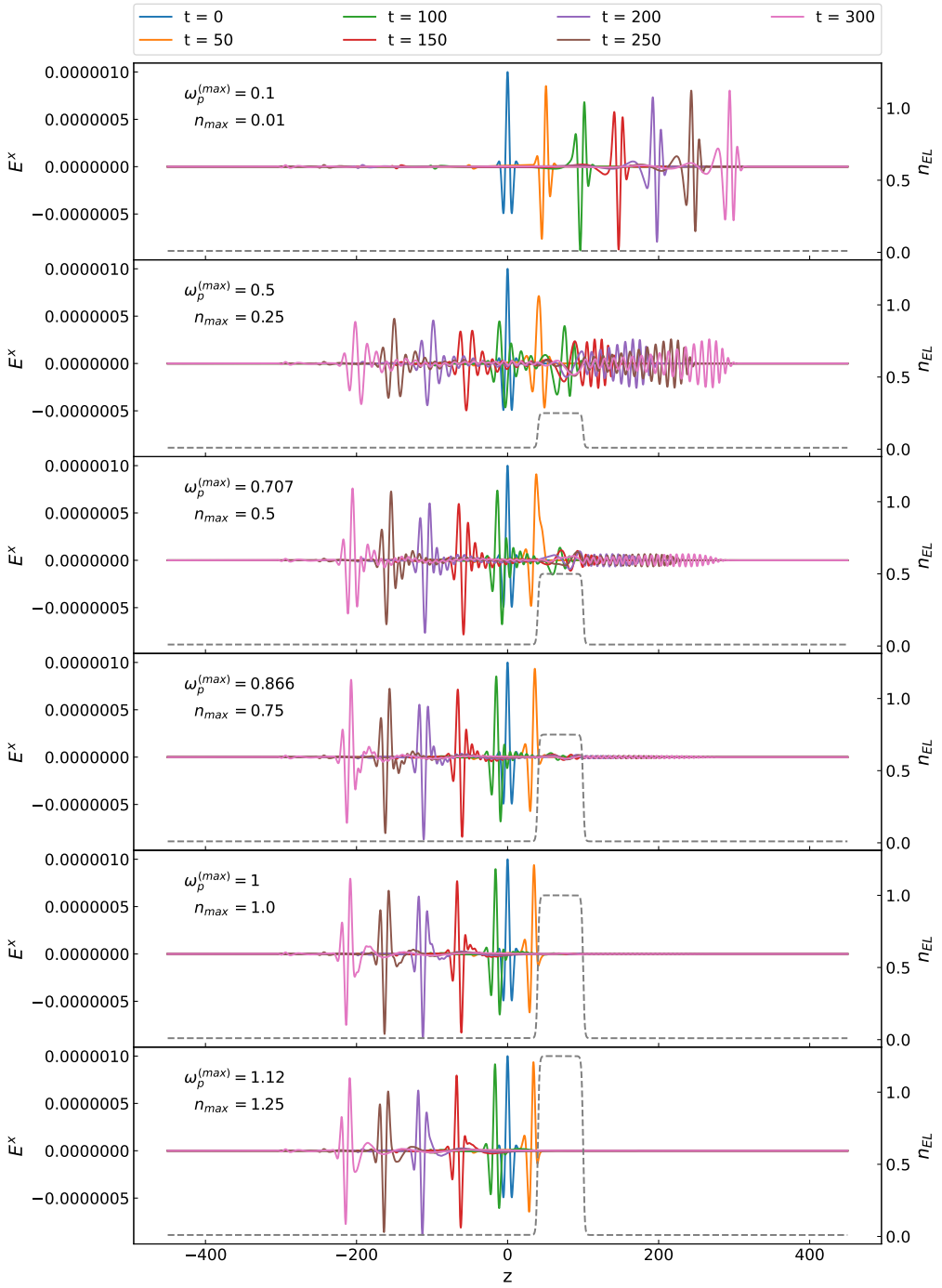

Figure 4.2. Propagation of an EM wave packet on a barrier of plasma in the linear regime. Here I show some snapshots of the evolution of E^x for different values of the plasma density in the barrier, $n_{\max}$, representing the initial profile of n_{EL} with a gray dashed line. When the plasma frequency in the barrier $\omega_p^{(\max)}$ becomes larger than ω, the wave packet is mostly reflected by the barrier, while the transmitted component is suppressed. The corresponding animations are available online [127].

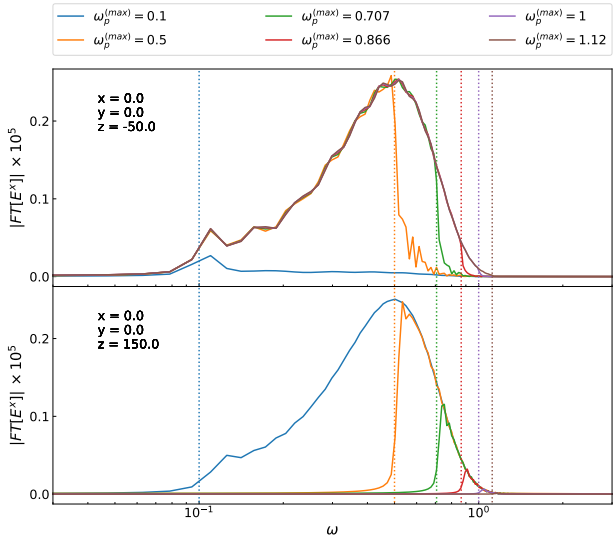

Figure 4.3. Absolute value of the discrete Fourier transform of E^x extracted before (upper panel) and after (lower panel) the plasma barrier. The different colors refer to the different values of the plasma density inside the barrier, and hence to different values of the plasma frequency $\omega_p^{(\max)}$, indicated with vertical dotted lines. We can clearly see that the barrier reflects the frequency components below $\omega_p^{(\max)}$, and transmits the components above it.

considered an initial wave packet of the electric field centered at $z_0 = -150$, with a width[4] $\sigma = 100$ and $\omega = 0.001$. We varied the amplitude of the EM field in a range $0.1 \leq A_E \leq 1000$. As for the plasma profile, we adopted a similar geometric model to the linear case, with the barrier placed between $z_1 = 100$ and $z_2 = 650$, with $W_1 = W_2 = 0.1$. We considered a background density $n_{\rm bkg} = 5 \times 10^{-6}$, and a maximum barrier density $n_{\max} = 0.5$, that corresponds to a plasma frequency of $\omega_p^{(\max)} = 0.022$. We used a numerical grid that extends in $[-2, 2] \times [-2, 2] \times [-750, 850]$, with a grid spacing $\Delta x = \Delta y = \Delta z = 0.2$, and a time step $\Delta t = 0.1$, so that CFL $= 0.5$. The final time of integration was set to $T = 500$.

The parameters were chosen such that the frequency of the wave packet was always much larger than $\omega_p^{(\rm bkg)}$, but a significant component of the spectrum, namely $\approx 97.5\%$, was below the plasma frequency of the barrier, and should therefore be reflected, if one assumes linear theory. First of all, we quantified the value of the electric field which gives rise to nonlinearities. A crucial parameter that characterizes the threshold of nonlinearities in laser-plasma interactions is the peak amplitude of the normalized vector potential, defined as $a_0 = e\mathbf{A}/m_e$ (see e.g. [269, 271]). Specifically, when $a_0 \gtrsim 1$, electrons acquire a relativistic transverse velocity, and therefore the interactions become nonlinear. Given our units, and estimating

rescaled by $[m_e]^{-1}$, while the electric field amplitude scales as $[m_e]^2$. Hence, the results of this section can be obtained in the case $m_e = 1$ by rescaling the other quantities accordingly.

[4]While formally the initial profile of the EM field, Eq. (4.33), represents a circularly polarized wave packet, the chosen value of the parameter σ reduces the y component of the electric field, making the polarization effectively elliptic.

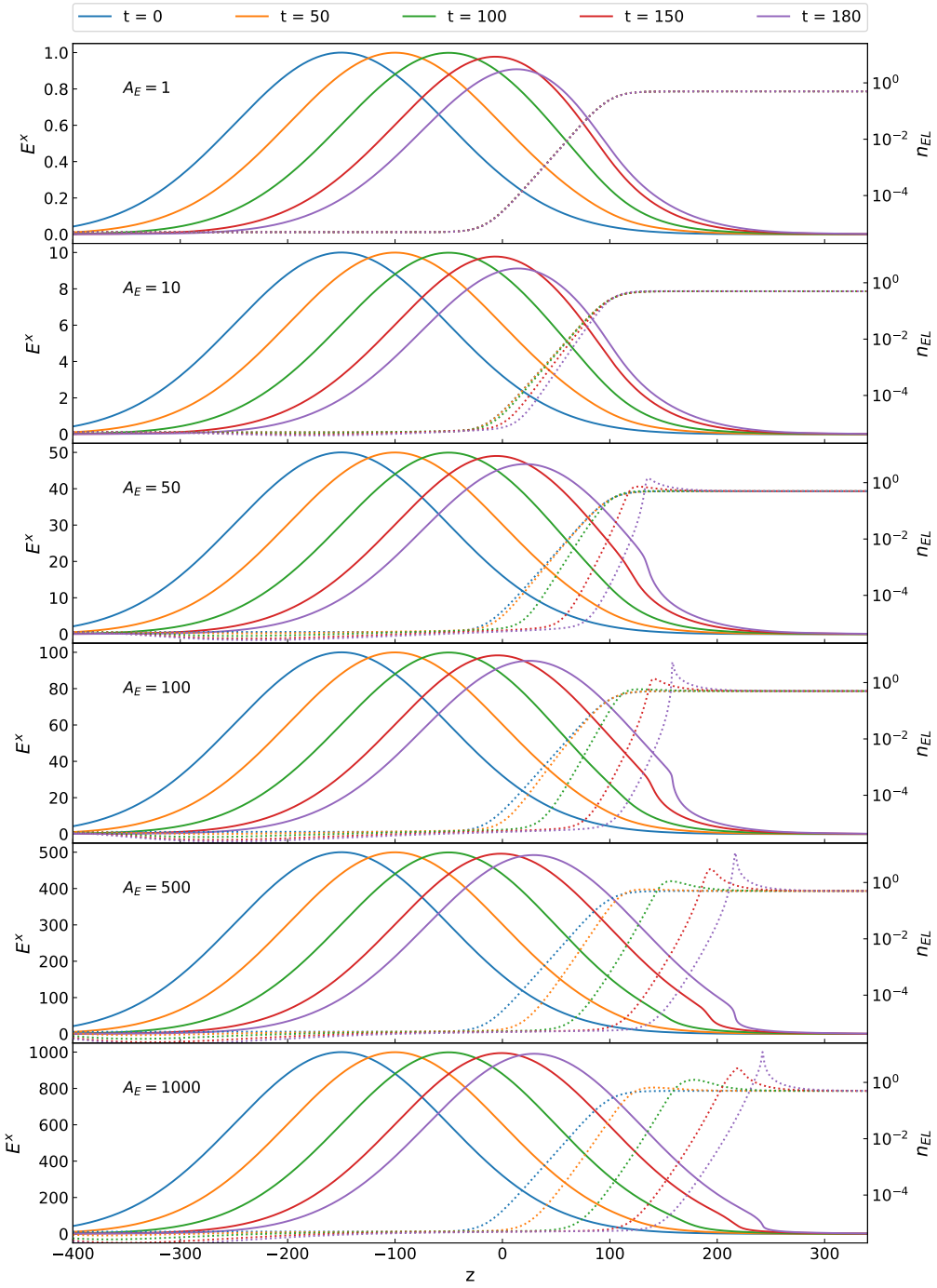

Figure 4.4. Snapshots of the evolution of E^x (solid lines) and n_{EL} (dotted lines) for the simulations of the propagation of an EM wave packet inside a plasma barrier in the nonlinear regime. The initial profile of n_{EL} is not varied across the simulations, and the different panels refer to different choices of the initial amplitude of the wave packet. The backreaction effects of the EM field onto the plasma density increase with A_E, and for $A_E \gtrsim 50$ the wave packet "transports" electrons along the z axis, eventually creating a plasma-depleted region (*blowout regime*). The corresponding animations are available online [127].

$A \approx E/\omega$, we obtained a critical electric field $E_{\rm crit} \gtrsim m_e\omega/e \approx 1$.

We performed a set of simulations choosing different values of the initial amplitude of the EM wave packet in the range $0.1 \leq A_E \leq 1000$. Figure 4.4 shows snapshots of the numerical simulations for some selected choices of A_E. It is possible to observe that in the case $A_E = 1$ (top panel) the density profile of plasma is not altered throughout the simulation, as in the linear case discussed in the previous section. Moreover, at sufficiently long times, the wave packet is reflected by the barrier, in agreement with linear theory predictions. From the second panel on (i.e. as $A_E \gtrsim 10$), instead, the wave packet induces a nonnegligible backreaction on the plasma density. This effect increases significantly for higher amplitudes, and it is due to the nonlinear couplings between transverse and longitudinal polarizations: the nonlinear Lorentz term $(\vec{\mathcal{U}} \times \vec{B})^z$ in the longitudinal component of the momentum equation (4.28) induces a radiation pressure on the plasma, and hence a longitudinal velocity $\vec{\mathcal{U}}^z$; as electrons travel along the z direction and ions remain at rest, a large longitudinal field due to charge separation is created, which tries to balance the effect of the Lorentz force and restore charge neutrality. This phenomenology resembles the one of plasma-based accelerators, where super-intense laser pulses are used to create large longitudinal fields that can be used to accelerate electrons [272].

To quantify the collective motion induced by nonlinearities we computed the velocity dispersion of electrons as

$$\sqrt{\langle \mathcal{U}^2 \rangle} = \sqrt{\frac{\int_V d^3x\, n_{EL}\, \mathcal{U}_i \mathcal{U}^i}{\int_V d^3x\, n_{EL}}}. \tag{4.34}$$

Since the fields are constant along the transverse directions[5], then $n_{EL}(x,y,z) = n_{EL}(z)$ and $\mathcal{U}^i(x,y,z) = \mathcal{U}^i(z)$. This allowed us to evaluate the above integral as

$$\sqrt{\langle \mathcal{U}^2 \rangle} = \sqrt{\frac{\int_{z_{-\infty}}^{z_{+\infty}} dz\, n_{EL}(z)\, \mathcal{U}_i(z) \mathcal{U}^i(z)}{\int_{z_{-\infty}}^{z_{+\infty}} dz\, n_{EL}(z)}}, \tag{4.35}$$

where $z_{\pm\infty}$ are the boundaries of the z domain and we computed the integral using the trapezoidal rule. In the upper panel of Fig. 4.5 we plotted the behavior of the velocity dispersion with respect to the initial amplitude A_E for different times. As we can see the nonlinearities start becoming relevant in the range $1 \lesssim A_E \lesssim 10$, where electrons start to acquire a collective motion. This is also confirmed by the middle panel, where the solid and dashed lines denote the maximum of $|\vec{\mathcal{U}}|$ and $\mathcal{U}^z$, respectively. While these quantities do not represent the collective behavior of the system, they have the advantage of not containing the contribution given by the portion of the plasma barrier that has not yet been reached by the EM wave. From this plot we can observe that in the range $1 \lesssim A_E \lesssim 10$, the electrons start acquiring a relativistic velocity with a large component on the transverse plane.

As already mentioned, the longitudinal motion of electrons generates a longitudinal field. Nevertheless, plasmas can sustain longitudinal fields only up to a certain threshold, usually called *wave-breaking (WB) limit*, above which plasma is not able to shield and sustain anymore electric fields, and the fluid description

[5] In Appendix I I show how the homogeneity of the fields along the transverse plane is preserved during the evolution.

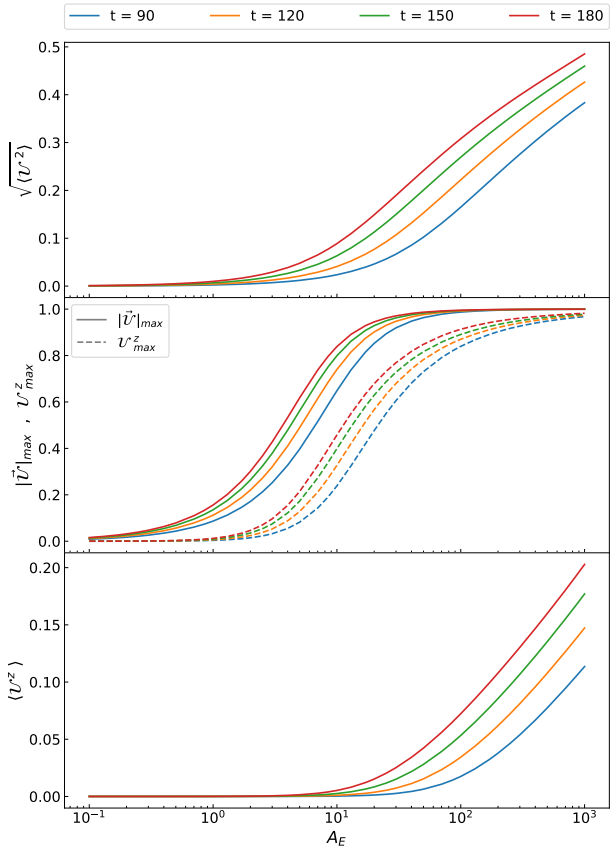

Figure 4.5. Collective behavior of plasma in the nonlinear regime as a function of the initial amplitude A_E of the EM wave packet. The upper panel shows the velocity dispersion $\sqrt{\langle \mathcal{U}^2 \rangle}$, the middle panel shows the maximum value of $|\vec{\mathcal{U}}|$ (solid lines) and of the longitudinal velocity $\mathcal{U}^z$ (dashed lines), while the lower panel shows the collective longitudinal velocity $\langle \mathcal{U}^z \rangle$. The nonlinearities start becoming relevant in the range $1 \lesssim A_E \lesssim 10$, where the velocity dispersion increases and the motion of electrons has a large component on the transverse plane. For $A_E \gtrsim 10$ the plasma enters in the blowout regime, where electrons are "transported" by the EM field, and acquire a positive collective longitudinal velocity.

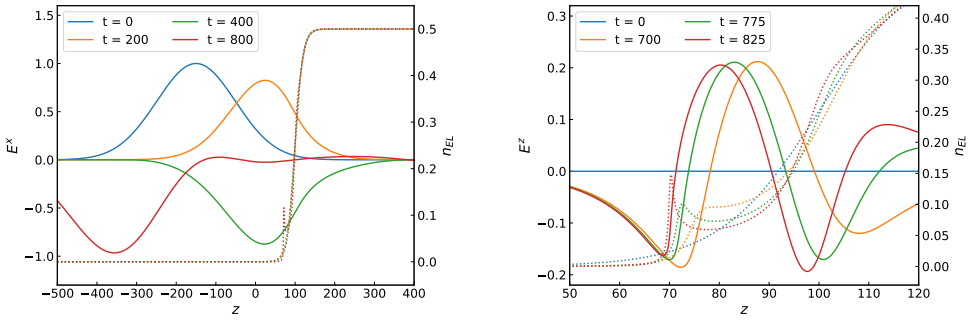

Figure 4.6. Evolution of the electric field and plasma density in the case of $A_E = 1$. Left panel: snapshots of E^x (solid lines) and n_{EL} (dotted lines) of the full evolution, where we can see that the wave packet is mostly reflected by the plasma barrier. Right panel: snapshots of the longitudinal component E^z (solid lines) and n_{EL} (dotted lines) focusing on the last stages of evolution. Here we can clearly see the WB phenomenon taking place, with the plasma density developing spikes in regions where the longitudinal component of the electric field increases steeply.

breaks down. This phenomenon was pioneered in [273] for the case of nonlinear, nonrelativistic cold plasmas, where the critical longitudinal field for WB was found to be $E^z_{\mathrm{WB}} = m_e\omega_p/e$, and later generalized for pulses with relativistic phase velocities [274]. This threshold field represents the limit after which the plasma response loses coherence as neighbouring electrons start crossing each other within one plasma frequency period. Therefore, above this critical electric field the plasma is not anymore able to coherently act as a system of coupled oscillators, and the fluid model based on collective effects breaks down. This leads to the formation of a spike in n_{EL}, which eventually diverges, and to a steepening of the longitudinal component of the electric field. Full particle-in-cell numerical simulations are required after the breakdown (see, e.g., [275, 276]). In our simulations, we observed the WB phenomenon at late times for large values of the electric field, in which cases we could only extract information before the breakdown of the model.

In order to better appreciate how the WB takes place, we repeated the simulation with $A_E = 1$ for a longer integration time and a larger grid. In the left panel of Fig. 4.6 I show the evolution of E^x (solid lines) throughout the simulation, where we can clearly see that the incoming wave packet is reflected by the plasma barrier. However, for $t \approx 700$, the longitudinal component of $\vec{\mathcal{U}}$ leads to an evolution of the plasma density. In this stage the plasma loses coherence and n_{EL} develops local spikes that increase in height and becomes sharper with time. When one of these spikes becomes excessively narrow, the fluid description of the system breaks down and the simulation crashes. This can be observed from the right panel of Fig. 4.6, where I show the longitudinal component of $\vec{E}$ together with the plasma density profile. Note that WB occurs as soon as the nonlinearities come into play (we observed it already for $A_E = 1$), and the fluid description in the nonlinear regime cannot be used for long-term numerical simulations. However the good convergence of the code even slightly before WB takes place (see Appendix H) ensures the reliability of the results up to this point.

Overall, Figs. 4.4 and 4.6 show that for $A_E \sim 1$ the system becomes weakly

nonlinear, in agreement with the previously mentioned analytical estimates.

Since we considered a model with vanishing pressure, it is worth examining the possibility that with the inclusion of a pressure term the formation of the observed spikes in n_{EL} can be contrasted. However, in order for the model to describe the regime of interest for the superradiant instability, the pressure has to be small [108, 109], and it has been shown that in a warm plasma the threshold for WB receives only small corrections with respect to the cold plasma case [277]. It is therefore to be expected that the WB phenomenon observed here would not be substantially altered by the inclusion of a pressure term.

Going back to the snapshots of the evolutions in Fig. 4.4, I now move to analyze the behavior of the system for larger electric fields, where the backreaction is macroscopic. We can see that in this case, i.e. for $A_E \gtrsim 50$, all the electrons in the plasma barrier are "transported" in the z direction and piled up within a plasma wake whose density grows over time. This corresponds to a *blowout regime* induced by radiation pressure. In order to better describe how the system reaches this phase, we computed the longitudinal component of the collective electron velocity as

$$\langle \mathcal{U}^z \rangle = \frac{\int_V d^3x\, n_{EL}\, \mathcal{U}^z}{\int_V d^3x\, n_{EL}} = \frac{\int_{z_{-\infty}}^{z_{+\infty}} dz\, n_{EL}(z)\, \mathcal{U}^z(z)}{\int_{z_{-\infty}}^{z_{+\infty}} dz\, n_{EL}(z)}, \tag{4.36}$$

where, again, we took advantage of the homogeneity of the system along the transverse directions to reduce the dimensionality of the domain of integration. The results are shown in the lower panel of Fig. 4.5, where we can see that for $A_E \lesssim 10$, the longitudinal momentum remains low and is not influenced by the wave packet. For $A_E \gtrsim 10$ instead, $\langle \mathcal{U}^z \rangle$ starts to increase in time, indicating that the system is in the blowout regime, as electrons are collectively moving forward in the z direction.

Overall, the above analysis shows that when the idealized situation studied in [111] cannot be applied and the nonlinear Lorentz term does not vanish, the general physical picture is drastically different and that penetration occurs in this setup due to radiation-pressure acceleration rather than transparency.

4.6 Discussion: implications for plasma-driven superradiant instabilities

Motivated by exploring the plasma-driven superradiant instability of accreting BHs at the full nonlinear level, we performed $3 + 1$ numerical simulations of a plane wave of very large amplitude but small frequency scattered off an inhomogeneous plasma barrier. Although nonlinear plasma-photon interactions are well studied in plasma-physics applications, to the best of our knowledge this is the first analysis aimed at exploring numerically this interesting setup in generic settings.

One of our main findings is the absence of the relativistic transparency effect in our simulations. As already mentioned, the analysis performed in [111] showed that, above a critical electric field, plasma turns from opaque to transparent, thus enabling the propagation of EM waves with frequency below the plasma one. As we have seen, such critical electric field for transparency is given by Eq. (4.6). In our simulations, we considered electric fields well above this threshold, yet we were not able to observe this effect. On the contrary, in the nonlinear regime the plasma

strongly interacts with the EM field in a complex way. The role of relativistic transparency in more realistic situations than the one described in [111] was rarely considered in the literature and is still an open problem [278]. Nevertheless, some subsequent analysis found a number of interesting features, and revealed that its phenomenology in realistic setups is more complex.

In Ref. [266] an analytical investigation of a similar setup was performed by considering the scattering between a laser wave packet and a sharp boundary plasma. The conclusion of the analysis is that, when plasma is inhomogeneous, nonlinearities tend to create a strong peaking of the plasma electron density (and hence of the effective plasma frequency), suppressing the laser penetration and enhancing the critical threshold needed for transparency. Subsequently, Refs. [267, 268] confirmed this prediction numerically, and showed that in a more realistic scenario transparency can occur but the phenomenology is drastically different from the one predicted in [111]. For nearly-critical plasmas, transparency arises due to the propagation of solitons, while for higher densities the penetration effect holds only for finite length scales. Nevertheless, these simulations were performed by considering a simplified momentum equation due to the assumption of a null-vorticity plasma, which is typically suitable for unidimensional problems, but likely fails to describe complex-geometry problems as the one of superradiant fields. Using particle-in-cell simulations, it was then realized that radiation-pressure can push and accelerate the fluid to relativistic regimes, similarly to our results, and produce interesting effects such as hole-boring, ion acceleration, and light-sail [279, 280].

While the complicated interplay between relativistic transparency and radiation-pressure acceleration is still an open problem [278, 281], we argue that the latter, which arises in generic situations with very overdense plasmas and high amplitude electric fields, is sufficient to dramatically quench the plasma-driven superradiant instability. To enforce this conclusion, we provided a rough estimate of the total energy extracted from the BH before nonlinear effects take place [110]. In order for the instability to be efficient on astrophysical timescales, $\omega \lesssim \omega_p \approx O(1/(GM))$, where G is the Newton's constant and M is the BH mass [108, 109, 264]. This gives a critical electric field

$$E_{\rm crit} = \frac{m_e \omega}{e} \approx 4 \times 10^5 \frac{\rm V}{\rm cm} \Big(\frac{M_\odot}{M} \Big). \tag{4.37}$$

The associated total energy can be estimated as $U = E_{\rm crit}^2 L^3$, where L is the size of the condensate formed by the superradiant instability, and corresponds to the location of the plasma barrier. This gives

$$U \approx 10^7 {\rm J} \Big(\frac{M}{M_\odot} \Big) \Big(\frac{L}{6M} \Big)^3 , \tag{4.38}$$

where we assumed that the peak of the plasma barrier roughly corresponds to the location of the peak density of an accretion disk, $L \approx 6M$. On the other hand, the total rotational energy of the BH is given by $K = MR^2\Omega^2$, where R and Ω are the radius and the angular velocity of the horizon, respectively. To efficiently satisfy the superradiant condition, $\Omega \gtrsim \omega_p \approx \mathcal{O}(1/(GM))$, so that

$$K \approx 10^{43} {\rm J} \Big(\frac{M}{M_\odot} \Big) . \tag{4.39}$$

Therefore, when the electric field reaches the threshold for nonlinearities, the total energy extracted from the BH is tiny, $U/K \approx 10^{-36}$.

Another argument supporting this conclusion is that, for the superradiant instability to be sustainable, the maximum energy leakage of the confining mechanism cannot exceed the superradiant amplification factor of the BH. For EM waves, the maximum amplification factor (for nearly extremal BHs and fine-tuned frequency) does not exceed $\approx 4\%$ and is typically much smaller [72]. Therefore, the instability is not quenched only if the plasma is able to confine more than 96% of the EM field energy. Our simulations show that in the nonlinear regime the situation is quite the opposite: almost the entirety of the EM field is not confined by the plasma, thus destroying its capability to ignite the instability. We expect this argument to be valid also when $\omega_p \gg \omega$, in which case plasma depletion through blowout is negligible, but the EM field can still transfer energy into longitudinal plasma motion.

Note that the arguments above are extremely conservative, since are based on a number of optimistic assumptions that would maximize the instability. First of all, realistic accretion flows around BHs are not spherical nor stationary, especially around spinning BHs. This would generically introduce mode-mixing and decoherence, rendering the instability less efficient. More importantly, even in the linear regime a disk-shape accretion geometry can (partially) confine modes that are mostly distributed along the equatorial plane, but would naturally provide energy leakage along off-equatorial directions [282, 283]. Finally, a sufficiently high plasma density in the corona could quench photon propagation in the first place [264], at least at the linear level during the early stages of the instability.

Chapter 5

Conclusions

In this thesis I have discussed three works in which my collaborators and I tackled conceptual problems by means of numerically simulated gedanken experiments.

In the work discussed in Chapter 2, we challenged the weak cosmic censorship conjecture in Einstein-Maxwell and in Einstein-Maxwell-scalar theories of gravity, by performing extensive fully nonlinear simulations of the spherical collapse of a charged field in different contexts, in the attempt of forming naked singularities.

In particular, we started by simulating the spherical collapse of a complex scalar field in flat spacetime in Einstein-Maxwell theory, trying to form a RN BH with $\bar{Q} > 1$. While we could form configurations with $\bar{Q} < 1$, and even very close to the upper bound, in situations that could have led to the formation of overcharged BHs the strength of the electromagnetic interaction was able to overcome gravitational attraction, preventing the collapse to naked singularities. This showed that, at least in our setup, WCCC is enforced by electric repulsion.

Also when starting from a pre-existing BH we were not able to produce naked singularities. While this is consistent with the theorem proven in Ref. [284], our analysis allowed us to identify the physical process that prevent the violation of WCCC. Specifically, we observed that the main role of cosmic censor is played by superradiance, that extracts energy and charge from the BH with the final effect of decreasing its charge-to-mass ratio. The analysis performed in this case gave us also the possibility of observing superradiant scattering at the fully nonlinear level (see Ref. [285] for a study specifically on this topic, and Ref. [286] for the rotating case).

Interestingly, the absence of formation of BH configurations with $\bar{Q} = 1$ in this second set of simulations, can also be viewed as a numerical confirmation of the third law of black hole thermodynamics, which states that it is impossible to convert a sub-extremal BH to an extremal one with a continuous process. Nevertheless, in a subsequent work Kehle and Unger [287], considering an Einstein-Maxwell model with a charged scalar field analogous to the one of our work, have shown the existence of a spherically symmetric spacetime configuration in which the third law is violated. While it might be hard to reproduce such configuration in a numerical simulation, the results of Ref. [287] show that it is conceptually possible to dinamically push the charge-to-mass ratio of a RN BH at least to $\bar{Q} = 1$.

In the case of Einstein-Maxwell-scalar we were able to dynamically form BHs with charge-to-mass ratio above unity, but still we did not produce naked singularities; however we observed that superradiance is at play also for scalarized BHs.

With our setup we could also study the descalarization in EMS gravity, which occurs when the charge-to-mass ratio of a scalarized BH decreases below the existence line, reaching a region where the RN solution is the only one allowed. We induced this process by simulating the absorption of an opposite-charged wave packet, but we also observed that it can take place with wave packets whose charge has the same sign as that of the BH, with the decrease in charge-to-mass ratio being driven by superradiance.

In the work described in Chapter 3 we simulated the collapse of a wave packet of a phantom field on a nearly-critical EdGB BH, with the purpose of investigating its evolution after Hawking evaporation. We observed that the system undergoes a runaway instability in which the horizon shrinks while the elliptic region inside the BH expands, until it gets exposed and the simulations has to be stopped. The behavior of the curvature hinted to the possibility of formation of a naked singularity, but the major problem to address was whether the dynamics of the elliptic region was gauge dependent or not. In fact at the time of writing the manuscripts in Refs. [43, 44] this was not yet clear, and one could still hope that in a different gauge the system of evolution equations was well-posed on the singularity, allowing to determine if a naked singularity formed.

However, in Ref. [288] the principal symbol of EdGB in spherical symmetry has been expressed in a gauge invariant way, meaning that the breakdown of hyperbolicity cannot be cured by a different gauge choice.

Nonetheless, given the good convergence of the code even close to the formation of a naked elliptic region, our simulations can be still useful as a knowledge base to analyze the same problem in other eventual alternative theories of gravity that present a minimum-mass solution. For instance, a research direction that my collaborators and I are interested in following, is the study of a modified version of EdGB in which the Einstein-Hilbert term is replaced by a $f(\mathcal{R})$ term. The idea is that a theory of this kind may still possess a minimum-mass BH, due to the presence of the Gauss-Bonnet term, but without suffering of problems related to hyperbolicity, thanks to the modifications in the principal symbol coming from the $f(\mathcal{R})$ term. In the case we will repeat a similar analysis also in the new model, it may be useful to compare the results with the EdGB case discussed here, as eventual differences or similarities can help in identifying the reasons that lead to the appearance of the observed behaviors.

Moreover, as we have seen, EdGB BHs coexist in the phase space with wormhole solutions. A possibility that we considered for EdGB gravity, but might be also taken into account for an eventual extension that preserves this characteristic, is that after losing mass critical BHs undergo a transition towards wormhole configurations, and the evaporation process is halted. Such a scenario can also have applications in the field of dark matter. Indeed horizonless remnants evade the constraints on light BHs [289] that arise from Hawking evaporation, and can in principle account for all the dark matter content of our Universe.

Lastly, in the work described in Chapter 4 we performed 3+1 nonlinear numerical simulations of the interaction between a high-amplitude, low-frequency EM wave packet and a plasma barrier, having in mind applications to the plasma-driven superradiant instability. We did not observe any signal of transparency, but the intense EM fields induced strong backreactions on the plasma, setting it in a blowout state in which electrons acquired a collective motion along the direction of propagation of the wave packet.

While the wave breaking phenomena that we encountered indicate that a particle-in-cell approach is required to perform simulations in the regime we explored, the dynamics appears to be complex, and a detailed model of plasma surrounding the BH is needed in order to draw definitive conclusions on whether nonlinear effects quench the superradiant instability. Nevertheless, our analysis already shows that plasma can be pushed severely out of equilibrium already in the first stages of the instability, and it is hard to imagine how a system in this state could sustain an exponential growth of the EM field.

As possible extensions to our work we could use the computational framework we developed to explore different scenarios, with a particular focus in beyond the Standard Model contexts. For instance, in Refs. [290,291] superradiance was studied in a model containing the ordinary photon and the dark photon, finding behaviors qualitatively similar to ours, with strong evolutions of the plasma profile. Therefore it would be interesting to study the propagation of the EM field in this regime using the techniques discussed here.

In conclusions, in these three works the use of gedanken experiments allowed us to tackle the problems at hand in a remarkably effective way. We could consider setups that were even markedly unrealistic, but in which the systems were explicitly pushed into the appropriate regimes to answer our questions, and the effects we would like to identify were forced to manifest. Furthermore, thanks to numerical simulations we could explore scenarios in which nonlinearities are relevant, and a semi-analytical approach would have been hardly viable. We could access extreme regimes in which the phenomenology is unknown, and by observing the evolution of the systems we simulated, we gained new insights on intrinsic aspects of the theories we examined.

The works I discussed in this thesis constitute only a small sample of the possible applications of numerically simulated gedanken experiments, and also thanks to the computational framework we developed, in the future it will be interesting to apply this research technique in many other contexts.

Appendix A

Null energy condition in EMS gravity with a complex scalar field

In this appendix I show that in the model (2.13) with a positive coupling function and in spherical symmetry, the null energy condition is always satisfied. To prove this statement I have to show that

$$T_{\mu\nu}m^\mu m^\nu \geq 0 \tag{A.1}$$

for any null vector m^μ, where $T_{\mu\nu}$ is the total energy-stress tensor. The latter is made of three terms, respectively due to the real scalar field ϕ, the complex scalar field ξ, and the electromagnetic field $F^{\mu\nu}$.

Let us consider these three terms separately. For two scalar fields one can show that

$$T^{\rm SF}_{\mu\nu}m^\mu m^\nu = \frac{1}{4\pi}\left(m^\mu\nabla_\mu\phi\right)^2 \geq 0\,, \tag{A.2}$$

$$T^{\xi}_{\mu\nu}m^\mu m^\nu = \frac{1}{2\pi}\left|m^\mu\mathcal{D}_\mu\xi\right|^2 \geq 0\,. \tag{A.3}$$

Finally, for the electromagnetic component we have

$$T^{\rm EM}_{\mu\nu}m^\mu m^\nu = -\frac{1}{4\pi}m^\mu F_{\mu\alpha}F^{\alpha}{}_{\nu}\,m^\nu F[\phi]. \tag{A.4}$$

Now, in spherical symmetry the magnetic field is absent and we can perform a 3+1 decomposition of the electromagnetic tensor as $F_{\mu\nu} = n_\mu E_\nu - n_\nu E_\mu$, where the electric field E^μ is orthogonal to n^μ (see Ref. [121]); therefore

$$\begin{aligned} T^{\rm EM}_{\mu\nu}m^\mu m^\nu &= -\frac{1}{4\pi}F[\phi]m^\mu m^\nu\left[E_\mu E_\nu - n_\mu n_\nu(E_jE^j)\right] \\ &= \frac{1}{4\pi}F[\phi]\left[(m_\mu n^\mu)^2(E_jE^j) - (m_iE^i)^2\right], \end{aligned} \tag{A.5}$$

Since m^μ is a null vector

$$0 = m_\mu m^\mu = m_\mu g^{\mu}{}_{\nu}m^\nu = m_\mu(\gamma^{\mu}{}_{\nu} - n^\mu n_\nu)m^\nu = m_im^i - (m_\mu n^\nu)^2, \tag{A.6}$$

and thus $(m_\mu n^\nu)^2 = m_i m^i$. Substituting in Eq. (A.5) we obtain that if $F[\phi] \geq 0$ then

$$T^{\rm EM}_{\mu\nu} m^\mu m^\nu = \frac{1}{4\pi} F[\phi]\left[m_i m^i (E_j E^j) - (m_i E^i)^2\right] \geq 0, \tag{A.7}$$

where in the last step the Cauchy-Schwarz inequality was used. Since the term $T_{\mu\nu} m^\mu m^\nu$ can be decomposed in a sum of three positive terms then the null energy condition (A.1) is satisfied.

Appendix B

Numerical evolution in EMS gravity with a complex scalar field: integration scheme and convergence tests

This appendix contains additional information on the numerical integration code used in the work described in Chapter 2. In particular I will discuss the implementation of the numerical integration scheme we used, and the convergence tests we performed to evaluate the reliability of the code.

B.1 Implementation of the PIRK integration scheme

Here, I summarize the PIRK integration scheme. The equations of motion are written as [124, 125]

$$\begin{cases} \partial_t u &= \mathcal{L}_1(u,v) \\ \partial_t v &= \mathcal{L}_2(u) + \mathcal{L}_3(u,v) \end{cases}, \tag{B.1}$$

where u schematically denotes the variables that are evolved fully explicitly whereas v the variables that are evolved partially implicitly.

We used an analogous procedure to Ref. [292]. Namely we first evolved explicitly the variables X, a, b, α, β^r, E^r, ξ and ϕ. As a second step we evolved partially implicitly A_a and K, using

$$\begin{cases} \mathcal{L}_{2(K)} &= -D^2\alpha, \\ \mathcal{L}_{3(K)} &= \beta^r\partial_r K + \alpha\Big(A_a^2 + 2A_b^2 + \frac{1}{3}K^2\Big) + 4\pi\alpha(S_a + 2S_b + \mathcal{E}) \end{cases}, \tag{B.2}$$

$$\begin{cases} \mathcal{L}_{2(A_a)} &= -\Big(D^r D_r\alpha - \frac{1}{3}D^2\alpha\Big) + \alpha(R^r{}_r - \frac{1}{3}R) \\ \mathcal{L}_{3(A_a)} &= \beta^r\partial_r A_a + \alpha K A_a - \frac{16\pi\alpha}{3}\Big(S_a - S_b\Big) \end{cases}, \tag{B.3}$$

Then, we evolved $\hat{\Delta}^r$, Π, P, a_r and φ using

$$\begin{cases} \mathcal{L}_{2(\hat{\Delta}^r)} & = \frac{2}{b}\partial_r\left(\frac{\beta^r}{r}\right) - 2\alpha(A_a - A_b)\frac{2}{br} - \frac{2}{a}(A_a\partial_r\alpha + \alpha\partial_r A_a) \\ & \quad + \frac{2\alpha}{a}\left[\partial_r A_a + (A_a - A_b)\left(\frac{\partial_r b}{b} + \frac{2}{r}\right) - 3A_a\frac{\partial_r X}{X} - \frac{2}{3}\partial_r K\right] \\ & \quad + \frac{1}{a}\partial_r^2\beta^r + \frac{\sigma}{3}\frac{1}{a}\partial_r\hat{\nabla}_m\beta^m \\ \mathcal{L}_{3(\hat{\Delta}^r)} & = \beta^r\partial_r\hat{\Delta}^r - \hat{\Delta}^r\partial_r\beta^r + 2\alpha A_a\hat{\Delta}^r + 2\frac{\sigma}{3}\hat{\Delta}^r\hat{\nabla}_m\beta^m - \frac{16\pi\alpha}{a}j_r \end{cases}, \tag{B.4}$$

$$\begin{cases} \mathcal{L}_{2(\Pi)} & = \frac{\alpha X^2}{a}\left[(\partial_r\phi)\left(\frac{2}{r} - \frac{\partial_r a}{2a} + \frac{\partial_r b}{b} - \frac{\partial_r X}{X}\right) + \partial_r^2\phi\right] + \frac{(\partial_r\phi)(\partial_r\alpha)}{a}X^2 \\ & \quad + \frac{1}{2}\frac{\alpha a}{X^2}(E^r)^2\frac{\delta F[\phi]}{\delta\phi} \\ \mathcal{L}_{3(\Pi)} & = \beta^r\partial_r\Pi + \alpha\Pi K \end{cases}, \tag{B.5}$$

$$\begin{cases} \mathcal{L}_{2(P)} & = \frac{\alpha X^2}{a}\left[(\partial_r\xi)\left(\frac{2}{r} - \frac{\partial_r a}{2a} + \frac{\partial_r b}{b} - \frac{\partial_r X}{X}\right) + \partial_r^2\xi\right] + \frac{(\partial_r\xi)(\partial_r\alpha)}{a}X^2 \\ & \quad + 2iq\alpha\left(\varphi P + \frac{a_r\partial_r\xi}{a}X^2\right) - q^2\alpha\left(\frac{(a_r)^2}{a}X^2 - \varphi^2\right)\xi \\ \mathcal{L}_{3(P)} & = \beta^r\partial_r P + \alpha P K \end{cases}, \tag{B.6}$$

$$\begin{cases} \mathcal{L}_{2(a_r)} & = a_r\partial_r\beta^r - \partial_r(\alpha\varphi) - \frac{\alpha a}{X^2}E^r \\ \mathcal{L}_{3(a_r)} & = \beta^r\partial_r a_r \end{cases}, \tag{B.7}$$

$$\begin{cases} \mathcal{L}_{2(\varphi)} & = -\frac{\alpha X^2}{a}\left[a_r\left(\frac{2}{r} - \frac{\partial_r a}{2a} + \frac{\partial_r b}{b} - \frac{\partial_r X}{X}\right) + \partial_r a_r\right] - \frac{(\partial_r\alpha)a_r}{a}X^2 \\ \mathcal{L}_{3(\varphi)} & = \beta^r\partial_r\varphi + \alpha\varphi K \end{cases}. \tag{B.8}$$

Finally, we evolved B^r fully implicitly.

B.2 Convergence tests

We checked the convergence of our code by computing the violation of the Hamiltonian constraint and studying its scaling with respect to the grid step.

We evolved the evolution equations using the initial condition discussed in Sec. 2.4.3, setting the initial BH charge-to-mass ratio to 0.9, and $qM = 5$. The grid extends from the origin up to $r_\infty = 250M$, and the grid steps we used are $\Delta r = 0.01M$ and $\Delta r = 0.005M$. In both cases the CFL factor was set to CFL $= 0.4$.

We then computed the violation of the Hamiltonian constraint at $T = 100M$, and the results are shown in Fig. B.1. As we can see from the plots, near the horizon the violation of the Hamiltonian constraint behaves as a third-order term, while in an outer region it scales as a second-order term, in agreement with the order of our numerical scheme.

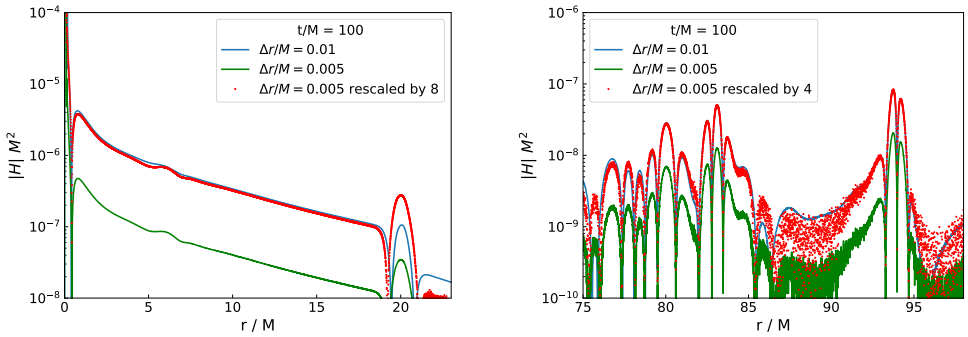

Figure B.1. Convergence of the code. Continuous lines denote the violation of the Hamiltonian constraint for the two spatial resolutions, while the dots denote the behavior corresponding to the higher resolution rescaled by the factor indicated in the legend. These plots show third-order convergence near the horizon, and second-order convergence in the outer region.

Appendix C

Field equations for stationary and spherically symmetric BHs in EdGB gravity

In this appendix I present the equations for stationary and spherically-symmetric BH solutions in EdGB gravity, both using Schwarzschild-like coordinates and PG-like coordinates. In both cases the dilaton and the metric functions depend only on the radial coordinate, so for them the primes denote radial derivatives. On the other hand for the coupling function $F'[\phi] = \frac{\delta F[\phi]}{\delta \phi}$.

C.1 Schwarzschild coordinates

Adopting the ansatz (3.7), the field equations (3.3),(3.4) read

$$\Lambda'\left(1+\frac{4}{\mathfrak{r}}F'[\phi]\phi'\right)-\frac{1-e^{\Lambda}}{\mathfrak{r}}-\frac{1}{2}\mathfrak{r}\phi'^2+\frac{4}{\mathfrak{r}}F'[\phi]\left[-3e^{-\Lambda}\Lambda'\phi'+2(e^{-\Lambda}-1)\phi''\right] + \frac{8}{\mathfrak{r}}F''[\phi]\phi'^2\left(e^{-\Lambda}-1\right)=0\,, \quad \text{(C.1)}$$

$$\Gamma'\left(1+\frac{4}{\mathfrak{r}}F'[\phi]\phi'\right)+\frac{1-e^{\Lambda}}{\mathfrak{r}}-\frac{1}{2}\mathfrak{r}\phi'^2-\frac{12}{\mathfrak{r}}e^{-\Lambda}\Gamma'F'[\phi]\phi'=0\,, \quad \text{(C.2)}$$

$$\Gamma''+\Gamma'\left(\frac{1}{\mathfrak{r}}+\frac{\Gamma'-\Lambda'}{2}\right)-\frac{\Lambda'}{\mathfrak{r}}+\phi'^2+\frac{4}{\mathfrak{r}}F'[\phi]\Big[\Gamma'\phi'e^{-\Lambda}\left(3\Lambda'-\Gamma'\right) - 2e^{-\Lambda}\left(\phi'\Gamma''+\Gamma'\phi''\right)\Big]-\frac{8}{\mathfrak{r}}e^{-\Lambda}F''[\phi]\phi'^2\Gamma'=0\,, \quad \text{(C.3)}$$

$$\phi''+\frac{\Gamma'-\Lambda'}{2}\phi'+\frac{2\phi'}{\mathfrak{r}}-\frac{2}{\mathfrak{r}^2}F'[\phi]\Big[\Gamma'\left(\Gamma'-\Lambda'+3e^{-\Lambda}\Lambda'-e^{-\Lambda}\Gamma'\right) + 2\Gamma''\left(1-e^{-\Lambda}\right)\Big]=0\,. \quad \text{(C.4)}$$

C.2 PG-like coordinates

After substituting the ansatz for the metric (3.28) in the field equations Eqs. (3.3)-(3.4), and performing algebraic manipulation using Wolfram MATHEMATICA it is possible to obtain the following system of ordinary differential equations:

$$\alpha' = \frac{\alpha}{4R'\left(RR' + 4\left(3\zeta^2-2\right)\phi' F'[\phi]\right)}\Big\{48\zeta^3 R'\zeta'\phi' F'[\phi] + 4\zeta R'\zeta'\left(RR' - 8\phi' F'[\phi]\right) + \zeta^2\left(R^2 R'\phi'^2 + 2R'^3\right) + R^2 R'\phi'^2 + 16\zeta^4\left(R'\phi'^2 F''[\phi] + F'[\phi]\left(R'\phi'' - R''\phi'\right)\right)\Big\}, \tag{C.5}$$

$$\zeta' = \frac{1}{4\zeta R'\left(RR' + 4\left(3\zeta^2-2\right)\phi' F'[\phi]\right)}\Big\{R^2 R'\phi'^2 - 16\zeta^4\Big[R'\phi'^2 F''[\phi] + F'[\phi]\left(R'\phi'' - R''\phi'\right)\Big] - \zeta^2\Big(16R''\phi' F'[\phi] + R'\Big(\phi'^2\left(R^2 - 16F''[\phi]\right) - 16\phi'' F'[\phi]\Big) + 2R'^3\Big)\Big\}, \tag{C.6}$$

$$\begin{aligned}\phi'' = -\frac{1}{D_\phi}\Big\{&\left(\zeta^2-1\right)R'^2\phi'\Big[\left(\zeta^2-1\right)F'[\phi]\phi'^3 - R'R''\Big]R^5 + R'\phi'\Big[\left(\zeta^2-2\right)R'^4 \\ &- 4\zeta^2\left(\zeta^2-1\right)\phi'^2 F''[\phi]R'^2 - 4\left(7\zeta^4 - 13\zeta^2 + 6\right)F'[\phi]\phi' R''R' \\ &- 8\left(\zeta^2-1\right)^2 F'[\phi]^2\phi'^4\Big]R^4 + 4R'F'[\phi]\phi'^2\Big[\left(12\zeta^4 - 25\zeta^2 + 12\right)R'^3 \\ &- 4\zeta^2\left(3\zeta^4 - 5\zeta^2 + 2\right)\phi'^2 F''[\phi]R' - 24\left(\zeta^2-1\right)^2\left(3\zeta^2-2\right)F'[\phi]\phi' R''\Big]R^3 \\ &- 32\left(\zeta^2-1\right)F'[\phi]^2\phi'^3\Big[6\left(\zeta^2-1\right)R'\phi'^2 F''[\phi]\zeta^4 + \left(-21\zeta^4 + 32\zeta^2 - 12\right)R'^3 \\ &+ 2\left(15\zeta^6 - 39\zeta^4 + 32\zeta^2 - 8\right)F'[\phi]\phi' R''\Big]R^2 + 4R'^2 F'[\phi]\Big[720F'[\phi]^2\phi'^4\zeta^8 \\ &- 24\phi'\left(94F'[\phi]^2\phi'^3 + R'^2 F''[\phi]\phi' - R'F'[\phi]R''\right)\zeta^6 + \Big(2624F'[\phi]^2\phi'^4 \\ &- 3R'\left(R'^3 - 8\phi'^2 F''[\phi]R' + 8F'[\phi]\phi' R''\right)\Big)\zeta^4 - 1344F'[\phi]^2\phi'^4\zeta^2 \\ &+ 256F'[\phi]^2\phi'^4\Big]R - 96\zeta^4\left(\zeta^2-1\right)R'^2 F'[\phi]^2\phi'\Big[R'^3 + 8\left(\zeta^2-1\right)\phi'^2 F''[\phi]R' \\ &- 8\left(\zeta^2-1\right)F'[\phi]\phi' R''\Big]\Big\},\end{aligned} \tag{C.7}$$

where

$$\begin{aligned}D_\phi = \left(\zeta^2-1\right)R'\Big[&96\left(3\zeta^4 - 5\zeta^2 + 2\right)R'F'[\phi]^2\phi'^2 R^3 \\ &+ 64\left(15\zeta^6 - 39\zeta^4 + 32\zeta^2 - 8\right)F'[\phi]^3\phi'^3 R^2 + R'^3\left(R^4 - 96\zeta^4 F'[\phi]^2\right)R \\ &+ 4R'^2 F'[\phi]\left(R^4\left(7\zeta^2 - 6\right) - 192\zeta^4\left(\zeta^2-1\right)F'[\phi]^2\right)\phi'\Big].\end{aligned} \tag{C.8}$$

The denominator D_ϕ vanishes at the horizon, since $\zeta = 1$. However the field equations are regular when the condition (3.30) is imposed. In this case ζ_h' and ϕ_h'' are given by

$$\phi_h'' = -\frac{3}{R_h^4 R_h'\left(R_h^4 - 96F'[\phi_h]^2\right) + 4R_h^7\phi_h' F'[\phi_h]}\Big[32R_h^4 R_h''\phi_h' F'[\phi_h]^2$$

$$+ 4R_h^5 R_h' R_h'' F'[\phi_h] + R_h^3 R_h'^2 \phi_h' \left(4R_h^2 F''[\phi_h] + R_h^4 - 32F'[\phi_h]^2\right)$$
$$+ 48R_h'^3 \left(R_h^2 F'[\phi_h] F''[\phi_h] + 4F'[\phi_h]^3\right)\Big], \tag{C.9}$$

$$\zeta_h' = -\frac{R_h'^2}{2R_h R_h' + 8\phi_h' F'[\phi_h]}. \tag{C.10}$$

Appendix D

Phase diagram in EdGB gravity: BHs, wormholes, and solitons

Here I present the methods used to find the static wormholes and the solitonic solutions with cusp singularities discussed in Sec. 3.1.3, and I discuss some of their properties [148–151]. Let me start with the wormhole solution. In spherical symmetry, the starting point is to consider the ansatz (3.7) in Schwarzschild coordinates. However, in this ansatz wormholes have a coordinate singularity, that can be removed defining the new coordinate $l^2 = \mathfrak{r}^2 - r_0^2$, where $l > 0$ and r_0 is the wormhole throat [148]. In terms of the coordinates (t, l, θ, φ), we used the following ansatz for the metric:

$$ds^2 = -e^{2\nu(l)}dt^2 + f(l)dl^2 + \left(l^2 + r_0^2\right)\left(d\theta^2 + \sin^2\theta\, d\varphi^2\right) . \tag{D.1}$$

Substituting into the modified Einstein equations (3.3)-(3.4), this yields

$$f' + \frac{f}{l\mathfrak{r}^2}\left(f\mathfrak{r}^2 - l^2 - 2\mathfrak{r}_0^2\right) - \frac{\mathfrak{r}^2}{2l}f\left(\phi'\right)^2 - \frac{4\gamma\lambda}{l\mathfrak{r}^2}e^{-\gamma\phi}\left[\frac{4l\mathfrak{r}_0^2}{r^2}\phi' + \left(\mathfrak{r}^2 - \frac{3l^2}{f}\right)f'\phi' + 2\gamma\phi'^2\left(\mathfrak{r}^2 f - l^2\right) + 2\phi''\left(l^2 - \mathfrak{r}^2 f\right)\right] = 0\,, \tag{D.2}$$

$$\nu' - \nu'\frac{4\gamma\lambda}{l}e^{-\gamma\phi}\left(1 - \frac{3l^2}{\mathfrak{r}^2 f}\right)\phi' + \frac{l}{2\mathfrak{r}^2} - \frac{f}{2l} - \frac{\mathfrak{r}^2}{4l}\phi'^2 = 0\,, \tag{D.3}$$

$$\nu'' + \nu'^2 + \nu'\left(\frac{l}{\mathfrak{r}^2} - \frac{f'}{2f}\right) - \frac{lf'}{2\mathfrak{r}^2 f} + \frac{\mathfrak{r}_0^2}{\mathfrak{r}^4} + \frac{1}{2}\phi'^2 + \frac{4\gamma\lambda}{\mathfrak{r}^2 f}e^{-\gamma\phi}\left[2l\phi'\nu'' + 2l\nu'\phi'' + \left(\frac{2\mathfrak{r}_0^2}{\mathfrak{r}^2} - 3\frac{lf'}{f} + 2l\nu' - 2l\gamma\phi'\right)\nu'\phi'\right] = 0\,, \tag{D.4}$$

$$\phi'' + \nu'\phi' + \left(\frac{2l}{\mathfrak{r}^2} - \frac{f'}{2f}\right)\phi' + \frac{4e^{-\gamma\phi}\gamma\lambda}{\mathfrak{r}^2 f}\left[-4\frac{l\mathfrak{r}_0^2}{\mathfrak{r}^4}\nu' + 2\left(f - \frac{l^2}{\mathfrak{r}^2}\right)\nu''\right.$$
$$\left. + \left(\frac{3l^2}{\mathfrak{r}^2 f} - 1\right) f'\nu' + \left(2f - \frac{2l^2}{\mathfrak{r}^2}\right)\nu'^2\right] = 0\,. \quad \text{(D.5)}$$

To impose the boundary conditions, we first expanded the dilaton and the metric functions at the throat (i.e., near $l \sim 0$):

$$\begin{aligned} f(l) &= f_0 + f_1 l + \mathcal{O}(l^2)\,, \\ e^{2\nu(l)} &= e^{2\nu_0}\,(1 + \nu_1 l) + \mathcal{O}(l^2)\,, \\ \phi(l) &= \phi_0 + \phi_1 l + \mathcal{O}(l^2)\,, \end{aligned} \quad \text{(D.6)}$$

where the parameters (f_1, ν_1, ϕ_1) are functions of (f_0, ν_0, ϕ_0) [148, 149]. At spatial infinity, we required:

$$\begin{aligned} f(l) &= 1 + \frac{2M}{l} + \mathcal{O}(l^{-2}) \\ \nu(l) &= -\frac{M}{l} + \mathcal{O}(l^{-2}) \\ \phi(l) &= -\frac{D}{l} + \mathcal{O}(l^{-2}) \end{aligned} \quad \text{(D.7)}$$

where M and D are the mass and scalar charge of the wormhole as measured by an observer at infinity. To obtain the wormhole solutions, we integrated Eqs. (D.2)–(D.5) from the throat at $l = 0$ outward, imposing Eqs. (D.6) as initial conditions. The parameter ν_0 was fixed though a rescaling by requiring asymptotic flatness of the metric, while ϕ_0 was fixed through a shooting procedure such that the dilaton field at infinity vanishes as in Eq. (D.7). We used units such that $r_0 = 2$. In this case the dimensionality of the parameter space is larger than for BHs: for each value of λ there exists a one-parameter family identified by f_0. This yields a two-dimensional domain of existence, see Fig. 3.4.

In particular, for $\lambda < 0.015228$ in the limit $f_0 \to 1$ we obtained wormhole solutions that coexist with BH solutions, as can be seen from the inset of Fig. 3.4. For $\lambda = 0.015228$ and $f_0 \to 1$ the wormhole solutions coexist with the singular BH at the end of the unstable branch. For $\lambda > 0.015228$ we found $f_0 > 1$ for all wormhole solutions. In particular, at the minimum value of f_0 allowed for these families, the wormhole solutions coexist with asymptotically flat and horizonless solutions, characterized by a singularity in the second radial derivative of the dilaton field. These "cusp" solutions also bound the domain of existence of horizonless, particle-like solutions whose scalar field diverges at the origin [150, 151].

The coordinates in Eq. (D.1) cover only part of the spacetime. If we try to extend them to values $l < 0$, we find a curvature singularity [149]. An interesting feature of these wormhole solutions is that this singularity disappears if we consider the existence of matter at the throat, as discussed extensively in [149].

Appendix E

Evolution equations for EdGB gravity with an additional phantom field

Here I discuss the system of equations used in the time evolution code described in Sec. 3.4. At variance with the cases discussed in Appendix C here the scalar fields and the metric functions depend on (r, t).

The evolution equations for the scalar fields have been obtained from the definition of the conjugate momenta (Eq. (3.37)) and are:

$$\partial_t \phi = \alpha P + \frac{\alpha \zeta Q}{R'}, \tag{E.1}$$

$$\partial_t \xi = \alpha \Pi + \frac{\alpha \zeta \Theta}{R'}. \tag{E.2}$$

Note that I am using a prime to indicate differentiation with respect to the single variable of a function, while I am using ∂_r and ∂_t to denote partial differentiation of spacetime variables. The evolution equations for Q and Θ are obtained by performing the time derivative of their definitions, and substituting the radial derivatives of Eqs. (E.1),(E.2) in place of the mixed derivatives of the scalar fields. The result is

$$\partial_t Q = \partial_r \Big(\alpha P + \frac{\alpha \zeta Q}{R'} \Big), \tag{E.3}$$

$$\partial_t \Theta = \partial_r \Big(\alpha \Pi + \frac{\alpha \zeta \Theta}{R'} \Big). \tag{E.4}$$

Finally, using the field equations it is possible to obtain three evolution equations for P, Π, and ζ and two constraints for α and ζ. The evolution equations are

$$\begin{aligned}
\partial_t P = \frac{1}{D_P} \Big\{ & \alpha R'^2 \Big[Q \left(R'(\partial_r \alpha) - \alpha R'' \right) + R' \Big(P \zeta R' (\partial_r \alpha) + \alpha \big((\partial_r Q) \\
& + R' \left(\zeta (\partial_r P) + P (\partial_r \zeta) \right) \big) \Big) \Big] R^4 - 2 \alpha R' \Big[2 F'[\phi] \Big(\Big(\zeta^2 + 4 \Big) R' (\partial_r \alpha) \\
& + \alpha \left(\zeta R' (\partial_r \zeta) - 4 R'' \right) \Big) Q^2 + R' \Big(20 P \zeta R' F'[\phi] (\partial_r \alpha) + \alpha \big(- R'^2
\end{aligned}$$

$$
\begin{aligned}
&+ 4F'[\phi]\left(2\zeta(\partial_r P) + 3P(\partial_r\zeta)\right)R' + 8F'[\phi]\left((\partial_r Q) - P\zeta R''\right)\Big)\Big)Q \\
&+ R'\Big(10P^2\zeta F'[\phi](\zeta(\partial_r\alpha) + \alpha(\partial_r\zeta))R'^2 + P\alpha\zeta(-R'^2 + 8\zeta F'[\phi](\partial_r P)R' \\
&+ 8F'[\phi](\partial_r Q))R' - 2(2\Theta\Pi R' + \zeta\left(\Theta^2 + \Pi^2 R'^2\right))F'[\phi]\left(\zeta(\partial_r\alpha) + \alpha(\partial_r\zeta)\right)\Big)\Big]R^3 \\
&- 2\alpha F'[\phi]\Big[8\alpha\zeta^2 R'F''[\phi]Q^4 - 8\Big(2\left(\zeta^2+2\right)R'F'[\phi](\partial_r\alpha) + \alpha(F'[\phi](\left(\zeta^2-4\right)R'' \\
&+ 2\zeta R'(\partial_r\zeta)) - 2P\zeta R'^2F''[\phi]\Big)\Big)Q^3 + R'\Big(\alpha\Big(\Big(\left(8\left(P^2-\Pi^2\right)F''[\phi] - 3\right)\zeta^2 \\
&+ 16\Big)R'^2 + 8\big(-2\zeta\left(\Theta\Pi F''[\phi] + 2F'[\phi](\partial_r P)\right) - P\left(\zeta^2+8\right)F'[\phi](\partial_r\zeta)\big)R' \\
&- 8\zeta(\zeta\Theta^2F''[\phi] - 6PF'[\phi]R'') + 8\left(\zeta^2-4\right)F'[\phi](\partial_r Q)\Big) \\
&- 8P\zeta\left(\zeta^2+16\right)R'F'[\phi](\partial_r\alpha)\Big)Q^2 + 2\Big(P\alpha\zeta(15R'^2 - 32\zeta F'[\phi](\partial_r P)R' \\
&- 24F'[\phi](\partial_r Q))R'^2 + 4(2\Theta\Pi R' + \zeta\left(\Theta^2 + \Pi^2R'^2\right))F'[\phi](2\zeta R'(\partial_r\alpha) \\
&+ \alpha\left(\zeta R'' + 2R'(\partial_r\zeta)\right)) - 4P^2\zeta F'[\phi](16\zeta R'(\partial_r\alpha) - 3\alpha\left(\zeta R'' - 4R'(\partial_r\zeta)\right))R'^2\Big)Q \\
&+ \zeta R'\Big(8R'(\partial_r\alpha)(P\zeta(2\Theta\Pi R' + \zeta\left(\Theta^2 + \left(\Pi^2 - 5P^2\right)R'^2\right))F'[\phi] + R'(\partial_r\zeta)) \\
&+ \alpha(-32P^2\zeta^2F'[\phi](\partial_r P)R'^3 + 2\Theta\Pi(R'^2 + 8PF'[\phi](\partial_r\zeta)R' - 8F'[\phi](\partial_r Q))R' \\
&+ \zeta(17P^2R'^4 - \Pi^2R'^4 + 3\Theta^2R'^2 - 24P^2F'[\phi](\partial_r Q)R'^2 - 8\Pi^2F'[\phi](\partial_r Q)R'^2 \\
&+ 8P(\Theta^2 + \left(\Pi^2 - 5P^2\right)R'^2)F'[\phi](\partial_r\zeta)R' - 8\Theta^2F'[\phi](\partial_r Q))\Big)\Big]R^2 \\
&- 8R'F'[\phi]\Big[4\alpha^2\left(\zeta^2-4\right)R'F'[\phi]Q^3 + 4\alpha\zeta R'(P\alpha\left(\zeta^2-12\right)R'F'[\phi] \\
&+ 2\zeta F''[\phi](\partial_r\alpha))Q^2 + 4\zeta\Big(2R'F'[\phi](\partial_r\alpha)^2\zeta^3 + \alpha^2R'(2F'[\phi](\partial_r\zeta)^2 \\
&+ 2PR'F''[\phi](\partial_r\zeta) - \left(\Theta^2 + \left(13P^2 - \Pi^2\right)R'^2\right)F'[\phi])\zeta \\
&+ 2\alpha(\partial_r\alpha)\Big(\zeta(3P\zeta R'^2F''[\phi] - F'[\phi]R'') + 2\left(\zeta^2-2\right)R'F'[\phi](\partial_r\zeta)\Big)\Big)Q \\
&+ \zeta^2R'\Big(-20P^3\alpha^2\zeta F'[\phi]R'^3 + 16P^2\alpha\zeta F''[\phi](\zeta(\partial_r\alpha) \\
&+ \alpha(\partial_r\zeta))R'^2 + 4PF'[\phi](\zeta\left(\left(\Pi^2R'^2 - \Theta^2\right)\alpha^2 + 2(\partial_r\alpha)^2\right) - 6\alpha(\partial_r\alpha)(\partial_r\zeta))R' \\
&+ \alpha((R'(\left(2\zeta^2-1\right)R' + 8\zeta\left(3-2\zeta^2\right)F'[\phi](\partial_r P)) + 8F'[\phi](\partial_r Q))(\partial_r\alpha) \\
&+ 2\alpha R'(\zeta R' + 4\left(1-2\zeta^2\right)F'[\phi](\partial_r P))(\partial_r\zeta))\Big)\Big]R \\
&+ 4\zeta F'[\phi]\Big[\zeta\Big(64QR'\left(2Q + P\zeta R'\right)F'[\phi]^2(\partial_r\zeta)^2 + 8F'[\phi](-8\zeta R'F''[\phi]Q^3 \\
&+ 8\left(2PF''[\phi]R'^2 + \zeta F'[\phi]R''\right)Q^2 + R'(R'(5\zeta R'\left(8F''[\phi]P^2 + 1\right) \\
&+ 16\left(1-2\zeta^2\right)F'[\phi](\partial_r P)) - 8\zeta F'[\phi](\partial_r Q))Q + P\zeta R'^3(3\zeta R'\left(8F''[\phi]P^2 + 1\right) \\
&+ 8\left(1-3\zeta^2\right)F'[\phi](\partial_r P)))(\partial_r\zeta) + \zeta R'(8\zeta R'F''[\phi]P^2 + 8QF''[\phi]P + \zeta R' \\
&- 8\left(\zeta^2-1\right)F'[\phi](\partial_r P))(R'^3 - 8\left(F''[\phi]Q^2 + F'[\phi](\partial_r Q)\right)R' \\
&+ 8QF'[\phi]R'')\Big)\alpha^2 + 8F'[\phi](\partial_r\alpha)\Big(16\zeta R'F''[\phi]Q^3 + 16\Big(\zeta(4P\zeta R'^2F''[\phi]
\end{aligned}
$$

$$
\begin{aligned}
&- F'[\phi]R'') + 2\left(\zeta^2-1\right)R'F'[\phi](\partial_r\zeta)\Big)Q^2 + 2\zeta R'\Big(\Big(\zeta^2\left(36F''[\phi]P^2+2\right)-1\Big)R'^2\\
&+ 4F'[\phi]\left(2\zeta\left(3-2\zeta^2\right)(\partial_r P) + 3P\left(\zeta^2-2\right)(\partial_r\zeta)\right)R'\\
&+ 8F'[\phi]\left((\partial_r Q) - P\zeta R''\right))Q + P\zeta^2 R'^2\Big(\Big(3\zeta^2\left(8F''[\phi]P^2+1\right)-2\Big)R'^2\\
&- 8F'[\phi]\left(\zeta\left(3\zeta^2-5\right)(\partial_r P) + 2P(\partial_r\zeta)\right)R' + 16F'[\phi](\partial_r Q)\Big)\Big)\alpha\\
&+ 128\zeta^2 R'\left(Q\zeta+PR'\right)\left(Q+P\zeta R'\right)F'[\phi]^2(\partial_r\alpha)^2\Big]\Big\}, \qquad \text{(E.5)}
\end{aligned}
$$

$$
\begin{aligned}
\partial_t\Pi = \frac{1}{RR'^3}\Big\{&RR'(\partial_r\alpha)\left(R'\zeta\Pi+\Theta\right) + \alpha\big[R'\big(R\left(R'(\partial_r\zeta)\Pi + (\partial_r\Theta)\right)\\
&+ R'\zeta\left(2R'\Pi + R(\partial_r\Pi)\right)\big) + \Theta\left(2R'^2 - RR''\right)\big]\Big\}, \qquad \text{(E.6)}
\end{aligned}
$$

$$
\begin{aligned}
\partial_t\zeta = \frac{1}{4R'\zeta\left(8F'[\phi]\left(R'P\zeta+Q\right)-RR'\right)}\Big\{&2\zeta^2\Big[\alpha\Big(8(\partial_r\zeta)F'[\phi]\left(2R'P\zeta+Q\right)\\
&+ R'\left(-8R'P^2\zeta F''[\phi] - R'\zeta - 8PQF''[\phi] + 8(\partial_r P)\left(\zeta^2-1\right)F'[\phi]\right)\Big)\\
&- 8R'^2(\partial_t P)\zeta F'[\phi]\Big] + R^2\alpha\big(2R'(\Theta\Pi - PQ) + R'^2\zeta\left(\Pi^2-P^2\right)\\
&+ \zeta\left(\Theta^2-Q^2\right)\big) - 4RR'\alpha\zeta^2(\partial_r\zeta)\Big\}, \qquad \text{(E.7)}
\end{aligned}
$$

where

$$
\begin{aligned}
D_P = R'^2\Big[&\alpha R'^3R^4 - 16\alpha R'^2\left(Q+P\zeta R'\right)F'[\phi]R^3 + 64\alpha R'\left(Q+P\zeta R'\right)^2F'[\phi]^2R^2\\
&+ 128\zeta^3R'^2F'[\phi]^2\left(\zeta(\partial_r\alpha)+\alpha(\partial_r\zeta)\right)R - 32\zeta^3F'[\phi]^2\Big(8\zeta R'(4Q\\
&+ 3P\zeta R')F'[\phi](\partial_r\alpha) + \alpha(\zeta\left(R'^3 - 8\left(F''[\phi]Q^2 + F'[\phi](\partial_r Q)\right)R' + 8QF'[\phi]R''\right)\\
&+ 8R'\left(4Q+3P\zeta R'\right)F'[\phi](\partial_r\zeta))\Big)\Big]. \qquad \text{(E.8)}
\end{aligned}
$$

The constraints are

$$
\begin{aligned}
\partial_r\zeta = -&\frac{1}{4R'\zeta\left(RR'-8F'[\phi]\left(R'P\zeta+Q\right)\right)\left(RR'-4F'[\phi]\left(3R'P\zeta+2Q\right)\right)}\\
&\times\Big\{8R'^2\zeta^2F'[\phi](R'P+Q\zeta)\Big[R^2(PQ-\Theta\Pi) + 8\zeta^2\left(PQF''[\phi] + (\partial_r P)F'[\phi]\right)\Big]\\
&- \Big[4F'[\phi]\left(Q\left(\zeta^2-2\right) - 2R'P\zeta\right) + RR'\Big]\Big[R^2R'\Big(2R'\zeta(PQ-\Theta\Pi)\\
&+ R'^2\left(P^2-\Pi^2\right) + Q^2 - \Theta^2\Big) + 2\zeta^2\Big(R'(8R'\zeta\left(PQF''[\phi] + (\partial_r P)F'[\phi]\right)\\
&+ 8Q^2F''[\phi] + 8(\partial_r Q)F'[\phi] - R'^2) - 8R''QF'[\phi]\Big)\Big]\Big\}, \qquad \text{(E.9)}\\
\partial_r\alpha = &\frac{\alpha}{2R'\zeta\left(RR'-8F'[\phi]\left(R'P\zeta+Q\right)\right)\left(RR'-4F'[\phi]\left(3R'P\zeta+2Q\right)\right)}\\
&\times\Big\{2R^2R'F'[\phi]\Big[R'^2\zeta(5P^2Q - 6P\Theta\Pi + Q\Pi^2) + 4R'Q(PQ-\Theta\Pi)\\
&+ Q\zeta\left(\Theta^2-Q^2\right)\Big] - 8RR'^3\zeta^2\Big(PQF''[\phi] + (\partial_r P)F'[\phi]\Big) + R^3R'^3(\Theta\Pi - PQ)\\
&+ 4\zeta^2F'[\phi]\Big[-8R'Q^3\zeta F''[\phi] + 24R'^3P(\partial_r P)\zeta F'[\phi] + R'Q\Big(16R'(\partial_r P)F'[\phi]
\end{aligned}
$$

$$+\zeta\left(R'^2\left(24P^2F''[\phi]+1\right)-8(\partial_r Q)F'[\phi]\right)\right)$$
$$+8Q^2\left(R''\zeta F'[\phi]+2R'^2PF''[\phi]\right)\Big]\Big\}. \tag{E.10}$$

These equations have been derived using Wolfram MATHEMATICA.

Appendix F

Numerical evolution in EdGB gravity: code testing and convergence

Here I discuss the simulations we performed to test the accuracy of the integration algorithm.

We first evolved a static BH in the upper branch ($\gamma = 4$, $\lambda = 0.01536$) in absence of perturbations of both scalar fields ($A_\phi = A_\xi = 0$). The outer boundary was placed at $R_\infty = 520$, the final time was $T = 500$, and the CFL factor was set to CFL $= 0.025$.

In Fig. F.1 I show how the violation CV_ζ of the constraint (E.9) at $t = T$ scales with the resolution. As we can see the fourth-order scaling is not satisfied in all the radial domain. This can be due to the fact that CV_ζ assumes small values and is dominated by noise. However, as we can see from the insets, the constraint violation scales as a fourth-order term in Δr in the horizon region, and as a fifth-order term in the region $3 \lesssim R \lesssim 6$. While the behavior near the horizon is consistent with the accuracy of the evolution algorithm, the fifth-order scaling might be due to the Kreiss-Oliger dissipation term, which is of order 5 in Δr.

Moreover, we observed that the profile of the dilaton field remains constant in time, which is consistent with the fact that our starting configuration is a static solution to the field equations.

In order to corroborate the reliability of the integration algorithm in the region in which the constraint violation is dominated by noise, we used a second-order accurate version of the code. In this way CV_ζ is typically larger, allowing us to check its scaling properties above the noise floor. The modifications introduced alter as little as possible the structure of the integration algorithm and they can be summarized as follows:

- We used the second-order Runge-Kutta method for the time integration;
- We used the second-order accurate finite differences method for the radial derivatives; we continued using the (second-order) upwind scheme for the first 2 grid points (instead of 1);

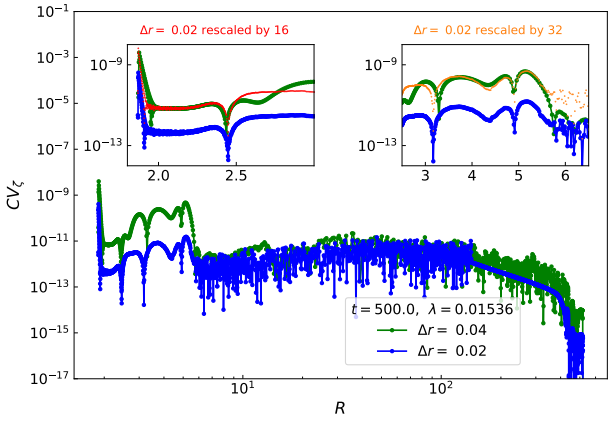

Figure F.1. Scaling of the violation CV_ζ of the constraint (E.9), at the end of the evolution of a stable static dilatonic BH configuration. We can see a fourth-order scaling near the horizon and a fifth order scaling for $3 \lesssim R \lesssim 6$.

- We performed the integration of the constraint for α using only the trapezoidal rule;
- We performed the integration in the shooting procedure and in the initialization part with the second-order accurate Runge-Kutta method;
- We computed the numerical derivatives in the right-hand side of the constraints during the initialization part with second-order accuracy; however the resolution of the shooting procedure was still the double of the resolution in the evolution (half of the grid points were discarded after initialization);
- We used the third order Kreiss-Oliger dissipation term

$$Q\,u = -\frac{\eta_{\rm KO}}{16\,\Delta t}(\Delta r)^4 (D_+^2)\rho(D_-^2)u, \tag{F.1}$$

  where u is a generic field, $\eta_{\rm KO} = 0.05$, and

$$\rho = \frac{1}{1+e^{5(R-15)}}; \tag{F.2}$$

  we continued excluding the innermost and outermost 3 grid points from the computation of the dissipation term (instead of 2);
- We used CFL $= 0.01$ since we observed that when using the second-order accurate code a lower CFL was needed.

We performed the numerical evolution of the same initial configuration as before with this version of the code. In Fig. F.2 I show the scaling of the constraint violation at the end of the simulations with resolutions $\Delta r = 0.005$ and $\Delta r = 0.01$. In this case we obtained the expected second-order scaling in all the radial domain except in a small region around $R \sim 15$ where CV_ζ seems to scale as a third order term. This may be due to the Kreiss-Oliger dissipation term, which is of order 3.

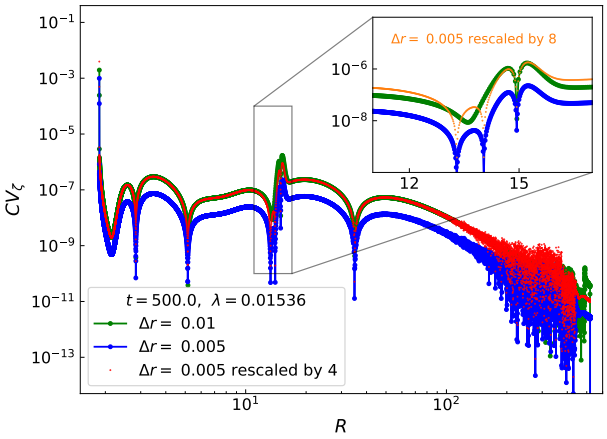

Figure F.2. Scaling of the constraint violation at the last time step of the evolution of a static stable dilatonic BH with $\lambda = 0.01536$ using the second-order accurate code. In this case CV_ζ scales as a second-order term, except in a region around $R \sim 15$, where there is third order scaling. This behavior may be due to the presence of the Kreiss-Oliger dissipation term.

We then moved to consider some collapsing scenarios in order to test the behavior of our second- and fourth-order accurate codes in the dynamical setups of our interest. We first considered the collapse of a wave packet of the dilaton on a Schwarzschild BH in GR ($\lambda = 0$). In this case we could estimate the BH mass at the horizon as $M_h = \frac{R_h}{2}$, and we could compare it with the Misner-Sharp mass at infinity to check that the results of the numerical evolution were in agreement with physical expectations. We obtained that initially $M_h < M_{\rm MS}$ since part of the total mass in the spacetime is stored in the profile of the dilaton outside the horizon, while at the end $M_h = M_{\rm MS}$ with excellent accuracy. This is consistent with the fact that the pulse of the dilaton has been absorbed by the BH.

We then considered a wave packet of the phantom field instead of the dilaton. In this case $M_h > M_{\rm MS}$ at the beginning of the simulation since the profile of the phantom field outside the BH adds a negative contribution to the total Misner-Sharp mass. At the end of the simulation instead, $M_h = M_{\rm MS}$. Also in this case the results of the simulations are consistent with physical expectations since the BH mass decreases upon absorbing the phantom perturbation.

We finally studied the convergence in some collapsing scenarios when $\lambda \neq 0$. I discuss here a test simulation of the collapse of a wave packet of the phantom field on a static dilatonic BH in the case $\lambda = 0.01528$. The outer boundary was at $R_\infty = 720$, the final time of integration was $T = 700$, and the parameters of the initial wave packet were

$$A_{0,\xi} = 0.02, \qquad R_{0,\xi} = 15, \qquad \sigma_\xi = 0.5. \tag{F.3}$$

In the left panel of Fig. F.3 I show the scaling of the constraint violation at the end of the numerical evolution. As we can see it is not possible to evaluate the convergence of the code since CV_ζ is very small and dominated by noise. However we repeated the simulation with the second-order accurate version of the code and

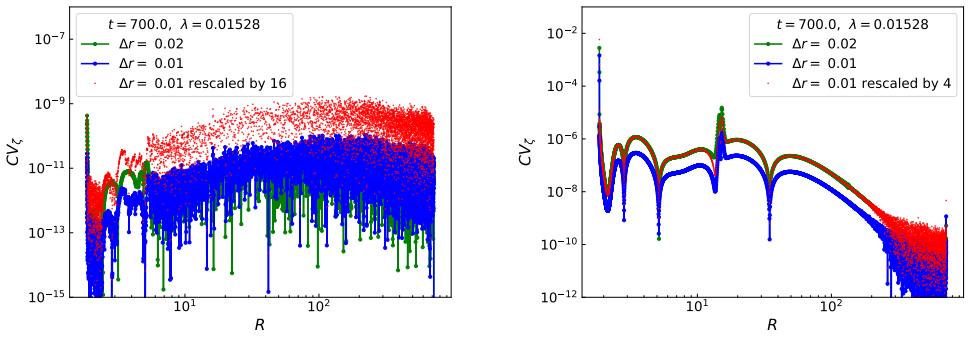

Figure F.3. Scaling of the constraint violation at the end of the simulation of the collapse of a wave packet of the phantom field on a dilatonic BH in the upper branch. The left and the right panels refer respectively to the fourth and the second-order accurate versions of the code.

we obtained the expected scaling properties (see the right panel of Fig. F.3)

In summary, even though it was not possible to evaluate properly the convergence of the code, the constraint violation appears to be very small and dominated by noise. The results of the test simulations are consistent with physical expectations, and the good scaling properties of the second-order accurate version of the code corroborate the reliability of our implementation of the integration algorithm that we used.

Appendix G

Derivation of the $3+1$ form of the equations for the plasma fluid

Here I report the explicit computation to express Eqs. (4.8), (4.9) in $3+1$ form.

G.1 Decomposition of Eq. (4.8)

Let me rewrite Eq. (4.8) for clarity:

$$u^\nu \nabla_\nu u^\mu = \frac{e}{m_e} F^{\mu\nu} u_\nu. \tag{G.1}$$

We have to project it separately on n^μ and on Σ_t.

Projection on n^μ

Contracting Eq. (4.8) with n_μ we obtain

$$n_\mu u^\nu \nabla_\nu u^\mu = \frac{e}{m_e} F^{\mu\nu} u_\nu n_\mu. \tag{G.2}$$

In the right hand side we have

$$\frac{e}{m_e} F^{\mu\nu} u_\nu n_\mu = -\frac{e}{m_e} E^\nu u_\nu = -\frac{e}{m_e} E^{\nu\ (3)} u_\nu, \tag{G.3}$$

where in the last step we used the fact that E^μ lies on Σ_t. The left hand side requires more manipulation. In particular we have that

$$n_\mu u^\nu \nabla_\nu u^\mu = u^\nu \nabla_\nu (n_\mu u^\mu) - u^\mu u^\nu \nabla_\nu n_\mu = -u^\nu \nabla_\nu \Gamma - u^\mu u^\nu \nabla_\nu n_\mu. \tag{G.4}$$

Let us now consider only the second term:

$$\begin{aligned} u^\mu u^\nu \nabla_\nu n_\mu &= u^\mu u^\nu \delta^\lambda{}_\nu \nabla_\lambda n_\mu = u^\mu u^\nu (h^\lambda{}_\nu - n^\lambda n_\nu) \nabla_\lambda n_\mu \\ &= u^\nu u^\mu h^\lambda{}_\nu \nabla_\lambda n_\mu - u^\nu n_\nu u^\mu a_\mu \end{aligned}$$

$$
\begin{aligned}
&= u^\nu u^\mu h^\lambda{}_\nu \delta^\sigma{}_\mu \nabla_\lambda n_\sigma + \Gamma u^\mu a_\mu \\
&= u^\nu u^\mu h^\lambda{}_\nu h^\sigma{}_\mu \nabla_\lambda n_\sigma - u^\nu u^\mu h^\lambda{}_\nu n^\sigma n_\mu \nabla_\lambda n_\sigma + \Gamma u^\mu a_\mu .
\end{aligned} \tag{G.5}
$$

Here we used the definition of the projection operator $h^\mu{}_\nu = \delta^\mu{}_\nu + n^\mu n_\nu$, the definition of Γ, and defined the 4-acceleration of the Eulerian observer, $a_\mu = n^\nu \nabla_\nu n_\mu = D_\mu \ln\alpha$. Given that $n^\mu n_\mu = -1$ the second term in the last line vanishes. Furthermore, by recognizing that $K_{\mu\nu} = -h^\lambda{}_\nu h^\sigma{}_\mu \nabla_\lambda n_\sigma$, we can write the first term as $-K_{\mu\nu}u^\mu u^\nu$. Substituting all these terms in Eq. (G.2) we obtain

$$
-u^\mu \nabla_\mu \Gamma + K_{\mu\nu} u^\mu u^\nu - \Gamma u^\mu D_\mu \ln\alpha = -\frac{e}{m_e} E^\mu \, {}^{(3)}u_\mu . \tag{G.6}
$$

Using now the decomposed form of u^μ (Eq. (4.17)) we can write

$$
\partial_t \Gamma = \beta^i \partial_i \Gamma - \alpha \mathcal{U}^i \partial_i \Gamma + \alpha \Gamma K_{ij} \mathcal{U}^i \mathcal{U}^j - \Gamma \mathcal{U}^i \partial_i \alpha + \frac{e}{m_e} \alpha E^i \mathcal{U}_i . \tag{G.7}
$$

Projection on Σ_t

Let us now project Eq. (4.8) with $h^\mu{}_\nu$:

$$
h^\mu{}_\sigma u^\nu \nabla_\nu u^\sigma = \frac{e}{m_e} h^\mu{}_\sigma F^{\sigma\nu} u_\nu . \tag{G.8}
$$

In the right hand side we have

$$
\begin{aligned}
\frac{e}{m_e} h^\mu{}_\sigma F^{\sigma\nu} u_\nu &= \frac{e}{m_e} h^\mu{}_\sigma (n^\sigma E^\nu - n^\nu E^\sigma + {}^{(3)}\epsilon^{\sigma\nu\lambda} B_\lambda) u_\nu \\
&= -\frac{e}{m_e} n^\nu u_\nu E^\mu + \frac{e}{m_e} \, {}^{(3)}\epsilon^{\mu\nu\lambda} B_\lambda u_\nu \\
&= \frac{e}{m_e} \Gamma E^\mu + \frac{e}{m_e} \Gamma \, {}^{(3)}\epsilon^{\mu\nu\lambda} B_\lambda \mathcal{U}_\nu .
\end{aligned} \tag{G.9}
$$

In the left hand side, instead, we start by substituting the decomposition (4.17):

$$
\begin{aligned}
h^\mu{}_\sigma u^\nu \nabla_\nu u^\sigma &= h^\mu{}_\sigma u^\nu \nabla_\nu (\Gamma n^\sigma + {}^{(3)}u^\sigma) \\
&= h^\mu{}_\sigma u^\nu n^\sigma \nabla_\nu \Gamma + \Gamma h^\mu{}_\sigma u^\nu \nabla_\nu n^\sigma + h^\mu{}_\sigma u^\nu \nabla_\nu \, {}^{(3)}u^\sigma \\
&= \Gamma h^\mu{}_\sigma (\Gamma n^\nu + {}^{(3)}u^\nu) \nabla_\nu n^\sigma + h^\mu{}_\sigma (\Gamma n^\nu + {}^{(3)}u^\nu) \nabla_\nu \, {}^{(3)}u^\sigma \\
&= \Gamma^2 h^\mu{}_\sigma a^\sigma - \Gamma K^\mu{}_\nu \, {}^{(3)}u^\nu + \Gamma h^\mu{}_\sigma n^\nu \nabla_\nu \, {}^{(3)}u^\sigma + h^\mu{}_\sigma \, {}^{(3)}u^\nu D_\nu \, {}^{(3)}u^\sigma ,
\end{aligned} \tag{G.10}
$$

where in the third step we used the orthogonality between n^μ and $h^\mu{}_\nu$, while on the fourth step we used the definition of the 4-acceleration a_μ and the extrinsic curvature $K_{\mu\nu}$. The covariant derivative D_μ has been introduced according to the definition $D_\nu \, {}^{(3)}u^\mu = h^\sigma{}_\nu h^\mu{}_\lambda \nabla_\sigma \, {}^{(3)}u^\lambda$. Let us now rewrite this equation in terms of $\mathcal{U}^\mu$:

$$
\begin{aligned}
h^\mu{}_\sigma u^\nu \nabla_\nu u^\sigma = \Gamma^2 a^\mu - \Gamma^2 K^\mu{}_\nu \mathcal{U}^\nu + \Gamma \mathcal{U}^\mu n^\nu \nabla_\nu \Gamma + \Gamma^2 h^\mu{}_\sigma n^\nu \nabla_\nu \mathcal{U}^\sigma \\
+ \mathcal{U}^\nu \mathcal{U}^\mu \Gamma D_\nu \Gamma + \Gamma^2 h^\mu{}_\sigma \mathcal{U}^\nu D_\nu \mathcal{U}^\sigma .
\end{aligned} \tag{G.11}
$$

Now we wish to rewrite the spatial components of this equation in the form of an evolution equation, and for this purpose we use a procedure similar to the one in Eqs. (A14) - (A20) of [121]. First we note that for any 3-vector ${}^{(3)}V^\mu$, $\mathcal{L}_n\,{}^{(3)}V^\nu = n^\mu\nabla_\mu\,{}^{(3)}V^\nu - {}^{(3)}V^\mu\nabla_\mu n^\nu$, so that

$$\begin{aligned} h^\nu{}_\sigma n^\mu\nabla_\mu\,{}^{(3)}V^\sigma &= h^\nu{}_\sigma\mathcal{L}_n\,{}^{(3)}V^\sigma + h^\nu{}_\sigma\,{}^{(3)}V^\mu\nabla_\mu n^\sigma \\ &= h^\nu{}_\sigma\mathcal{L}_n\,{}^{(3)}V^\sigma - {}^{(3)}V^\mu K^\nu{}_\mu . \end{aligned} \tag{G.12}$$

Now, the Lie derivative can also be written in terms of partial derivatives, and setting $\nu = i$ we obtain

$$\begin{aligned} h^i{}_\sigma n^\mu\nabla_\mu\,{}^{(3)}V^\sigma &= h^i{}_\sigma\mathcal{L}_n\,{}^{(3)}V^\sigma - {}^{(3)}V^j K^i{}_j \\ &= \frac{1}{\alpha}\partial_t\,{}^{(3)}V^i - \frac{\beta^j}{\alpha}\partial_j\,{}^{(3)}V^i + \frac{{}^{(3)}V^j}{\alpha}\partial_j\beta^i - {}^{(3)}V^j K^i{}_j\,, \end{aligned} \tag{G.13}$$

where we made use of the explicit expressions of $h^\mu{}_\nu$ and n^μ.

If we now substitute Eq. (G.13) in the i-th component of Eq. (G.11), we get

$$\begin{aligned} h^i{}_\sigma u^\nu\nabla_\nu u^\sigma &= \Gamma^2 a^i + \Gamma\mathcal{U}^i n^\nu\nabla_\nu\Gamma + \mathcal{U}^i\mathcal{U}^j\Gamma D_j\Gamma \\ &\quad + \frac{\Gamma^2}{\alpha}\Big(\partial_t\mathcal{U}^i - \beta^j\partial_j\mathcal{U}^i + \mathcal{U}^j\partial_j\beta^i\Big) \\ &\quad + \Gamma^2\mathcal{U}^j D_j\mathcal{U}^i - 2\Gamma^2 K^i{}_j\mathcal{U}^j\,. \end{aligned} \tag{G.14}$$

Next, $n^\nu\nabla_\nu\Gamma = \frac{1}{\alpha}[\partial_t\Gamma - \beta^i\partial_i\Gamma]$, which is given by Eq. (G.7). Substituting in Eq. (G.14) we obtain

$$\begin{aligned} h^i{}_\sigma u^\nu\nabla_\nu u^\sigma &= \Gamma^2 a^i + \Gamma^2\mathcal{U}^i K_{jl}\mathcal{U}^j\mathcal{U}^l - \Gamma^2\mathcal{U}^i\mathcal{U}^j\frac{\partial_j\alpha}{\alpha} \\ &\quad + \frac{\Gamma^2}{\alpha}\Big(\partial_t\mathcal{U}^i - \beta^j\partial_j\mathcal{U}^i + \mathcal{U}^j\partial_j\beta^i\Big) \\ &\quad + \frac{e}{m_e}\Gamma\mathcal{U}^i E^j\mathcal{U}_j + \Gamma^2\mathcal{U}^j D_j\mathcal{U}^i - 2\Gamma^2 K^i{}_j\mathcal{U}^j\,. \end{aligned} \tag{G.15}$$

We are now ready to replace Eq. (G.15) and the spatial components of Eq. (G.9) in the original equation (G.8) and isolate the evolution operator. The result is:

$$\begin{aligned} \partial_t\mathcal{U}^i &= \beta^j\partial_j\mathcal{U}^i - \mathcal{U}^j\partial_j\beta^i - \alpha a^i - \alpha\mathcal{U}^i K_{jl}\mathcal{U}^j\mathcal{U}^l \\ &\quad + \frac{\alpha}{\Gamma}\frac{e}{m_e}\Big(-\mathcal{U}^i E^j\mathcal{U}_j + E^i + {}^{(3)}\epsilon^{ijl}B_l\mathcal{U}_j\Big) \\ &\quad + 2\alpha K^i{}_j\mathcal{U}^j + \mathcal{U}^i\mathcal{U}^j\partial_j\alpha - \alpha\mathcal{U}^j D_j\mathcal{U}^i\,. \end{aligned} \tag{G.16}$$

G.2 Continuity equation in $3+1$ variables

Let us now use the variables that we have introduced to rewrite the continuity equation Eq. (4.9). Using the decomposition $u^\mu = \Gamma(n^\mu + \mathcal{U}^\mu)$ and the definition of the electron density seen by the Eulerian observer, $n_{EL} = \Gamma n_e$, we can rewrite Eq. (4.9) as

$$0 = \nabla_\mu[n_e\Gamma(n^\mu + \mathcal{U}^\mu)] = \nabla_\mu[n_{EL}(n^\mu + \mathcal{U}^\mu)]$$

$$= n^{\mu}\nabla_{\mu}n_{EL} + \mathcal{U}^{\mu}\nabla_{\mu}n_{EL} + n_{EL}\nabla_{\mu}n^{\mu} + n_{EL}\nabla_{\mu}\mathcal{U}^{\mu}\,. \tag{G.17}$$

Expressing $n^{\mu}\nabla_{\mu}n_{EL}$ in terms of Lie derivatives, Eq. (G.17) can be written as an evolution equation for n_{EL}:

$$\partial_t n_{EL} = \beta^i\partial_i n_{EL} + \alpha K n_{EL} - \alpha\mathcal{U}^i\partial_i n_{EL} - \alpha n_{EL}\nabla_{\mu}\mathcal{U}^{\mu}. \tag{G.18}$$

Appendix H

Numerical integration of Maxwell's equations with a plasma fluid: convergence tests

We evaluated the accuracy and the convergence properties of our code for the numerical integration of the Maxwell's equations in presence of a plasma fluid by checking how the constraint violations scale with the resolution in two test setups taken from the simulations presented in Chapter 4.

Specifically, we considered the following quantities

$$CV_{\text{Gauss}} = \partial_i E^i - e n_{EL} - \rho_{(\text{ions})}, \tag{H.1}$$

$$CV_{\text{Magnetic}} = \partial_i B^i, \tag{H.2}$$

$$CV_{\text{Plasma}} = \sqrt{\Gamma^2 (1 - \mathcal{U}_i \mathcal{U}^i)} - 1, \tag{H.3}$$

which, whenever nonzero, represent the violations of the Gauss law (4.23), of the Gauss law for magnetism (4.24), and of the normalization condition in Eq. (4.30), respectively.

In order to asses the reliability of our code I show here the convergence in the two most challenging nonlinear regimes: WB and blowout (although not shown, the convergence of the linear regime is excellent). Starting from the former, we repeated the simulation with $A_E = 1$ whose characteristic are described in Sec. 4.5.2, using a lower resolution $\Delta x = \Delta y = \Delta z = 0.4$, and increasing the grid size to $[-4, 4] \times [-4, 4] \times [-1450, 1150]$ in order to maintain 21 grid points along the x and y directions. We also doubled the time step to $\Delta t = 0.2$, in order to keep the CFL factor constant.

Figure H.1 shows the constraint violations CV_{Gauss} (left panel) and CV_{Plasma} (right panel) along the z axis at $t = 830$, slightly before WB happens (cf. right panel of Fig. 4.6). In general, while for both the constraint violations there is a region where they are dominated by noise, in the central region they show an excellent fourth order scaling, and convergence is lost only for $65 \lesssim z \lesssim 75$, where the WB phenomenon is taking place. Although not shown, the violation CV_{Magnetic} is extremely small and dominated by noise, with values $\lesssim 10^{-14}$.

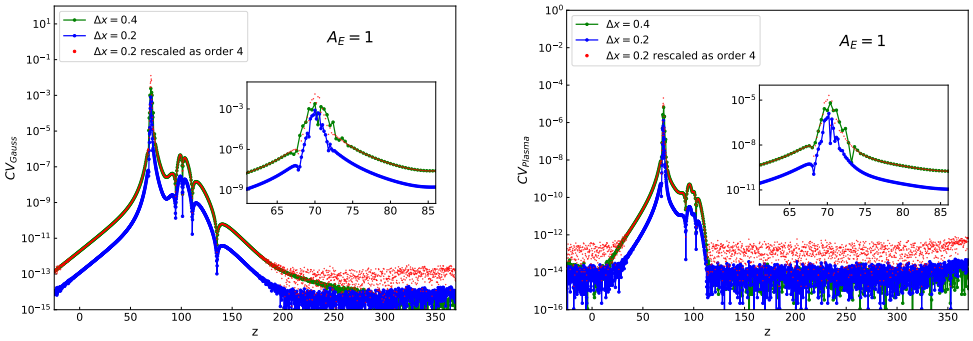

Figure H.1. Scaling of the violations of the Gauss Law (left panel) and the condition $u^\mu u_\mu = -1$ along the z axis, for the simulation in the nonlinear regime with $A_E = 1$. CV_{Gauss} and CV_{Plasma} are extracted at $t = 830$, when the WB phenomenon starts taking place. Overall the code converges extremely well, except in the region around the spike of n_{EL}, where the constraint violation displays a peak. The insets show a magnification of the constraint violations around this region.

Let me now move to consider the convergence in the blowout regime. We repeated the simulation with $A_E = 1000$ using grid steps $\Delta x = \Delta y = \Delta z = 0.4$ while maintaining the CFL factor constant. As in the previous case we extended the grid to $[-4, 4] \times [-4, 4] \times [-750, 850]$ in order to have the same number of grid points along the transverse directions x and y. The scaling of CV_{Gauss} and CV_{Plasma} on the z axis at $t = 190$ is shown in the left and right panel of Fig. H.2, respectively. We can see that the code converges extremely well, except in the region just behind the peak of the plasma density (cf. lowest panel of Fig. 4.4). However, it is worth noting that the extension of the region where convergence is lost decreases as the resolution increases, and that fourth-order scaling is restored in the plasma-depleted region. As for the violation of Eq. (4.24), also in this case CV_{Magnetic} is small and dominated by noise, assuming values $\lesssim 10^{-11}$.

Given the excellent convergence properties in the nonlinear regime, we concluded that the code is reliable and produces accurate results at the resolutions used in Chapter 4

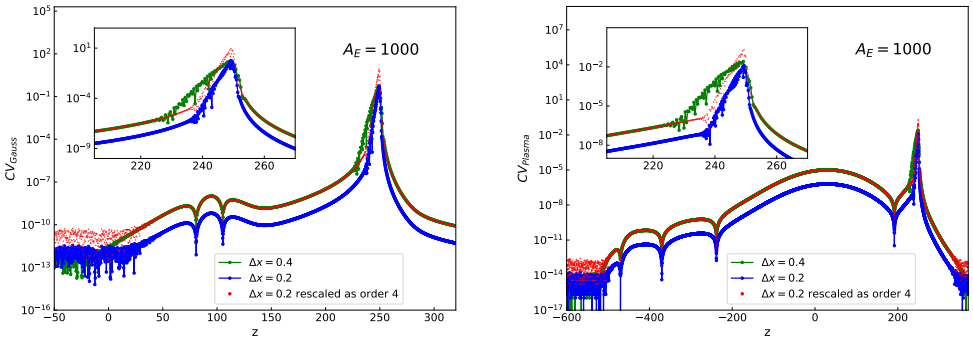

Figure H.2. Convergence of CV_{Gauss}(left panel) and CV_{Plasma}(right panel) along the z axis for the simulation in the nonlinear regime with $A_E = 1000$. The constraint violation is computed at $t = 190$, when the system is in the blowout regime. As we can see it satisfies fourth-order scaling except in the region close to the "transported" plasma and behind it, where the constraint violations have a peak. This can be better appreciated in the inset, that contains a magnification of the constraint violation around this region.

Appendix I

Simulations of an EM wave packet scattering off a plasma barrier: homogeneity along the transverse directions

Throughout the work described in Chapter 4, we used numerical grids whose extension along the transverse directions x and y is significantly smaller than in the z direction. This had the advantage of reducing considerably the computational cost, and could be done by exploiting the planar geometry of the system under consideration. In this appendix, I would like to show that homogeneity of the variables along the transverse directions is preserved also at late times during the evolution, so that this grid structure is compatible with the physical properties of the system for the entire duration of the simulations.

For this purpose let me consider the simulation in the nonlinear regime with $A_E = 1000$, and extract the profiles of E^x, E^y, E^z, and n_{EL} along the x and y axes at $z = 240$. This operation is performed at $t = 180$ when the system is already in a blowout state, and the value of the z coordinate is chosen to be where plasma is concentrated at this time.

The results are shown in Fig. I.1, where the left and right panels represent the profiles along the x and y axes, respectively. We can see that all the profiles are constant along the axes, and that the values are consistent between the two plots, confirming that the system maintains homogeneity along the transverse directions.

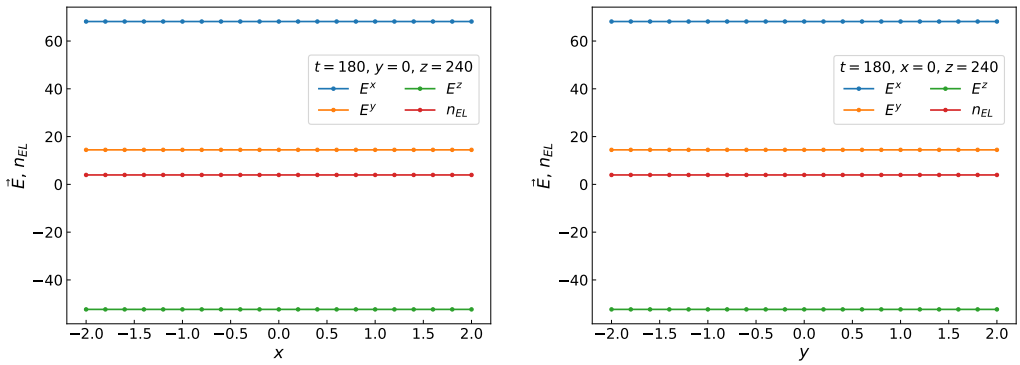

Figure I.1. Profiles of $\vec{E}$ and n_{EL} along the transverse directions x (left) and y (right) at $z = 240$ for the simulation with initial amplitude $A_E = 1000$. These data are extracted at $t = 180$, when the system is already in the blowout regime, and in the spatial region where the plasma density peaks. All the profiles are constant in x and y, with values consistent between the two plots. This confirms that the homogeneity property is conserved during the $3 + 1$ simulations.

Bibliography

[1] J. Witt-Hansen, "H.C. Örsted, Immanuel Kant, and the Thought Experiment", *Danish Yearbook of Philosophy* **13** (1976), 48 .

[2] G. Galilei, *Dialogo sopra i due massimi sistemi del mondo*, Giovanni Battista Landini, Florence (1632).

[3] G. Galilei, *Discorsi e dimostrazioni matematiche intorno a due nuove scienze attenenti alla meccanica e i movimenti locali*, Elzevir, Leiden (1638).

[4] S. Newton, Isaac, *Philosophiæ Naturalis Principia Mathematica*, Jussu Societatis Regiae ac Typis Josephi Streater. Prostat apud plures bibliopolas, London (1687).

[5] A. Einstein, "Zur Elektrodynamik bewegter Körper", *Annalen der Physik* **322** (1905), 891.

[6] P. Langevin, "L'Évolution de l'espace et du temps", *Scientia* **10** (1911), 31.

[7] E. Schrödinger, "Die gegenwärtige Situation in der Quantenmechanik", *Naturwissenschaften* **23** (1935), 807.

[8] E. Dewan and M. Beran, "Note on Stress Effects due to Relativistic Contraction", *American Journal of Physics* **27** (1959), 517.

[9] J. S. Bell, *How to Teach Special Relativity*, pp. 61–73, WORLD SCIENTIFIC (2001) .

[10] F. J. Dyson, "Search for Artificial Stellar Sources of Infrared Radiation", *Science* **131** (1960), 1667.

[11] A. Einstein, B. Podolsky, and N. Rosen, "Can Quantum-Mechanical Description of Physical Reality Be Considered Complete?", *Phys. Rev.* **47** (1935), 777.

[12] I. Newton, *De mundi systemate liber*, Impensis J. Tonson, J. Osborn & T. Longman, London (1728).

[13] M. S. Morris, K. S. Thorne, and U. Yurtsever, "Wormholes, Time Machines, and the Weak Energy Condition", *Phys. Rev. Lett.* **61** (1988), 1446.

[14] F. Echeverria, G. Klinkhammer, and K. S. Thorne, "Billiard balls in wormhole spacetimes with closed timelike curves: Classical theory", *Phys. Rev. D* **44** (1991), 1077.

[15] J. Friedman, M. S. Morris, I. D. Novikov, F. Echeverria, G. Klinkhammer, K. S. Thorne, and U. Yurtsever, "Cauchy problem in spacetimes with closed timelike curves", *Phys. Rev. D* **42** (1990), 1915.

[16] B. P. Abbott *et al.* [LIGO Scientific Collaboration and Virgo Collaboration], "GWTC-1: A Gravitational-Wave Transient Catalog of Compact Binary Mergers Observed by LIGO and Virgo during the First and Second Observing Runs", *Phys. Rev. X* **9** (2019), 031040, arXiv: 1811.12907 [astro-ph.HE].

[17] R. Abbott *et al.* [LIGO Scientific Collaboration and Virgo Collaboration], "GWTC-2: Compact Binary Coalescences Observed by LIGO and Virgo during the First Half of the Third Observing Run", *Phys. Rev. X* **11** (2021), 021053, arXiv: 2010.14527 [gr-qc].

[18] R. Abbott *et al.* [LIGO Scientific Collaboration and Virgo Collaboration], "GWTC-2.1: Deep Extended Catalog of Compact Binary Coalescences Observed by LIGO and Virgo During the First Half of the Third Observing Run", (2021), arXiv: 2108.01045 [gr-qc].

[19] R. Abbott *et al.* [LIGO Scientific Collaboration, Virgo Collaboration, and KAGRA Collaboration], "GWTC-3: Compact Binary Coalescences Observed by LIGO and Virgo During the Second Part of the Third Observing Run", (2021), arXiv: 2111.03606 [gr-qc].

[20] K. Akiyama *et al.* [Event Horizon Telescope Collaboration], "First M87 Event Horizon Telescope Results. I. The Shadow of the Supermassive Black Hole", *Astrophys. J. Lett.* **875** (2019), L1, arXiv: 1906.11238 [astro-ph.GA].

[21] K. Akiyama *et al.* [Event Horizon Telescope Collaboration], "First Sagittarius A* Event Horizon Telescope Results. I. The Shadow of the Supermassive Black Hole in the Center of the Milky Way", *Astrophys. J. Lett.* **930** (2022), L12.

[22] Abuter, R. *et al.* [GRAVITY Collaboration], "Detection of the gravitational redshift in the orbit of the star S2 near the Galactic centre massive black hole", *A&A* **615** (2018), L15, arXiv: 1807.09409 [astro-ph.GA].

[23] T. Do *et al.*, "Relativistic redshift of the star S0-2 orbiting the Galactic Center supermassive black hole", *Science* **365** (2019), 664, arXiv: 1907.10731 [astro-ph.GA].

[24] Abuter, R. *et al.* [GRAVITY Collaboration], "Detection of the Schwarzschild precession in the orbit of the star S2 near the Galactic centre massive black hole", *A&A* **636** (2020), L5, arXiv: 2004.07187 [astro-ph.GA].

[25] A. Einstein and N. Rosen, "The Particle Problem in the General Theory of Relativity", *Phys. Rev.* **48** (1935), 73.

[26] H. G. Ellis, "Ether flow through a drainhole: A particle model in general relativity", *J. Math. Phys.* **14** (1973), 104.

[27] K. A. Bronnikov, "Scalar-Tensor Theory and Scalar Charge", *Acta Phys. Pol. B* **4** (1973), 251.

[28] M. S. Morris and K. S. Thorne, "Wormholes in spacetime and their use for interstellar travel: A tool for teaching general relativity", *Am. J. Phys.* **56** (1988), 395.

[29] P. O. Mazur and E. Mottola, "Gravitational Condensate Stars: An Alternative to Black Holes", *Universe* **9** (2023), 88, arXiv: gr-qc/0109035.

[30] P. O. Mazur and E. Mottola, "Gravitational vacuum condensate stars", *Proc. Nat. Acad. Sci.* **101** (2004), 9545, arXiv: gr-qc/0407075.

[31] D. J. Kaup, "Klein-Gordon Geon", *Phys. Rev.* **172** (1968), 1331.

[32] R. Ruffini and S. Bonazzola, "Systems of Self-Gravitating Particles in General Relativity and the Concept of an Equation of State", *Phys. Rev.* **187** (1969), 1767.

[33] M. Colpi, S. L. Shapiro, and I. Wasserman, "Boson Stars: Gravitational Equilibria of Self-Interacting Scalar Fields", *Phys. Rev. Lett.* **57** (1986), 2485.

[34] R. Brito, V. Cardoso, C. A. R. Herdeiro, and E. Radu, "Proca stars: Gravitating Bose–Einstein condensates of massive spin 1 particles", *Phys. Lett. B* **752** (2016), 291, arXiv: 1508.05395 [gr-qc].

[35] S. L. Liebling and C. Palenzuela, "Dynamical boson stars", *Living Rev. Rel.* **26** (2023), 1, arXiv: 1202.5809 [gr-qc].

[36] V. Cardoso and P. Pani, "Testing the nature of dark compact objects: a status report", *Living Rev. Rel.* **22** (2019), 4, arXiv: 1904.05363 [gr-qc].

[37] S. Weinberg, *The Quantum Theory of Fields. Vol. 1: Foundations*, Cambridge University Press, Cambridge, UK (2005), ISBN 978-0-521-67053-1, 978-0-511-25204-4.

[38] S. Weinberg, "The cosmological constant problem", *Rev. Mod. Phys.* **61** (1989), 1.

[39] E. Berti *et al.*, "Testing General Relativity with Present and Future Astrophysical Observations", *Class. Quant. Grav.* **32** (2015), 243001, arXiv: 1501.07274 [gr-qc].

[40] E. N. Saridakis *et al.* [CANTATA], *Modified Gravity and Cosmology: An Update by the CANTATA Network*, Springer Cham (2021), ISBN 978-3-030-83714-3, 978-3-030-83717-4, 978-3-030-83715-0, arXiv: 2105.12582 [gr-qc].

[41] J. M. Ezquiaga and M. Zumalacárregui, "Dark Energy in Light of Multi-Messenger Gravitational-Wave Astronomy", *Front. Astron. Space Sci.* **5** (2018), 44, arXiv: 1807.09241 [astro-ph.CO].

[42] F. Corelli, T. Ikeda, and P. Pani, "Challenging cosmic censorship in Einstein-Maxwell-scalar theory with numerically simulated gedanken experiments", *Phys. Rev. D* **104** (2021), 084069, arXiv: 2108.08328 [gr-qc].

[43] F. Corelli, M. de Amicis, T. Ikeda, and P. Pani, "What Is the Fate of Hawking Evaporation in Gravity Theories with Higher Curvature Terms?", *Phys. Rev. Lett.* **130** (2023), 091501, arXiv: 2205.13006 [gr-qc].

[44] F. Corelli, M. de Amicis, T. Ikeda, and P. Pani, "Nonperturbative gedanken experiments in Einstein-dilaton-Gauss-Bonnet gravity: Nonlinear transitions and tests of the cosmic censorship beyond general relativity", *Phys. Rev. D* **107** (2023), 044061, arXiv: 2205.13007 [gr-qc].

[45] E. Cannizzaro, F. Corelli, and P. Pani, "Nonlinear photon-plasma interaction and the black hole superradiant instability", *Phys. Rev. D* **109** (2024), 023007, arXiv: 2306.12490 [gr-qc].

[46] R. Penrose, "Gravitational collapse: The role of general relativity", *Riv. Nuovo Cim.* **1** (1969), 252.

[47] R. M. Wald, *General Relativity*, University of Chicago Press, Chicago, USA (1984).

[48] R. M. Wald, *Gravitational Collapse and Cosmic Censorship*, pp. 69–86, Springer Netherlands, Dordrecht (1999) .

[49] S. W. Hawking, "Breakdown of predictability in gravitational collapse", *Phys. Rev. D* **14** (1976), 2460.

[50] Y. C. Ong, "Space–time singularities and cosmic censorship conjecture: A Review with some thoughts", *Int. J. Mod. Phys. A* **35** (2020), 2030007, arXiv: 2005.07032 [gr-qc].

[51] R. Penrose, "Gravitational Collapse and Space-Time Singularities", *Phys. Rev. Lett.* **14** (1965), 57.

[52] S. W. Hawking and R. Penrose, "The singularities of gravitational collapse and cosmology", *Proc. Roy. Soc. Lond. A* **314** (1970), 529.

[53] R. Wald, "Gedanken experiments to destroy a black hole", *Annals of Physics* **82** (1974), 548, ISSN 0003-4916.

[54] V. E. Hubeny, "Overcharging a black hole and cosmic censorship", *Phys. Rev. D* **59** (1999), 064013, arXiv: gr-qc/9808043.

[55] T. Jacobson and T. P. Sotiriou, "Over-spinning a black hole with a test body", *Phys. Rev. Lett.* **103** (2009), 141101, [Erratum: Phys.Rev.Lett. 103, 209903 (2009)], arXiv: 0907.4146 [gr-qc].

[56] A. Saa and R. Santarelli, "Destroying a near-extremal Kerr-Newman black hole", *Phys. Rev. D* **84** (2011), 027501, arXiv: 1105.3950 [gr-qc].

[57] S. Isoyama, N. Sago, and T. Tanaka, "Cosmic censorship in overcharging a Reissner-Nordström black hole via charged particle absorption", *Phys. Rev. D* **84** (2011), 124024, arXiv: 1108.6207 [gr-qc].

[58] J. Natário, L. Queimada, and R. Vicente, "Test fields cannot destroy extremal black holes", *Class. Quant. Grav.* **33** (2016), 175002, arXiv: 1601.06809 [gr-qc].

[59] H. M. Siahaan and P. C. Tjiang, "Destroying Kaluza-Klein and Kerr-Newman black holes", (2021), arXiv: 2108.06523 [gr-qc].

[60] P. Aniceto, P. Pani, and J. V. Rocha, "Radiating black holes in Einstein-Maxwell-dilaton theory and cosmic censorship violation", *JHEP* **05** (2016), 115, arXiv: 1512.08550 [hep-th].

[61] I. Semiz, "Dyonic Kerr-Newman black holes, complex scalar field and cosmic censorship", *Gen. Rel. Grav.* **43** (2011), 833, arXiv: gr-qc/0508011.

[62] K. Düztaş and I. Semiz, "Cosmic Censorship, Black Holes and Integer-spin Test Fields", *Phys. Rev. D* **88** (2013), 064043, arXiv: 1307.1481 [gr-qc].

[63] K. Düztaş, "Cosmic censorship, massless fermionic test fields, and absorption probabilities", *Eur. Phys. J. C* **81** (2021), 1131, arXiv: 2107.05345 [gr-qc].

[64] G. Bozzola, "Does Charge Matter in High-Energy Collisions of Black Holes?", *Phys. Rev. Lett.* **128** (2022), 071101, arXiv: 2202.05310 [gr-qc].

[65] G. Bozzola and V. Paschalidis, "Can quasicircular mergers of charged black holes produce extremal black holes?", *Phys. Rev. D* **108** (2023), 064010, arXiv: 2309.04368 [gr-qc].

[66] E. Barausse, V. Cardoso, and G. Khanna, "Test bodies and naked singularities: Is the self-force the cosmic censor?", *Phys. Rev. Lett.* **105** (2010), 261102, arXiv: 1008.5159 [gr-qc].

[67] E. Barausse, V. Cardoso, and G. Khanna, "Testing the Cosmic Censorship Conjecture with point particles: the effect of radiation reaction and the self-force", *Phys. Rev. D* **84** (2011), 104006, arXiv: 1106.1692 [gr-qc].

[68] P. Zimmerman, I. Vega, E. Poisson, and R. Haas, "Self-force as a cosmic censor", *Phys. Rev. D* **87** (2013), 041501, arXiv: 1211.3889 [gr-qc].

[69] M. Colleoni and L. Barack, "Overspinning a Kerr black hole: the effect of self-force", *Phys. Rev. D* **91** (2015), 104024, arXiv: 1501.07330 [gr-qc].

[70] J. Sorce and R. M. Wald, "Gedanken experiments to destroy a black hole. II. Kerr-Newman black holes cannot be overcharged or overspun", *Phys. Rev. D* **96** (2017), 104014, arXiv: 1707.05862 [gr-qc].

[71] M. Colleoni, L. Barack, A. G. Shah, and M. van de Meent, "Self-force as a cosmic censor in the Kerr overspinning problem", *Phys. Rev. D* **92** (2015), 084044, arXiv: 1508.04031 [gr-qc].

[72] R. Brito, V. Cardoso, and P. Pani, "Superradiance: New Frontiers in Black Hole Physics", *Lect. Notes Phys.* **906** (2015), pp.1, arXiv: 1501.06570 [gr-qc].

[73] I. R. Vasquez, "Overspinning problem in Kerr black holes: second order corrections and self-energy", (2021), arXiv: 2107.13135 [gr-qc].

[74] A. Sang and J. Jiang, "Gedanken experiments at high-order approximation: Kerr black hole cannot be overspun", *JHEP* **2021** (2021), 95, arXiv: 2108.03454 [gr-qc].

[75] J. M. Torres and M. Alcubierre, "Gravitational collapse of charged scalar fields", *Gen. Rel. Grav.* **46** (2014), 1773, arXiv: 1407.7885 [gr-qc].

[76] C. A. R. Herdeiro, E. Radu, N. Sanchis-Gual, and J. A. Font, "Spontaneous Scalarization of Charged Black Holes", *Phys. Rev. Lett.* **121** (2018), 101102, arXiv: 1806.05190 [gr-qc].

[77] D. D. Doneva and S. S. Yazadjiev, "New Gauss-Bonnet Black Holes with Curvature-Induced Scalarization in Extended Scalar-Tensor Theories", *Phys. Rev. Lett.* **120** (2018), 131103, arXiv: 1711.01187 [gr-qc].

[78] H. O. Silva, J. Sakstein, L. Gualtieri, T. P. Sotiriou, and E. Berti, "Spontaneous scalarization of black holes and compact stars from a Gauss-Bonnet coupling", *Phys. Rev. Lett.* **120** (2018), 131104, arXiv: 1711.02080 [gr-qc].

[79] D. D. Doneva, F. M. Ramazanoğlu, H. O. Silva, T. P. Sotiriou, and S. S. Yazadjiev, "Scalarization", (2022), arXiv: 2211.01766 [gr-qc].

[80] E. W. Hirschmann, L. Lehner, S. L. Liebling, and C. Palenzuela, "Black hole dynamics in Einstein-Maxwell-dilaton theory", *Phys. Rev. D* **97** (2018), 064032, arXiv: 1706.09875 [gr-qc].

[81] M. Boskovic, R. Brito, V. Cardoso, T. Ikeda, and H. Witek, "Axionic instabilities and new black hole solutions", *Phys. Rev. D* **99** (2019), 035006, arXiv: 1811.04945 [gr-qc].

[82] C.-Y. Zhang, P. Liu, Y. Liu, C. Niu, and B. Wang, "Dynamical scalarization in Einstein-Maxwell-dilaton theory", *Phys. Rev. D* **105** (2022), 024073, arXiv: 2111.10744 [gr-qc].

[83] C.-Y. Zhang, Q. Chen, Y. Liu, W.-K. Luo, Y. Tian, and B. Wang, "Critical Phenomena in Dynamical Scalarization of Charged Black Holes", *Phys. Rev. Lett.* **128** (2022), 161105, arXiv: 2112.07455 [gr-qc].

[84] D. Garfinkle, G. T. Horowitz, and A. Strominger, "Charged black holes in string theory", *Phys. Rev. D* **43** (1991), 3140, [Erratum: Phys. Rev. D 45, 3888 (1992)].

[85] H. O. Silva, H. Witek, M. Elley, and N. Yunes, "Dynamical Descalarization in Binary Black Hole Mergers", *Phys. Rev. Lett.* **127** (2021), 031101, arXiv: 2012.10436 [gr-qc].

[86] M. Elley, H. O. Silva, H. Witek, and N. Yunes, "Spin-induced dynamical scalarization, descalarization, and stealthness in scalar-Gauss-Bonnet gravity during a black hole coalescence", *Phys. Rev. D* **106** (2022), 044018, arXiv: 2205.06240 [gr-qc].

[87] D. D. Doneva, A. Vañó Viñuales, and S. S. Yazadjiev, "Dynamical descalarization with a jump during a black hole merger", *Phys. Rev. D* **106** (2022), L061502, arXiv: 2204.05333 [gr-qc].

[88] P. Kanti, N. E. Mavromatos, J. Rizos, K. Tamvakis, and E. Winstanley, "Dilatonic black holes in higher curvature string gravity", *Phys. Rev. D* **54** (1996), 5049, arXiv: hep-th/9511071.

[89] D. J. Gross and J. H. Sloan, "The Quartic Effective Action for the Heterotic String", *Nucl. Phys. B* **291** (1987), 41.

[90] C. M. Will, "The Confrontation between General Relativity and Experiment", *Living Rev. Rel.* **17** (2014), 4, arXiv: 1403.7377 [gr-qc].

[91] S. O. Alexeev and M. V. Pomazanov, "Black hole solutions with dilatonic hair in higher curvature gravity", *Phys. Rev. D* **55** (1997), 2110, arXiv: hep-th/9605106.

[92] T. Torii, H. Yajima, and K.-i. Maeda, "Dilatonic black holes with Gauss-Bonnet term", *Phys. Rev. D* **55** (1997), 739, arXiv: gr-qc/9606034.

[93] P. Pani and V. Cardoso, "Are black holes in alternative theories serious astrophysical candidates? The Case for Einstein-Dilaton-Gauss-Bonnet black holes", *Phys. Rev. D* **79** (2009), 084031, arXiv: 0902.1569 [gr-qc].

[94] S. W. Hawking, "Particle Creation by Black Holes", *Commun. Math. Phys.* **43** (1975), 199, [Erratum: Commun.Math.Phys. 46, 206 (1976)].

[95] M. De Amicis, "Black hole evaporation in Einstein-dilaton-Gauss-Bonnet gravity", Master's thesis, Sapienza University of Rome (2021).

[96] S. Alexeyev, A. Barrau, G. Boudoul, O. Khovanskaya, and M. Sazhin, "Black hole relics in string gravity: Last stages of Hawking evaporation", *Class. Quant. Grav.* **19** (2002), 4431, arXiv: gr-qc/0201069.

[97] Y. B. Zel'Dovich, "Generation of Waves by a Rotating Body", *ZhETF Pisma Redaktsiiu* **14** (1971), 270.

[98] Y. B. Zel'Dovich, "Amplification of cylindrical electromagnetic waves reflected from a rotating body", *ZhETF* **62** (1972), 2076.

[99] S. A. Teukolsky and W. H. Press, "Perturbations of a rotating black hole. III. Interaction of the hole with gravitational and electromagnetic radiation", *Astrophys. J.* **193** (1974), 443.

[100] W. H. Press and S. A. Teukolsky, "Floating Orbits, Superradiant Scattering and the Black-hole Bomb", *Nature* **238** (1972), 211.

[101] T. Damour, N. Deruelle, and R. Ruffini, "On Quantum Resonances in Stationary Geometries", *Lett. Nuovo Cim.* **15** (1976), 257.

[102] S. L. Detweiler, "Klein-Gordon equation and rotating black holes", *Phys. Rev. D* **22** (1980), 2323.

[103] L. Tonks and I. Langmuir, "Oscillations in Ionized Gases", *Phys. Rev.* **33** (1929), 195.

[104] F. F. Chen, *Introduction to Plasma Physics and Controlled Fusion*, volume 1: Plasma Physics, Springer New York, NY (1984), ISBN 978-1-4419-3201-3.

[105] R. Kulsrud and A. Loeb, "Dynamics and gravitational interaction of waves in nonuniform media", *Phys. Rev. D* **45** (1992), 525.

[106] P. Pani and A. Loeb, "Constraining primordial black-hole bombs through spectral distortions of the cosmic microwave background", *Phys. Rev. D* **88** (2013), 041301, arXiv: 1307.5176 [astro-ph.CO].

[107] J. P. Conlon and C. A. R. Herdeiro, "Can black hole superradiance be induced by galactic plasmas?", *Phys. Lett. B* **780** (2018), 169, arXiv: 1701.02034 [astro-ph.HE].

[108] E. Cannizzaro, A. Caputo, L. Sberna, and P. Pani, "Plasma-photon interaction in curved spacetime: Formalism and quasibound states around nonspinning black holes", *Phys. Rev. D* **103** (2021), 124018, arXiv: 2012.05114 [gr-qc].

[109] E. Cannizzaro, A. Caputo, L. Sberna, and P. Pani, "Plasma-photon interaction in curved spacetime. II. Collisions, thermal corrections, and superradiant instabilities", *Phys. Rev. D* **104** (2021), 104048, arXiv: 2107.01174 [gr-qc].

[110] V. Cardoso, W.-D. Guo, C. F. B. Macedo, and P. Pani, "The tune of the Universe: the role of plasma in tests of strong-field gravity", *Mon. Not. Roy. Astron. Soc.* **503** (2021), 563, arXiv: 2009.07287 [gr-qc].

[111] P. Kaw and J. Dawson, "Relativistic Nonlinear Propagation of Laser Beams in Cold Overdense Plasmas", *Physics of Fluids* **13** (1970), 472.

[112] S. W. Hawking and G. F. R. Ellis, *The Large Scale Structure of Space-Time*, Cambridge University Press (1973).

[113] D. Astefanesei, C. Herdeiro, A. Pombo, and E. Radu, "Einstein-Maxwell-scalar black holes: classes of solutions, dyons and extremality", *JHEP* **2019** (2019), 78, arXiv: 1905.08304 [hep-th].

[114] P. G. S. Fernandes, C. A. R. Herdeiro, A. M. Pombo, E. Radu, and N. Sanchis-Gual, "Spontaneous Scalarisation of Charged Black Holes: Coupling Dependence and Dynamical Features", *Class. Quant. Grav.* **36** (2019), 134002, [Erratum: Class.Quant.Grav. 37, 049501 (2020)], arXiv: 1902.05079 [gr-qc].

[115] J. L. Blázquez-Salcedo, C. A. R. Herdeiro, J. Kunz, A. M. Pombo, and E. Radu, "Einstein-Maxwell-scalar black holes: the hot, the cold and the bald", *Phys. Lett. B* **806** (2020), 135493, arXiv: 2002.00963 [gr-qc].

[116] P. G. S. Fernandes, "Einstein–Maxwell-scalar black holes with massive and self-interacting scalar hair", *Phys. Dark Univ.* **30** (2020), 100716, arXiv: 2003.01045 [gr-qc].

[117] M. Shibata and T. Nakamura, "Evolution of three-dimensional gravitational waves: Harmonic slicing case", *Phys. Rev. D* **52** (1995), 5428.

[118] T. W. Baumgarte and S. L. Shapiro, "On the numerical integration of Einstein's field equations", *Phys. Rev. D* **59** (1998), 024007, arXiv: gr-qc/9810065.

[119] J. D. Brown, "Covariant formulations of BSSN and the standard gauge", *Phys. Rev. D* **79** (2009), 104029, arXiv: 0902.3652 [gr-qc].

[120] M. Alcubierre and M. D. Mendez, "Formulations of the 3+1 evolution equations in curvilinear coordinates", *Gen. Rel. Grav.* **43** (2011), 2769, arXiv: 1010.4013 [gr-qc].

[121] M. Alcubierre, J. C. Degollado, and M. Salgado, "The Einstein-Maxwell system in 3+1 form and initial data for multiple charged black holes", *Phys. Rev. D* **80** (2009), 104022, arXiv: 0907.1151 [gr-qc].

[122] C. Bona, J. Masso, E. Seidel, and J. Stela, "A New formalism for numerical relativity", *Phys. Rev. Lett.* **75** (1995), 600, arXiv: gr-qc/9412071.

[123] M. Alcubierre, B. Bruegmann, P. Diener, M. Koppitz, D. Pollney, E. Seidel, and R. Takahashi, "Gauge conditions for long term numerical black hole evolutions without excision", *Phys. Rev. D* **67** (2003), 084023, arXiv: gr-qc/0206072.

[124] P. J. Montero and I. Cordero-Carrion, "BSSN equations in spherical coordinates without regularization: vacuum and non-vacuum spherically symmetric spacetimes", *Phys. Rev. D* **85** (2012), 124037, arXiv: 1204.5377 [gr-qc].

[125] I. Cordero-Carrion and P. Cerda-Duran, "Partially implicit Runge-Kutta methods for wave-like equations in spherical-type coordinates", (2012), arXiv: 1211.5930 [math-ph].

[126] D. Christodoulou and R. Ruffini, "Reversible transformations of a charged black hole", *Phys. Rev. D* **4** (1971), 3552.

[127] https://web.uniroma1.it/gmunu/.

[128] J. L. Ripley and F. Pretorius, "Gravitational collapse in Einstein dilaton-Gauss–Bonnet gravity", *Class. Quant. Grav.* **36** (2019), 134001, arXiv: 1903.07543 [gr-qc].

[129] F. Corelli, "Instability of Schwarzschild Black Holes in Einstein-scalar-Gauss-Bonnet Gravity: Perturbative Approach and Time-Domain Analysis", Master's thesis, Sapienza University of Rome (2020), arXiv: 2112.12048 [gr-qc].

[130] G. W. Horndeski, "Second-order scalar-tensor field equations in a four-dimensional space", *Int. J. Theor. Phys.* **10** (1974), 363.

[131] T. Kobayashi, "Horndeski theory and beyond: a review", *Rept. Prog. Phys.* **82** (2019), 086901, arXiv: 1901.07183 [gr-qc].

[132] R. P. Woodard, "Avoiding dark energy with 1/r modifications of gravity", *Lect. Notes Phys.* **720** (2007), 403, arXiv: astro-ph/0601672.

[133] D. D. Doneva, S. Kiorpelidi, P. G. Nedkova, E. Papantonopoulos, and S. S. Yazadjiev, "Charged Gauss-Bonnet black holes with curvature induced scalarization in the extended scalar-tensor theories", *Phys. Rev. D* **98** (2018), 104056, arXiv: 1809.00844 [gr-qc].

[134] P. V. P. Cunha, C. A. R. Herdeiro, and E. Radu, "Spontaneously Scalarized Kerr Black Holes in Extended Scalar-Tensor–Gauss-Bonnet Gravity", *Phys. Rev. Lett.* **123** (2019), 011101, arXiv: 1904.09997 [gr-qc].

[135] C. A. R. Herdeiro, E. Radu, H. O. Silva, T. P. Sotiriou, and N. Yunes, "Spin-induced scalarized black holes", *Phys. Rev. Lett.* **126** (2021), 011103, arXiv: 2009.03904 [gr-qc].

[136] L. G. Collodel, B. Kleihaus, J. Kunz, and E. Berti, "Spinning and excited black holes in Einstein-scalar-Gauss–Bonnet theory", *Class. Quant. Grav.* **37** (2020), 075018, arXiv: 1912.05382 [gr-qc].

[137] A. Dima, E. Barausse, N. Franchini, and T. P. Sotiriou, "Spin-induced black hole spontaneous scalarization", *Phys. Rev. Lett.* **125** (2020), 231101, arXiv: 2006.03095 [gr-qc].

[138] E. Berti, L. G. Collodel, B. Kleihaus, and J. Kunz, "Spin-induced black-hole scalarization in Einstein-scalar-Gauss-Bonnet theory", *Phys. Rev. Lett.* **126** (2021), 011104, arXiv: 2009.03905 [gr-qc].

[139] Y. Brihaye and B. Hartmann, "Spontaneous scalarization of charged black holes at the approach to extremality", *Phys. Lett. B* **792** (2019), 244, arXiv: 1902.05760 [gr-qc].

[140] C. A. R. Herdeiro, A. M. Pombo, and E. Radu, "Aspects of Gauss-Bonnet Scalarisation of Charged Black Holes", *Universe* **7** (2021), 483, arXiv: 2111.06442 [gr-qc].

[141] G. Antoniou, A. Bakopoulos, and P. Kanti, "Evasion of No-Hair Theorems and Novel Black-Hole Solutions in Gauss-Bonnet Theories", *Phys. Rev. Lett.* **120** (2018), 131102, arXiv: 1711.03390 [hep-th].

[142] T. P. Sotiriou and S.-Y. Zhou, "Black hole hair in generalized scalar-tensor gravity: An explicit example", *Phys. Rev. D* **90** (2014), 124063, arXiv: 1408.1698 [gr-qc].

[143] T. Torii and K.-i. Maeda, "Stability of a dilatonic black hole with a Gauss-Bonnet term", *Phys. Rev. D* **58** (1998), 084004.

[144] T. P. Sotiriou and S.-Y. Zhou, "Black hole hair in generalized scalar-tensor gravity", *Phys. Rev. Lett.* **112** (2014), 251102, arXiv: 1312.3622 [gr-qc].

[145] N. D. Birrell and P. C. W. Davies, *Quantum Fields in Curved Space*, Cambridge Monographs on Mathematical Physics, Cambridge University Press, Cambridge, UK (1982), ISBN 978-0-521-27858-4, 978-0-521-27858-4.

[146] R. A. Konoplya, A. F. Zinhailo, and Z. Stuchlík, "Quasinormal modes, scattering, and Hawking radiation in the vicinity of an Einstein-dilaton-Gauss-Bonnet black hole", *Phys. Rev. D* **99** (2019), 124042, arXiv: 1903.03483 [gr-qc].

[147] T. Regge and J. A. Wheeler, "Stability of a Schwarzschild singularity", *Phys. Rev.* **108** (1957), 1063.

[148] P. Kanti, B. Kleihaus, and J. Kunz, "Wormholes in Dilatonic Einstein-Gauss-Bonnet Theory", *Phys. Rev. Lett.* **107** (2011), 271101, arXiv: 1108.3003 [gr-qc].

[149] P. Kanti, B. Kleihaus, and J. Kunz, "Stable Lorentzian Wormholes in Dilatonic Einstein-Gauss-Bonnet Theory", *Phys. Rev. D* **85** (2012), 044007, arXiv: 1111.4049 [hep-th].

[150] B. Kleihaus, J. Kunz, and P. Kanti, "Particle-like ultracompact objects in Einstein-scalar-Gauss-Bonnet theories", *Phys. Lett. B* **804** (2020), 135401, arXiv: 1910.02121 [gr-qc].

[151] B. Kleihaus, J. Kunz, and P. Kanti, "Properties of ultracompact particlelike solutions in Einstein-scalar-Gauss-Bonnet theories", *Phys. Rev. D* **102** (2020), 024070, arXiv: 2005.07650 [gr-qc].

[152] J. L. Ripley and F. Pretorius, "Scalarized Black Hole dynamics in Einstein dilaton Gauss-Bonnet Gravity", *Phys. Rev. D* **101** (2020), 044015, arXiv: 1911.11027 [gr-qc].

[153] K. D. Kokkotas, R. A. Konoplya, and A. Zhidenko, "Analytical approximation for the Einstein-dilaton-Gauss-Bonnet black hole metric", *Phys. Rev. D* **96** (2017), 064004, arXiv: 1706.07460 [gr-qc].

[154] Z.-K. Guo, N. Ohta, and T. Torii, "Black Holes in the Dilatonic Einstein-Gauss-Bonnet Theory in Various Dimensions. I. Asymptotically Flat Black Holes", *Prog. Theor. Phys.* **120** (2008), 581, arXiv: 0806.2481 [gr-qc].

[155] J. L. Blázquez-Salcedo, F. S. Khoo, and J. Kunz, "Quasinormal modes of Einstein-Gauss-Bonnet-dilaton black holes", *Phys. Rev. D* **96** (2017), 064008, arXiv: 1706.03262 [gr-qc].

[156] J. L. Ripley and F. Pretorius, "Hyperbolicity in Spherical Gravitational Collapse in a Horndeski Theory", *Phys. Rev. D* **99** (2019), 084014, arXiv: 1902.01468 [gr-qc].

[157] J. L. Ripley and F. Pretorius, "Dynamics of a $\mathbb{Z}_2$ symmetric EdGB gravity in spherical symmetry", *Class. Quant. Grav.* **37** (2020), 155003, arXiv: 2005.05417 [gr-qc].

[158] W. E. East and J. L. Ripley, "Evolution of Einstein-scalar-Gauss-Bonnet gravity using a modified harmonic formulation", *Phys. Rev. D* **103** (2021), 044040, arXiv: 2011.03547 [gr-qc].

[159] W. E. East and J. L. Ripley, "Dynamics of Spontaneous Black Hole Scalarization and Mergers in Einstein-Scalar-Gauss-Bonnet Gravity", *Phys. Rev. Lett.* **127** (2021), 101102, arXiv: 2105.08571 [gr-qc].

[160] H.-J. Kuan, D. D. Doneva, and S. S. Yazadjiev, "Dynamical Formation of Scalarized Black Holes and Neutron Stars through Stellar Core Collapse", *Phys. Rev. Lett.* **127** (2021), 161103, arXiv: 2103.11999 [gr-qc].

[161] H.-J. Kuan, J. Singh, D. D. Doneva, S. S. Yazadjiev, and K. D. Kokkotas, "Nonlinear evolution and nonuniqueness of scalarized neutron stars", *Phys. Rev. D* **104** (2021), 124013, arXiv: 2105.08543 [gr-qc].

[162] W. E. East and F. Pretorius, "Binary neutron star mergers in Einstein-scalar-Gauss-Bonnet gravity", *Phys. Rev. D* **106** (2022), 104055, arXiv: 2208.09488 [gr-qc].

[163] M. Corman, J. L. Ripley, and W. E. East, "Nonlinear studies of binary black hole mergers in Einstein-scalar-Gauss-Bonnet gravity", *Phys. Rev. D* **107** (2023), 024014, arXiv: 2210.09235 [gr-qc].

[164] N. Franchini, M. Bezares, E. Barausse, and L. Lehner, "Fixing the dynamical evolution in scalar-Gauss-Bonnet gravity", *Phys. Rev. D* **106** (2022), 064061, arXiv: 2206.00014 [gr-qc].

[165] L. A. Saló, K. Clough, and P. Figueras, "Well-Posedness of the Four-Derivative Scalar-Tensor Theory of Gravity in Singularity Avoiding Coordinates", *Phys. Rev. Lett.* **129** (2022), 261104, arXiv: 2208.14470 [gr-qc].

[166] L. Aresté Saló, K. Clough, and P. Figueras, "Puncture gauge formulation for Einstein-Gauss-Bonnet gravity and four-derivative scalar-tensor theories in $d + 1$ spacetime dimensions", *Phys. Rev. D* **108** (2023), 084018, arXiv: 2306.14966 [gr-qc].

[167] D. D. Doneva, L. A. Saló, K. Clough, P. Figueras, and S. S. Yazadjiev, "Testing the limits of scalar-Gauss-Bonnet gravity through nonlinear evolutions of spin-induced scalarization", *Phys. Rev. D* **108** (2023), 084017, arXiv: 2307.06474 [gr-qc].

[168] R. Benkel, T. P. Sotiriou, and H. Witek, "Dynamical scalar hair formation around a Schwarzschild black hole", *Phys. Rev. D* **94** (2016), 121503, arXiv: 1612.08184 [gr-qc].

[169] R. Benkel, T. P. Sotiriou, and H. Witek, "Black hole hair formation in shift-symmetric generalised scalar-tensor gravity", *Class. Quant. Grav.* **34** (2017), 064001, arXiv: 1610.09168 [gr-qc].

[170] H. Witek, L. Gualtieri, P. Pani, and T. P. Sotiriou, "Black holes and binary mergers in scalar Gauss-Bonnet gravity: Scalar field dynamics", *Phys. Rev. D* **99** (2019), 064035, arXiv: 1810.05177 [gr-qc].

[171] M. Okounkova, "Stability of Rotating Black Holes in Einstein Dilaton Gauss-Bonnet Gravity", *Phys. Rev. D* **100** (2019), 124054, arXiv: 1909.12251 [gr-qc].

[172] M. Okounkova, "Numerical relativity simulation of GW150914 in Einstein-dilaton-Gauss-Bonnet gravity", *Phys. Rev. D* **102** (2020), 084046, arXiv: 2001.03571 [gr-qc].

[173] T. Evstafyeva, M. Agathos, and J. L. Ripley, "Measuring the ringdown scalar polarization of gravitational waves in Einstein-scalar-Gauss-Bonnet gravity", *Phys. Rev. D* **107** (2023), 124010, arXiv: 2212.11359 [gr-qc].

[174] H.-J. Kuan, A. T.-L. Lam, D. D. Doneva, S. S. Yazadjiev, M. Shibata, and K. Kiuchi, "Dynamical scalarization during neutron star mergers in scalar-Gauss-Bonnet theory", *Phys. Rev. D* **108** (2023), 063033, arXiv: 2302.11596 [gr-qc].

[175] D. Hilditch, "An Introduction to Well-posedness and Free-evolution", *Int. J. Mod. Phys. A* **28** (2013), 1340015, arXiv: 1309.2012 [gr-qc].

[176] O. A. Reula, "Hyperbolic methods for Einstein's equations", *Living Rev. Rel.* **1** (1998), 3.

[177] O. Sarbach and M. Tiglio, "Continuum and Discrete Initial-Boundary-Value Problems and Einstein's Field Equations", *Living Rev. Rel.* **15** (2012), 9, arXiv: 1203.6443 [gr-qc].

[178] B. Gustafsson, H.-O. Kreiss, and J. Oliger, *Time-Dependent Problems and Difference Methods*, John Wiley & Sons, Ltd (2013), ISBN 9781118548448.

[179] G. B. Whitham, *Linear and Nonlinear Waves*, John Wiley & Sons, Ltd (1999), ISBN 9781118032954.

[180] J. L. Ripley, "General relativity and its classical modification in gravitational collapse", Ph.D. thesis, Princeton U. (2020).

[181] M. C. Babiuc *et al.*, "Implementation of standard testbeds for numerical relativity", *Class. Quant. Grav.* **25** (2008), 125012, arXiv: 0709.3559 [gr-qc].

[182] P. Bosch, A. Buchel, and L. Lehner, "Unstable horizons and singularity development in holography", *JHEP* **2017** (2017), 135, arXiv: 1704.05454 [hep-th].

[183] A. Almheiri, T. Hartman, J. Maldacena, E. Shaghoulian, and A. Tajdini, "The entropy of Hawking radiation", *Rev. Mod. Phys.* **93** (2021), 035002, arXiv: 2006.06872 [hep-th].

[184] R. H. Dicke, "Coherence in Spontaneous Radiation Processes", *Phys. Rev.* **93** (1954), 99.

[185] T. J. M. Zouros and D. M. Eardley, "Instabilities of massive scalar perturbations of a rotating black hole", *Annals Phys.* **118** (1979), 139.

[186] S. R. Dolan, "Instability of the massive Klein-Gordon field on the Kerr spacetime", *Phys. Rev. D* **76** (2007), 084001, arXiv: 0705.2880 [gr-qc].

[187] P. Pani, V. Cardoso, L. Gualtieri, E. Berti, and A. Ishibashi, "Black-Hole Bombs and Photon-Mass Bounds", *Phys. Rev. Lett.* **109** (2012), 131102, arXiv: 1209.0465 [gr-qc].

[188] P. Pani, V. Cardoso, L. Gualtieri, E. Berti, and A. Ishibashi, "Perturbations of slowly rotating black holes: Massive vector fields in the Kerr metric", *Phys. Rev. D* **86** (2012), 104017, arXiv: 1209.0773 [gr-qc].

[189] H. Witek, V. Cardoso, A. Ishibashi, and U. Sperhake, "Superradiant instabilities in astrophysical systems", *Phys. Rev. D* **87** (2013), 043513, arXiv: 1212.0551 [gr-qc].

[190] V. Cardoso, O. J. C. Dias, G. S. Hartnett, M. Middleton, P. Pani, and J. E. Santos, "Constraining the mass of dark photons and axion-like particles through black-hole superradiance", *JCAP* **2018** (2018), 043, arXiv: 1801.01420 [gr-qc].

[191] V. P. Frolov, P. Krtouš, D. Kubizňák, and J. E. Santos, "Massive Vector Fields in Rotating Black-Hole Spacetimes: Separability and Quasinormal Modes", *Phys. Rev. Lett.* **120** (2018), 231103, arXiv: 1804.00030 [hep-th].

[192] S. R. Dolan, "Instability of the Proca field on Kerr spacetime", *Phys. Rev. D* **98** (2018), 104006, arXiv: 1806.01604 [gr-qc].

[193] R. Brito, V. Cardoso, and P. Pani, "Massive spin-2 fields on black hole spacetimes: Instability of the Schwarzschild and Kerr solutions and bounds on the graviton mass", *Phys. Rev. D* **88** (2013), 023514, arXiv: 1304.6725 [gr-qc].

[194] O. J. C. Dias, G. Lingetti, P. Pani, and J. E. Santos, "Black hole superradiant instability for massive spin-2 fields", *Phys. Rev. D* **108** (2023), L041502, arXiv: 2304.01265 [gr-qc].

[195] A. Arvanitaki, S. Dimopoulos, S. Dubovsky, N. Kaloper, and J. March-Russell, "String axiverse", *Phys. Rev. D* **81** (2010), 123530, arXiv: 0905.4720 [hep-th].

[196] S. Hod, "Stationary scalar clouds around rotating black holes", *Phys. Rev. D* **86** (2012), 104026, [Erratum: Phys.Rev.D 86, 129902 (2012)], arXiv: 1211.3202 [gr-qc].

[197] S. Hod, "Stationary resonances of rapidly-rotating Kerr black holes", *Eur. Phys. J. C* **73** (2013), 2378, arXiv: 1311.5298 [gr-qc].

[198] C. A. R. Herdeiro and E. Radu, "Kerr Black Holes with Scalar Hair", *Phys. Rev. Lett.* **112** (2014), 221101, arXiv: 1403.2757 [gr-qc].

[199] C. Herdeiro, E. Radu, and H. Rúnarsson, "Kerr black holes with Proca hair", *Class. Quant. Grav.* **33** (2016), 154001, arXiv: 1603.02687 [gr-qc].

[200] S. Hod, "The large-mass limit of cloudy black holes", *Class. Quant. Grav.* **32** (2015), 134002, arXiv: 1607.00003 [gr-qc].

[201] W. E. East and F. Pretorius, "Superradiant Instability and Backreaction of Massive Vector Fields around Kerr Black Holes", *Phys. Rev. Lett.* **119** (2017), 041101, arXiv: 1704.04791 [gr-qc].

[202] C. A. R. Herdeiro and E. Radu, "Dynamical Formation of Kerr Black Holes with Synchronized Hair: An Analytic Model", *Phys. Rev. Lett.* **119** (2017), 261101, arXiv: 1706.06597 [gr-qc].

[203] N. M. Santos, C. L. Benone, L. C. B. Crispino, C. A. R. Herdeiro, and E. Radu, "Black holes with synchronised Proca hair: linear clouds and fundamental non-linear solutions", *JHEP* **2020** (2020), 10, arXiv: 2004.09536 [gr-qc].

[204] C. A. R. Herdeiro, E. Radu, and N. M. Santos, "A bound on energy extraction (and hairiness) from superradiance", *Phys. Lett. B* **824** (2022), 136835, arXiv: 2111.03667 [gr-qc].

[205] A. Arvanitaki and S. Dubovsky, "Exploring the string axiverse with precision black hole physics", *Phys. Rev. D* **83** (2011), 044026, arXiv: 1004.3558 [hep-th].

[206] H. Kodama and H. Yoshino, "Axiverse and Black Hole", *Int. J. Mod. Phys. Conf. Ser.* **7** (2012), 84, arXiv: 1108.1365 [hep-th].

[207] H. Yoshino and H. Kodama, "Bosenova Collapse of Axion Cloud around a Rotating Black Hole", *Progress of Theoretical Physics* **128** (2012), 153, arXiv: 1203.5070 [gr-qc].

[208] H. Yoshino and H. Kodama, "Gravitational radiation from an axion cloud around a black hole: Superradiant phase", *PTEP* **2014** (2014), 043E02, arXiv: 1312.2326 [gr-qc].

[209] R. Brito, V. Cardoso, and P. Pani, "Black holes as particle detectors: evolution of superradiant instabilities", *Class. Quant. Grav.* **32** (2015), 134001, arXiv: 1411.0686 [gr-qc].

[210] H. Yoshino and H. Kodama, "The bosenova and axiverse", *Class. Quant. Grav.* **32** (2015), 214001, arXiv: 1505.00714 [gr-qc].

[211] M. Baryakhtar, R. Lasenby, and M. Teo, "Black hole superradiance signatures of ultralight vectors", *Phys. Rev. D* **96** (2017), 035019, arXiv: 1704.05081 [hep-ph].

[212] R. Brito, S. Ghosh, E. Barausse, E. Berti, V. Cardoso, I. Dvorkin, A. Klein, and P. Pani, "Gravitational wave searches for ultralight bosons with LIGO and LISA", *Phys. Rev. D* **96** (2017), 064050, arXiv: 1706.06311 [gr-qc].

[213] W. E. East, "Superradiant instability of massive vector fields around spinning black holes in the relativistic regime", *Phys. Rev. D* **96** (2017), 024004, arXiv: 1705.01544 [gr-qc].

[214] W. E. East, "Massive Boson Superradiant Instability of Black Holes: Nonlinear Growth, Saturation, and Gravitational Radiation", *Phys. Rev. Lett.* **121** (2018), 131104, arXiv: 1807.00043 [gr-qc].

[215] G. Ficarra, P. Pani, and H. Witek, "Impact of multiple modes on the black-hole superradiant instability", *Phys. Rev. D* **99** (2019), 104019, arXiv: 1812.02758 [gr-qc].

[216] N. Siemonsen and W. E. East, "Gravitational wave signatures of ultralight vector bosons from black hole superradiance", *Phys. Rev. D* **101** (2020), 024019, arXiv: 1910.09476 [gr-qc].

[217] R. Brito, S. Grillo, and P. Pani, "Black Hole Superradiant Instability from Ultralight Spin-2 Fields", *Phys. Rev. Lett.* **124** (2020), 211101, arXiv: 2002.04055 [gr-qc].

[218] N. Siemonsen, T. May, and W. E. East, "Modeling the black hole superradiance gravitational waveform", *Phys. Rev. D* **107** (2023), 104003, arXiv: 2211.03845 [gr-qc].

[219] P. V. P. Cunha, C. A. R. Herdeiro, E. Radu, and H. F. Rúnarsson, "Shadows of Kerr Black Holes with Scalar Hair", *Phys. Rev. Lett.* **115** (2015), 211102, arXiv: 1509.00021 [gr-qc].

[220] P. V. P. Cunha, C. A. R. Herdeiro, E. Radu, and H. F. Rúnarsson, "Shadows of Kerr black holes with and without scalar hair", *Int. J. Mod. Phys. D* **25** (2016), 1641021, arXiv: 1605.08293 [gr-qc].

[221] F. H. Vincent, E. Gourgoulhon, C. Herdeiro, and E. Radu, "Astrophysical imaging of Kerr black holes with scalar hair", *Phys. Rev. D* **94** (2016), 084045, arXiv: 1606.04246 [gr-qc].

[222] P. V. P. Cunha, C. A. R. Herdeiro, and E. Radu, "EHT Constraint on the Ultralight Scalar Hair of the M87 Supermassive Black Hole", *Universe* **5** (2019), 220, arXiv: 1909.08039 [gr-qc].

[223] R. Roy and U. A. Yajnik, "Evolution of black hole shadow in the presence of ultralight bosons", *Phys. Lett. B* **803** (2020), 135284, arXiv: 1906.03190 [gr-qc].

[224] G. Creci, S. Vandoren, and H. Witek, "Evolution of black hole shadows from superradiance", *Phys. Rev. D* **101** (2020), 124051, arXiv: 2004.05178 [gr-qc].

[225] Y. Chen, R. Roy, S. Vagnozzi, and L. Visinelli, "Superradiant evolution of the shadow and photon ring of Sgr A*", *Phys. Rev. D* **106** (2022), 043021, arXiv: 2205.06238 [astro-ph.HE].

[226] I. Sengo, P. V. P. Cunha, C. A. R. Herdeiro, and E. Radu, "Kerr black holes with synchronised Proca hair: lensing, shadows and EHT constraints", *JCAP* **2023** (2023), 047, arXiv: 2209.06237 [gr-qc].

[227] D. Baumann, H. S. Chia, and R. A. Porto, "Probing ultralight bosons with binary black holes", *Phys. Rev. D* **99** (2019), 044001, arXiv: 1804.03208 [gr-qc].

[228] J. Zhang and H. Yang, "Gravitational floating orbits around hairy black holes", *Phys. Rev. D* **99** (2019), 064018, arXiv: 1808.02905 [gr-qc].

[229] D. Baumann, H. S. Chia, R. A. Porto, and J. Stout, "Gravitational collider physics", *Phys. Rev. D* **101** (2020), 083019, arXiv: 1912.04932 [gr-qc].

[230] E. Berti, R. Brito, C. F. B. Macedo, G. Raposo, and J. a. L. Rosa, "Ultralight boson cloud depletion in binary systems", *Phys. Rev. D* **99** (2019), 104039, arXiv: 1904.03131 [gr-qc].

[231] J. Zhang and H. Yang, "Dynamic signatures of black hole binaries with superradiant clouds", *Phys. Rev. D* **101** (2020), 043020, arXiv: 1907.13582 [gr-qc].

[232] M. C. Ferreira, C. F. B. Macedo, and V. Cardoso, "Orbital fingerprints of ultralight scalar fields around black holes", *Phys. Rev. D* **96** (2017), 083017, arXiv: 1710.00830 [gr-qc].

[233] V. Cardoso, F. Duque, and T. Ikeda, "Tidal effects and disruption in superradiant clouds: A numerical investigation", *Phys. Rev. D* **101** (2020), 064054, arXiv: 2001.01729 [gr-qc].

[234] D. Baumann, G. Bertone, J. Stout, and G. M. Tomaselli, "Ionization of gravitational atoms", *Phys. Rev. D* **105** (2022), 115036, arXiv: 2112.14777 [gr-qc].

[235] D. Baumann, G. Bertone, J. Stout, and G. M. Tomaselli, "Sharp Signals of Boson Clouds in Black Hole Binary Inspirals", *Phys. Rev. Lett.* **128** (2022), 221102, arXiv: 2206.01212 [gr-qc].

[236] T. Takahashi, H. Omiya, and T. Tanaka, "Axion cloud evaporation during inspiral of black hole binaries: The effects of backreaction and radiation", *PTEP* **2022** (2022), 043E01, arXiv: 2112.05774 [gr-qc].

[237] G. M. Tomaselli, T. F. M. Spieksma, and G. Bertone, "Dynamical friction in gravitational atoms", *JCAP* **2023** (2023), 070, arXiv: 2305.15460 [gr-qc].

[238] B. Su, Z.-Z. Xianyu, and X. Zhang, "Probing Ultralight Bosons with Compact Eccentric Binaries", *Astrophys. J.* **923** (2021), 114, arXiv: 2107.13527 [gr-qc].

[239] T. Takahashi and T. Tanaka, "Axion clouds may survive the perturbative tidal interaction over the early inspiral phase of black hole binaries", *JCAP* **2021** (2021), 031, arXiv: 2106.08836 [gr-qc].

[240] R. D. Peccei and H. R. Quinn, "CP Conservation in the Presence of Pseudoparticles", *Phys. Rev. Lett.* **38** (1977), 1440.

[241] S. Weinberg, "A New Light Boson?", *Phys. Rev. Lett.* **40** (1978), 223.

[242] F. Wilczek, "Problem of Strong P and T Invariance in the Presence of Instantons", *Phys. Rev. Lett.* **40** (1978), 279.

[243] W. Hu, R. Barkana, and A. Gruzinov, "Fuzzy Cold Dark Matter: The Wave Properties of Ultralight Particles", *Phys. Rev. Lett.* **85** (2000), 1158, arXiv: astro-ph/0003365.

[244] L. Hui, J. P. Ostriker, S. Tremaine, and E. Witten, "Ultralight scalars as cosmological dark matter", *Phys. Rev. D* **95** (2017), 043541, arXiv: 1610.08297 [astro-ph.CO].

[245] E. G. M. Ferreira, "Ultra-light dark matter", *Astron. Astrophys. Rev.* **29** (2021), 7, arXiv: 2005.03254 [astro-ph.CO].

[246] E. Witten, "Some properties of O(32) superstrings", *Phys. Lett. B* **149** (1984), 351.

[247] P. Svrcek and E. Witten, "Axions in string theory", *JHEP* **2006** (2006), 051, arXiv: hep-th/0605206.

[248] M. Goodsell, J. Jaeckel, J. Redondo, and A. Ringwald, "Naturally light hidden photons in LARGE volume string compactifications", *JHEP* **2009** (2009), 027, arXiv: 0909.0515 [hep-ph].

[249] A. Arvanitaki, M. Baryakhtar, and X. Huang, "Discovering the QCD axion with black holes and gravitational waves", *Phys. Rev. D* **91** (2015), 084011, arXiv: 1411.2263 [hep-ph].

[250] A. Arvanitaki, M. Baryakhtar, S. Dimopoulos, S. Dubovsky, and R. Lasenby, "Black hole mergers and the QCD axion at Advanced LIGO", *Phys. Rev. D* **95** (2017), 043001, arXiv: 1604.03958 [hep-ph].

[251] R. Brito, S. Ghosh, E. Barausse, E. Berti, V. Cardoso, I. Dvorkin, A. Klein, and P. Pani, "Stochastic and Resolvable Gravitational Waves from Ultralight Bosons", *Phys. Rev. Lett.* **119** (2017), 131101, arXiv: 1706.05097 [gr-qc].

[252] O. A. Hannuksela, K. W. K. Wong, R. Brito, E. Berti, and T. G. F. Li, "Probing the existence of ultralight bosons with a single gravitational-wave measurement", *Nature Astron.* **3** (2019), 447, arXiv: 1804.09659 [astro-ph.HE].

[253] L. Tsukada, T. Callister, A. Matas, and P. Meyers, "First search for a stochastic gravitational-wave background from ultralight bosons", *Phys. Rev. D* **99** (2019), 103015, arXiv: 1812.09622 [astro-ph.HE].

[254] H. Davoudiasl and P. B. Denton, "Ultralight Boson Dark Matter and Event Horizon Telescope Observations of M87*", *Phys. Rev. Lett.* **123** (2019), 021102, arXiv: 1904.09242 [astro-ph.CO].

[255] K. K. Y. Ng, O. A. Hannuksela, S. Vitale, and T. G. F. Li, "Searching for ultralight bosons within spin measurements of a population of binary black hole mergers", *Phys. Rev. D* **103** (2021), 063010, arXiv: 1908.02312 [gr-qc].

[256] C. Palomba, S. D'Antonio, P. Astone, S. Frasca, G. Intini, I. La Rosa, P. Leaci, S. Mastrogiovanni, A. L. Miller, F. Muciaccia, O. J. Piccinni, L. Rei, and F. Simula, "Direct Constraints on the Ultralight Boson Mass from Searches of Continuous Gravitational Waves", *Phys. Rev. Lett.* **123** (2019), 171101, arXiv: 1909.08854 [astro-ph.HE].

[257] L. Sun, R. Brito, and M. Isi, "Search for ultralight bosons in Cygnus X-1 with Advanced LIGO", *Phys. Rev. D* **101** (2020), 063020, [Erratum: Phys.Rev.D 102, 089902 (2020)], arXiv: 1909.11267 [gr-qc].

[258] M. J. Stott, "Ultralight Bosonic Field Mass Bounds from Astrophysical Black Hole Spin", (2020), arXiv: 2009.07206 [hep-ph].

[259] K. K. Y. Ng, S. Vitale, O. A. Hannuksela, and T. G. F. Li, "Constraints on Ultralight Scalar Bosons within Black Hole Spin Measurements from the LIGO-Virgo GWTC-2", *Phys. Rev. Lett.* **126** (2021), 151102, arXiv: 2011.06010 [gr-qc].

[260] L. Tsukada, R. Brito, W. E. East, and N. Siemonsen, "Modeling and searching for a stochastic gravitational-wave background from ultralight vector bosons", *Phys. Rev. D* **103** (2021), 083005, arXiv: 2011.06995 [astro-ph.HE].

[261] C. Ünal, F. Pacucci, and A. Loeb, "Properties of ultralight bosons from heavy quasar spins via superradiance", *JCAP* **2021** (2021), 007, arXiv: 2012.12790 [hep-ph].

[262] R. Abbott *et al.* [The LIGO Scientific Collaboration, the Virgo Collaboration, and the KAGRA Collaboration], "All-sky search for gravitational wave emission from scalar boson clouds around spinning black holes in LIGO O3 data", *Phys. Rev. D* **105** (2022), 102001, arXiv: 2111.15507 [astro-ph.HE].

[263] R. Abbott *et al.* [LIGO Scientific Collaboration, Virgo Collaboration, and KAGRA Collaboration], "Search for continuous gravitational wave emission from the Milky Way center in O3 LIGO-Virgo data", *Phys. Rev. D* **106** (2022), 042003, arXiv: 2204.04523 [astro-ph.HE].

[264] A. Dima and E. Barausse, "Numerical investigation of plasma-driven superradiant instabilities", *Class. Quant. Grav.* **37** (2020), 175006, arXiv: 2001.11484 [gr-qc].

[265] D. Blas and S. J. Witte, "Quenching mechanisms of photon superradiance", *Phys. Rev. D* **102** (2020), 123018, arXiv: 2009.10075 [hep-ph].

[266] F. Cattani, A. Kim, D. Anderson, and M. Lisak, "Threshold of induced transparency in the relativistic interaction of an electromagnetic wave with overdense plasmas", *Phys. Rev. E* **62** (2000), 1234.

[267] M. Tushentsov, A. Kim, F. Cattani, D. Anderson, and M. Lisak, "Electromagnetic Energy Penetration in the Self-Induced Transparency Regime of Relativistic Laser-Plasma Interactions", *Phys. Rev. Lett.* **87** (2001), 275002.

[268] V. I. Berezhiani, D. P. Garuchava, S. V. Mikeladze, K. I. Sigua, N. L. Tsintsadze, S. M. Mahajan, Y. Kishimoto, and K. Nishikawa, "Fluid-Maxwell simulation of laser pulse dynamics in overdense plasma", *Physics of Plasmas* **12** (2005), 062308.

[269] E. Esarey, C. B. Schroeder, and W. P. Leemans, "Physics of laser-driven plasma-based electron accelerators", *Rev. Mod. Phys.* **81** (2009), 1229.

[270] I. D. Novikov and K. S. Thorne, "Astrophysics and black holes", in "Proceedings, Ecole d'Eté de Physique Théorique: Les Astres Occlus", (1973) pp. 343–550.

[271] P. Sprangle, E. Esarey, and A. Ting, "Nonlinear theory of intense laser-plasma interactions", *Phys. Rev. Lett.* **64** (1990), 2011.

[272] T. Tajima and J. M. Dawson, "Laser Electron Accelerator", *Phys. Rev. Lett.* **43** (1979), 267.

[273] J. M. Dawson, "Nonlinear Electron Oscillations in a Cold Plasma", *Phys. Rev.* **113** (1959), 383.

[274] A. I. Akhiezer and R. V. Polovin, "Theory of wave motion of an electron plasma", *Soviet Phys. JETP* **3** (1956).

[275] A. Pukhov and J. Meyer-ter Vehn, "Laser wake field acceleration: the highly non-linear broken-wave regime", *Appl. Phys. B* **74** (2002), 355.

[276] A. Bergmann and P. Mulser, "Breaking of resonantly excited electron plasma waves", *Phys. Rev. E* **47** (1993), 3585.

[277] R. M. G. M. Trines and P. A. Norreys, "Wave-breaking limits for relativistic electrostatic waves in a one-dimensional warm plasma", *Physics of Plasmas* **13** (2006), 123102.

[278] E. Siminos, B. Svedung Wettervik, M. Grech, and T. Fülöp, "Kinetic effects on the transition to relativistic self-induced transparency in laser-driven ion acceleration", in "APS Division of Plasma Physics Meeting Abstracts", , volume 2016 of *APS Meeting Abstracts* (2016) p. TO6.007.

[279] A. Pukhov and J. Meyer-ter Vehn, "Laser Hole Boring into Overdense Plasma and Relativistic Electron Currents for Fast Ignition of ICF Targets", *Phys. Rev. Lett.* **79** (1997), 2686.

[280] A. Macchi, "Theory of light sail acceleration by intense lasers: an overview", *High Power Laser Science and Engineering* **2** (2014), e10.

[281] S. S. Bulanov, E. Esarey, C. B. Schroeder, S. V. Bulanov, T. Z. Esirkepov, M. Kando, F. Pegoraro, and W. P. Leemans, "Radiation pressure acceleration: The factors limiting maximum attainable ion energy", *Physics of Plasmas* **23** (2016), 056703.

[282] G. Lingetti, E. Cannizzaro, and P. Pani, "Superradiant instabilities by accretion disks in scalar-tensor theories", *Phys. Rev. D* **106** (2022), 024007, arXiv: 2204.09335 [gr-qc].

[283] Z. Wang, T. Helfer, K. Clough, and E. Berti, "Superradiance in massive vector fields with spatially varying mass", *Phys. Rev. D* **105** (2022), 104055, arXiv: 2201.08305 [gr-qc].

[284] J. Kommemi, "The Global Structure of Spherically Symmetric Charged Scalar Field Spacetimes", *Commun. Math. Phys.* **323** (2013), 35, arXiv: 1107.0949 [gr-qc].

[285] O. Baake and O. Rinne, "Superradiance of a charged scalar field coupled to the Einstein-Maxwell equations", *Phys. Rev. D* **94** (2016), 124016, arXiv: 1610.08352 [gr-qc].

[286] W. E. East, F. M. Ramazanoğlu, and F. Pretorius, "Black Hole Superradiance in Dynamical Spacetime", *Phys. Rev. D* **89** (2014), 061503, arXiv: 1312.4529 [gr-qc].

[287] C. Kehle and R. Unger, "Gravitational collapse to extremal black holes and the third law of black hole thermodynamics", (2022), arXiv: 2211.15742 [gr-qc].

[288] A. Hegade K. R., J. L. Ripley, and N. Yunes, "Where and why does Einstein-scalar-Gauss-Bonnet theory break down?", *Phys. Rev. D* **107** (2023), 044044, arXiv: 2211.08477 [gr-qc].

[289] B. Carr, K. Kohri, Y. Sendouda, and J. Yokoyama, "Constraints on primordial black holes", *Rept. Prog. Phys.* **84** (2021), 116902, arXiv: 2002.12778 [astro-ph.CO].

[290] A. Caputo, S. J. Witte, D. Blas, and P. Pani, "Electromagnetic signatures of dark photon superradiance", *Phys. Rev. D* **104** (2021), 043006, arXiv: 2102.11280 [hep-ph].

[291] N. Siemonsen, C. Mondino, D. Egana-Ugrinovic, J. Huang, M. Baryakhtar, and W. E. East, "Dark photon superradiance: Electrodynamics and multimessenger signals", *Phys. Rev. D* **107** (2023), 075025, arXiv: 2212.09772 [astro-ph.HE].

[292] N. Sanchis-Gual, J. C. Degollado, C. Herdeiro, J. A. Font, and P. J. Montero, "Dynamical formation of a Reissner-Nordström black hole with scalar hair in a cavity", *Phys. Rev. D* **94** (2016), 044061, arXiv: 1607.06304 [gr-qc].